論文 / 著書情報
Article / Book Information

題目(和文)	テトラダイマイト構造をもつトポロジカル絶縁体における光励起電子およびフォノン超高速ダイナミクス
Title(English)	Ultrafast dynamics of photoexcited electrons and coherent phonons in topological insulators having the tetradymite structure
著者(和文)	則松桂
Author(English)	Katsura Norimatsu
出典(和文)	学位:博士（理学）, 学位授与機関:東京工業大学, 報告番号:甲第10093号, 授与年月日:2016年3月26日, 学位の種別:課程博士, 審査員:中村 一隆,笹川 崇男,小田原 修,吉本 護,和田 裕之
Citation(English)	Degree:, Conferring organization: Tokyo Institute of Technology, Report number:甲第10093号, Conferred date:2016/3/26, Degree Type:Course doctor, Examiner:,,,,
学位種別(和文)	博士論文
Type(English)	Doctoral Thesis

Ultrafast dynamics of photoexcited electrons and coherent phonons in topological insulators having the tetradymite structure

Katsura Norimatsu

Department of Innovative and Engineered Materials,
Interdisciplinary Graduate School of Science and Engineering,
Tokyo Institute of Technology

Contents

Chapter 3.
Phonon dynamics

Acknowledgement

Throughout the last five years, I have received tremendous amount of scientific, technical and personal support by uncountable number of great people in order to finalize this thesis. I would like to acknowledge and appreciate all these people who have been involved in making my Ph.D. study possible to complete.

The present study was managed under the guidance of Prof. Kazutaka G. Nakamura of the Materials and Structures Laboratory (MSL), Tokyo Institute of Technology (Tokyo Tech). My Ph.D. study could not be completed successfully without the continuous care and support I have received from Prof. Nakamura. His passion towards his study and education was truly inspiring and I have acquired a huge amount of knowledge and experience by studying under him.

This research could not be carried out without the support and guidance provided by my co-supervisor, Prof. Takao Sasagawa. I sincerely appreciate him for providing all the precious samples for my research. Prof. Yosuke Kayanuma, Prof. Fujio Minami, and Prof. Masahiro Kitajima have contributed hugely on providing valuable suggestions towards my research methods and also I always enjoyed having great conversation with such amazing and inspiring people. I would also like to thank Prof. Osamu Odawara, Prof. Mamoru Yoshimoto, and Prof. Hiroyuki Wada for their guidance, suggestions, and arrangements for my thesis presentation. I would also like to gratitude Prof. Tomokazu Iyoda and Prof. Keiji Nagai for their encouragement in my Ph.D. course.

Prof. Masaki Hada of Okayama University should also be acknowledged for his continuous support and guidance given to me throughout my Ph.D. course. Prof. Hiroki Taniguchi of Nagoya University helped me with measuring the Raman spectrum. I have received a great help from Prof. Tadahiko Ishikawa of Department of Chemistry and

Materials Science of Tokyo Tech for measuring the reflectivity spectra. I also appreciate Prof. Shin-ya Koshihara for permitting me to use his valuable equipment. I would like to thank Prof. Ken Onda and Dr. Sei'ichi Tanaka of Interactive Research Center of Science of Tokyo Tech for providing machine to perform mid-infrared experiments and help me in measuring the data. Mr. Sercan Keskin at the R. J. Dwayne Miller's group in the Max Plank Institute for the Structure and Dynamics of Matter helped me with preparing thin Bi_2Te_3 sample.

Prof. Yutaka Shikano and Prof. Yasuaki Okano of Institute for Molecular Science have given me guidance and encouragement by sharing their knowledge and experience which was also quite valuable for my research. Ms. Aki Miyamoto, a secretary of the Nakamura research group, cannot be missed to be acknowledged hugely on giving me unconditional mental support and great advice throughout my study.

Prof. Kazutaka Ohkawa of Tokyo University of Science have supported my research by giving me continuous valuable advice and great encouragement. Prof.Takashi Sawaguchi of Nihon University and Dr. Nanae Yamashita suggested and provided me a fantastic opportunity to proceed to study at the postgraduate course in Tokyo Tech.

My appreciation should also be extended to the past and present members in the laboratory for their support and friendship. Dr. Jianbo Hu helped to carry out coherent phonon measurements in Bi_2Se_3. Prof. Hiroshi Takahashi, Mr. Arihiro Goto, Mr. Tomoaki Doki, and Mr. Takayuki Eda also greatly supported my research. My friends/co-researchers, Mr. Shinichi Harada, Mr. Yuki Kabasawa, and Mr. Dai Horiuchi have always given me warm encouragement throughout my Ph.D. study and I could not go through it without their support. Mr. Shingo Hayashi, Mr. Keigo Kato, Mr. Norihisa Kndo, Mr. Akira Ochi, and Mr. Kensuke Yokota shared their experiments to carry out all measurements in Bi and GaAs. Mr. Shin-ichi Uozumi was involved in the experiments of measuring the coherent phonons in topological insulators. Mr. Tetsuya Tsuruta shared to assemble the optical pump-probe system with using the sub-10 femtosecond laser. Mr. Kazuma Ohya helped to draw the experimental setup and Mr. Kenichi Goto, Mr. Hiroya Sasaki, and Mr. Takuya Imaizumi have always been a huge support for research and also my life as a Ph.D. student.

I am particularly grateful for the assistance given by Mr. Rikizo Yano of Sasagawa

group. I would like to thank Mr. Hiromasa Namiki for measuring carrier density of Sb_2Te_3, Mr. Syuhei Yamamoto and Mr. Kyushiro Igarashi of Sasagawa group for preparing all the samples in order to complete this thesis.

This work was hugely supported by Core Research for Evolutional Science and Technology of Japan Science and Technology Agency. In addition, I would like to acknowledge the Grant-in-Aid for Japan Society for the Promotion of Science Fellows for supporting this study.

Finally, no words can be sufficient enough to describe my appreciation to the members of my family who have shown endless support and unconditional love throughout my whole journey to complete this study.

23. Feb. 2016

Katsura Norimatsu

Abstract

The dynamics of phonons and electrons can be directly studied by femtosecond time-resolved reflectance spectroscopy. Phonons are excited coherently in solids by irradiation of femtosecond laser pulses, whose duration much shorter than the period of the atomic vibration (coherent phonon). Here, I apply this technique for the topological insulators, which behave as a semiconductor in the bulk and metal-like conductivity on its edge and surface. The dynamics of photoexcited electrons and phonons in topological insulators would be closely related with intrinsic features for electronic applications. However, the quantitatively measurements of them is still lacking.

In this dissertation, following results consist of two parts: phonon dynamics and carrier dynamics. First, I observed all the Raman active optical phonons (E_g^1, E_g^2, A_{1g}^1, and A_{1g}^2) in topological insulators (Sb_2Te_3, Bi_2Te_3, and Bi_2Se_3) using femtosecond time-resolved near-infrared (IR) reflectivity measurements. Amplitude of these coherent phonons strongly depends on polarization of an excitation pulse, and I clarified their lifetimes. Secondly, the dynamics of photoexcited topological insulators *p*-type Sb_2Te_3 has been studied using the time-resolved mid-IR reflectivity measurements. It was found that the photoexcited relaxation process is as follows: electrons were excited in the bulk-conduction band and generate coherent phonons (< 1 ps). These coherent phonons relax to the equilibrium state within 4 ps. In addition, electrons on the surface (Dirac Fermions) are supplied from the bulk-valence band because of the generated holes in the bulk-valence band via auger electron transition (< 1 ps). Thereafter, the excited electrons go back to the bulk-valence band within 10 ps via recombination of holes with electrons relaxed through a Dirac cone surface state. The faster relaxation time ($\tau = 3.3$ ps) implies a characteristic of topological insulator having a Dirac cone surface state, like similarly to a graphene.

Chapter1.
General introduction

It has been urgently required to investigate and control the faster and the smaller-scaled phenomena as the internet grows faster and the information we deal with gets denser. In order to accomplish these requirements, it is necessary to attain the size of sub-nanometer and the time scale of femtosecond. Usually, we can photographically observe the image of atomic configuration by applying scanning electron microscope (SEM), scanning probe microscope (SPM), and tunneling electron microscope (TEM). The additional requirement is that how we can do the same for atomic and electric motions. Measuring the time scale of femtosecond is one of the milestones since it is the time scale of the fastest atomic motions i.e. phonon vibration, these transitions or chemical reactions. Monitoring fastest electrons and atoms dynamics requires the time-resolution of less than a few picoseconds. The current electric devices are not fast enough to detect these ultrafast phenomena. The sets of the current electric devices such as photo multiplier tube, streak camera, and multichannel reproduction photodiode enable us to study on relatively slow photoexcited molecular transition and electric transition in chemical reaction process with ~10 ps time-resolution. This problem can be solved by using the femtosecond pulse laser as a replacement. The principle is almost the same as strobe camera, and this technique is exploited to femtosecond time-domain spectroscopy.

In this study, I worked on ultrafast time-domain spectroscopy of the chalcogenide compounds (Bi_2Te_3, Sb_2Te_3 and Bi_2Se_3). Such chalcogenide compounds are known as the highest figure-of-merit coefficient $ZT \cong 1$ among bulk thermoelectric materials[1-6] and phase-change materials for data-storage applications[7]. Recently, they

have also been known as topological insulators[8,9] which are characterization of photoexcited electron- and phonon- dynamics in the material. The unique properties of the topological insulators can be used for some electronic device applications.

1.1 Ultrafast phenomena

Time acts as a benchmark for indicating the continued existence of materials and rate of changes, and deeply involved in the biological, chemical, and physical systems. It was in 1989 when I was just born, Ramsey, the American physicist, was awarded Nobel Prize in Physics for his invention of an extremely accurate atom clock by using the resonance frequency of cesium atoms[10]. In natural sciences, time is an indispensable parameter. Figure 1-1 shows a time scale of natural phenomena and device responsiveness around us; for example, a heartbeat ~1 second (s), a blink of an eye ~150 milliseconds (1 ms = 10^{-3} s), a shutter speed of camera ~2 microseconds (1 μs = 10^{-6} s), throughput of general computer for nanoseconds (1 ns = 10^{-9} s) order, and so on. Subsequently, there are faster phenomena with timescale of picoseconds (1 ps = 10^{-12} s) to attoseconds (1 as = 10^{-18} s), which are called 'Ultrafast phenomena'. The timescale of picoseconds is lattice-vibrational period (*e.g.*, to move the position of atoms in the ammonia molecule ~21 ps[11]). The femtoseconds (1 fs = 10^{-15} s) is the vibration time as the strontium atom, chemical reactions occur, and light travels a distance of about 300 nm. It is peculiarly interesting for us to elucidate the ultrafast phenomena of ps to fs time region, which might bring us an innovation and advancement in various research fields in the future. The attosecond is the half-life of the η-meson[11], and light travels a distance of about 0.3 nm. We can see the objects with our eyes like a camera, so that a light is an essential tool to observe everything. Similarly, a method of spectroscopy is the field of interaction between light and materials to investigate molecular vibrations, electric band structures, phase transitions and so on.

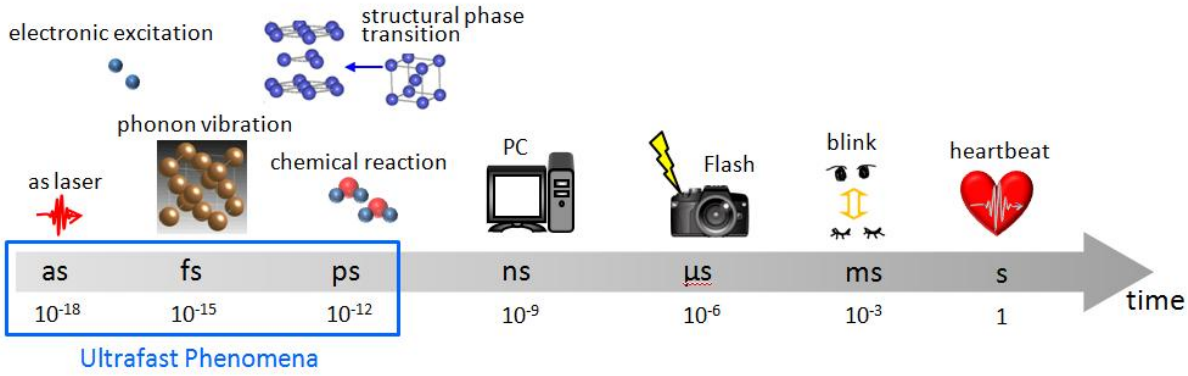

Fig. 1-1 Typical time-scales of phenomena around us.

1.2 Time-domain spectroscopy

Materials around us are composed of atoms and electrons, which move with velocities of 1/1000 to 1/100 the speed of light. Chemical reactions occur at time scale of 10 to100 fs as forming or breaking chemical bonds between atoms[11]. In order to investigate the ultrafast phenomena such as photoexcied electronic state, electronic structure, relaxation process and lattice vibration at time scale less than a few picoseconds, we need some ultrafast observation techniques. The presently electric devices (photodetectors: photomultiplier tube, streak camera, multichannel reproduction photodiode) are not fast enough to be used to observe these ultrafast phenomena, because the time resolution of the electric device is limited ~10 ps order. Ahmed Zewail, the American scientist, has been observing intramolecular vibrational processes of molecules by using a molecular beam and a picoseconds or femtosecond laser since 1979[12-14]. In 1999, he was awarded Novel Prize in Chemistry for his studies of the transition states of chemical reactions by using femtosecond spectroscopy[15]. He revealed the uni-molecular reaction by using the iodine cyanide molecule, dissociates into iodine (I) and cyanide (CN): $ICN \rightarrow I + CN$. In order to monitor the ultrafast time-behavior like a chemical reaction, it was a vital point to prepare an ultrafast shutter for observing targets that is an ultrashort pulse laser. The laser has some profitable characters; coherent light with high irradiance, monochromic, and convergent. They are applied to electronic devices, optical communications, metallic processing, medical care,

and ultrafast spectroscopy.

A pump-probe technique is the most commonly used technique in femtosecond time-resolved spectroscopy. This technique generally uses two optical pulses. The output pulses derived from laser is divided into two pulses; one is used to excite electrons in the materials (pump pulse), and the other pulse (probe pulse) is used to detect the changes induced by the pump pulse. The power of the probe pulse is set to be much smaller than that of the pump pulse in order not to induce any changes in the sample. The arrival time of the pump and probe pulse is controlled by changing length of each optical path. The time resolution in the pump-probe technique depends on the pulse width, and the mechanical pitch of optical delay stage. The study of ultrafast phenomena has been conducted by using wide region of electromagnetic wave from infrared light to soft X-rays.

1.3 Coherent phonon and generation mechanism

Phonon is a quantization of lattice vibration, which carries vital roles in physical properties in condensed matter. Usually phonons are randomly oscillating (incoherent) in thermal equilibrium. Then the displacement of the atoms is almost zero in time and space because they have each different wave vectors and frequencies. On the other hand, phonons are excited coherently by irradiation of femtosecond laser pulses, whose duration is much shorter than the vibrational period. The synchronized and collective atomic motion is so-called coherent phonons as illustrated in Fig. 1-2. The coherent phonons are detected as a modulation in transient reflectivity or transmission via a change of electric susceptibility. By using the coherent phonons, we can directly detect not only vibrational frequency but also their dephasing time.

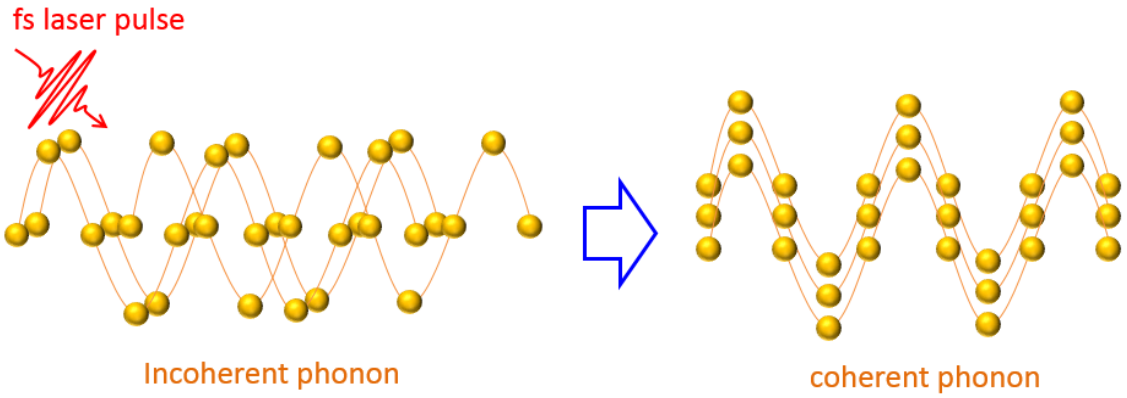

Fig. 1-2 Schematic of coherent phonon generation

In 1985, K. A. Nelson *et al.*[16] reported the first observations of coherent phonon in solid : α–perylene. Since then, coherent phonons have been conducted for various materials such as semimetals[17,18], semiconductors[19], and superconductors[20,21]. The generation mechanism of coherent phonons have been proposed by several groups[22-24], and they are classified into two processes: one is impulsive stimulated Raman scattering (ISRS) for transparent region and the other is impulsive absorption (IA) for opaque region[25]. The IA process is usually referred as displacement enhanced coherent phonon (DECP) process.

1.3.1 Impulsive Stimulated Raman Scattering (ISRS)

Figure 1-3(a) shows the generation mechanism of ISRS. This mechanism is the non-linear optical process in case of using ultrashort pulse laser as a pump pulse, and dominantly occurs in transparent conditions. The ultrashort pulse has a broad bandwidth which includes both the excitation light and Stokes (or anti-Stokes) light. Then the stimulated Raman process occurs instantaneously within a single optical pulse.

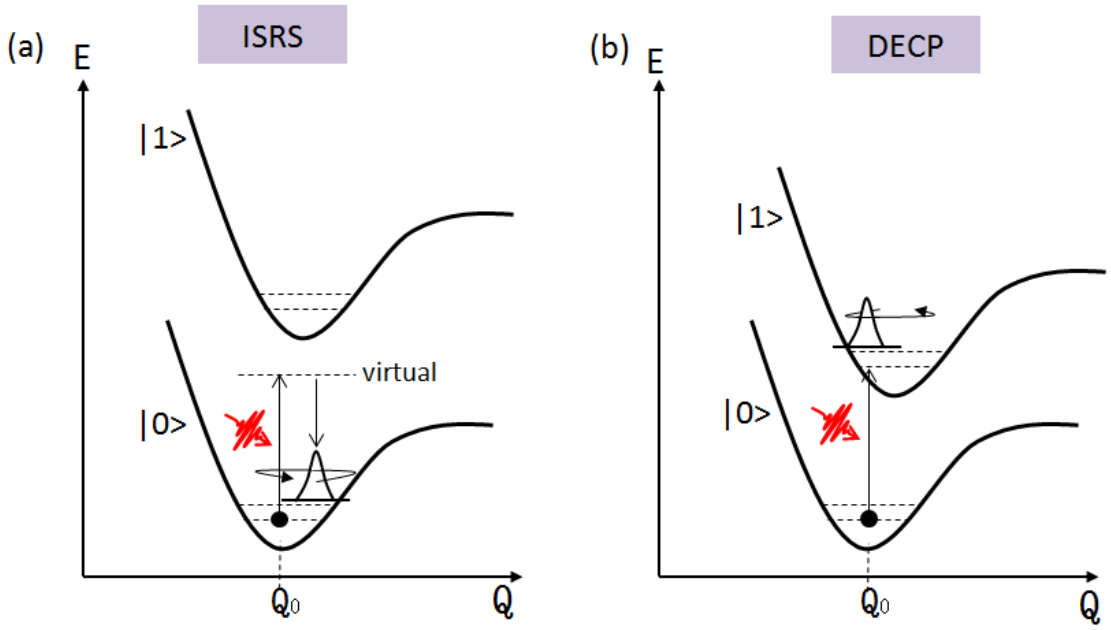

Fig. 1-3 General generation mechanism of coherent phonons (a) ISRS and (b) DECP.

1.3.2 Displacive Excitation of Coherent Phonons (DECP)

Figure 1-3(b) shows the generation mechanism of DECP. This is one of the generation mechanisms of coherent phonons given by Dresselhause group[22]. The changes of carrier density $n(t)$ by laser irradiation in materials is expressed by

$$\frac{dn(t)}{dt} = \alpha P(t) - \beta n(t), \tag{1.1}$$

where α is the absorption coefficient, $P(t)$ is the power of light, and β is the relaxation coefficient. Potential energy surface of the electronic excited state is usually different from that of the ground state. They assumed that the equilibrium position $Q_0(t)$ of atom is proportional to the photoexcited carrier density as

$$Q_0(t) = kn(t), \tag{1.2}$$

where k is a proportional constant. The equation of motion for general coordinate $Q(t)$ of lattice vibration can be written as

$$\frac{d^2Q(t)}{dt^2} = -\omega_0^2\big(Q(t) - Q_0(t)\big) - 2\Upsilon\frac{dQ(t)}{dt}, \tag{1.3}$$

where ω_0 is an angular frequency of the lattice vibration, Υ is a relaxation constant.

Ususally, a photoexcited density become

$$n(t) \propto e^{-\beta t}\,, \tag{1.4}$$

and the time variable carrier density is expressed as

$$n(t) = \rho E_p \int_0^\infty g(t-\tau) e^{-\beta\tau} d\tau\,, \tag{1.5}$$

where E_p is a laser fluence. Here, $P(t)$ can be expresses as

$$P(t) = E_p \cdot g(t), \tag{1.6}$$

$$\int_{-\infty}^{\infty} g(t)dt = 1\,, \tag{1.7}$$

where $g(t)$ indicate normalized pulse shape. The $Q(t)$ is obtained as

$$Q(t) = \frac{\omega_0^2 k\rho E_p}{(\omega_0^2 + \beta^2 - 2\Upsilon\beta)} \int_0^\infty g(t-\tau)\left[e^{-\beta\tau} - e^{\Upsilon\tau}\left(\cos(\Omega\tau) - \frac{\beta'}{\Omega}\sin(\Omega\tau)\right)\right] d\tau, \tag{1.8}$$

where

$$\Omega \equiv \sqrt{\omega_0^2 - \Upsilon^2}\,, \tag{1.9}$$

$$\beta' = \beta - \Upsilon\,. \tag{1.10}$$

1.3.3 Coherent phonon detection

The measurements of coherent phonons are conducted as a modulation in transient reflectivity via a change of electric susceptibility. Reflectivity change is expressed by

$$\frac{\Delta R(t)}{R} = \frac{1}{R}\left[\left(\frac{\partial R}{\partial n}\right) n(t) + \left(\frac{\partial R}{\partial Q}\right) Q(t) + \left(\frac{\partial R}{\partial T_e}\right) \Delta T_e\right] \tag{1.11}$$

where $n(t)$ is the excited band carrier density, $Q(t)$ is nuclear coordinate, ΔT_e is a change in electron temperature at Fermi level produced by the pump pulse[26-28], which led to interpretation of electron-phonon coupling strength[28].

For sufficiently narrow pump and probe pulses compared to the period of oscillation $1/\omega_0$,

$$\overline{\frac{\Delta R(t)}{R}} = Ae^{-\beta t} + \mathrm{B}\frac{\omega_0^2}{\omega_0^2 + \beta^2 - 2\gamma\beta}\left[e^{-\beta t} - e^{-\gamma t}\left(\cos(\Omega t) - \frac{\beta'}{\Omega}\sin(\Omega t)\right)\right], \tag{1.12}$$

where

$$A = \frac{1}{R}\left[\left(\frac{\partial R}{\partial \epsilon_1}\right)\left(\frac{\partial \epsilon_1}{\partial n}\right) + \left(\frac{\partial R}{\partial \epsilon_2}\right)\left(\frac{\partial \epsilon_2}{\partial n}\right)\right]\rho\varepsilon_{\text{pump}} \tag{1.13}$$

$$B = \frac{1}{R}\left[\left(\frac{\partial R}{\partial \epsilon_1}\right)\left(\frac{\partial \epsilon_1}{\partial Q}\right) + \left(\frac{\partial R}{\partial \epsilon_2}\right)\left(\frac{\partial \epsilon_2}{\partial Q}\right)\right]\kappa\rho\varepsilon_{\text{pump}} \tag{1.14}$$

where Ω and β' are given by $\Omega \equiv \sqrt{{\omega_0}^2 - \gamma^2}$ (Eq.1-9), and $\beta' = \beta - \gamma$ (Eq.1-10), respectively. The amplitude of coherent phonon is described as

$$\frac{\omega_0^2}{(\omega_0^2 + \beta^2 - 2\gamma\beta)}. \tag{1.15}$$

Equations (1.11) and (1.12) show that the reflectivity change includes change in carrier density $n(t)$ and normal coordinate $Q(t)$ of the phonons. Then we can directly monitor the $Q(t)$, which represents the atomic motion, from the modulation in transient reflectivity.

1.4 Topological insulators

Generally, inorganic materials are categorized into metal, semiconductor or insulator. Their differences are determined by the electric structure as shown in Fig. 1-4. Recently, topological insulators are a new quantum phase of matter that behave as a semiconductor with small band gap in the bulk but have metal-like conductivity on its edge and surface because of having a Dirac dispersion. In this chapter, the fundamentals of topological insulator and recent studies are described.

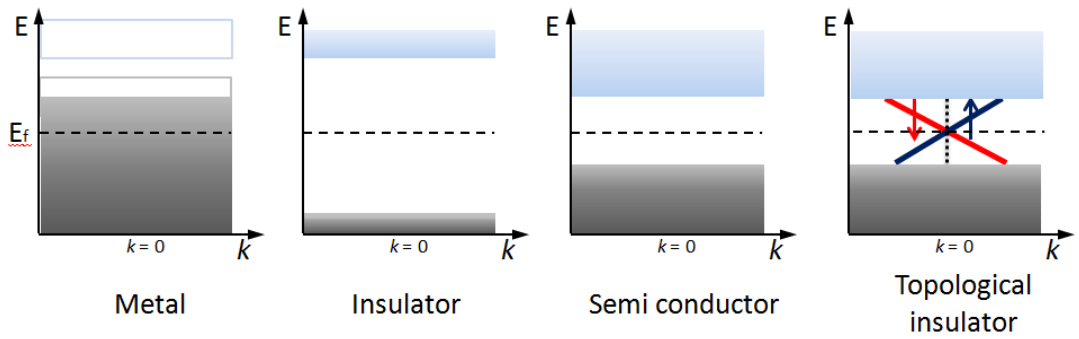

Fig. 1-4 Electronic band structures of metal, insulator, semiconductor, and topological insulator.

1.4.1 Graphene

Graphene is a single atomic layer of graphite known as two dimensional material. In 2004, a graphene consists of carbon monolayer was first isolated despite of the theoretically predicted thermal instability. The special properties of graphene are different from other forms of carbon such as graphite, diamond, fullerene and so on. In particular, the superior electrical conductivity, thermal stability, and mechanical strength have been actively studied in the field of electrochemistry[29,30]. In 2010, Andre Geim and Konstantin Novoselov were awarded Nobel Prize in physics for groundbreaking experiments regarding the two-dimensional material graphene[31]. The dispersion of the band gap in the ordinary semiconductors can be approximated by parabolic curve and described with quantum effect via Schrödinger equation. In contrast, that of graphene has linear dispersion relation so-called Dirac cone in the Γ point of the Brillouin Zone. The electrons existing on the Dirac cone (Dirac Fermions) cannot define the effective mass hence they are massless quasi particle. Therefore Dirac Fermions would be expected as lower power consumption devices. Graphene had been widely known as the only material possessing the Dirac Fermions, however in recent years another substance which also possesses the Dirac Fermions has been newly discovered. That is called "topological insulators".

1.4.2 Topological insulators

As shown in Fig. 1-5, topological insulator is a new quantum phase of matter, which has a band gap in the bulk while topologically protected edge and surface states due to the time reversal symmetry. It means that spin-orbit coupling gives rise to electrically insulating states in the bulk and robust conducting states along the edge.

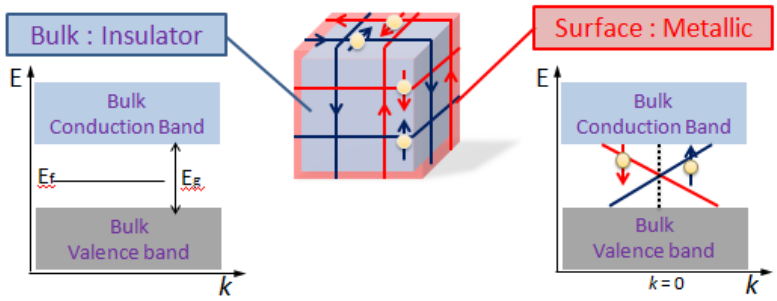

Fig. 1-5 Schematic of topological insulator: a simple model insulating band structure of bulk state and Dirac dispersion of surface state.

The classification of topology can differentiate by 'topological invariant'. For example, there are differences between a doughnut and a ball associated with the number of hole. They are distinguished from two-valued topological invariant, called Z_2 index. In a similar way, a wave function having an electronic state of topological insulator is determined with parity. The surface state has a helical spin structure. The electron backscattering induced by nonmagnetic impurities is suppressed by a helical spin texture. Despite of a relatively a short history since its discovery, topological insulators have attracted many scientists for their considerable ways of using on different variety of devices and creation of new creative applications [32,33]. Topological insulator is theoretically predicted in the researches of quantum spin hall effect[34-36], and the researches have begun with the two-dimensional (2D) topological insulators such as CdTe/HgTe/CdTe quantum well structures[37] and AlSb/InAs/GaSb/AlSb quantum well structures[38]. They actually have very small band gap lower than 10 meV.

In 2008[39,40], the $Bi_{1-x}Sb_x$ single crystal has experimentally discovered as a three-dimensional (3D) topological insulator, but unfortunately it was also unsuitable for the study because of the complicated surface structure. Subsequently, a lot of the 3D topological insulators have been suggested and observed (e.g., Bi_2Te_3[41], Bi_2Se_3[41], Sb_2Te_3[41], $(Bi_{1-x}Sb_x)_2Te_3$[42], $Bi_{2-x}Sb_xTe_{3-y}Se_y$[43], $Pb_{1-x}Sn_xTe$[44]). They have larger band gap around 0.3 eV. In particular, the Bi_2Te_3, Bi_2Se_3 and Sb_2Te_3 are well-known as having a single Dirac cone on their surface, and these binary compounds are so-called tetradymite structure[45].

1.4.3 Previous researches of topological insulators

(i) Electronic band structure of bulk and surface state

• The electronic structures of V_2VI_3 compounds have been calculated using first-principles methods as high-performance thermoelectric materials and topological insulators[46]. H. Zhang *et al*. calculated the bulk and surface band structures of Bi_2Te_3, Bi_2Se_3, Sb_2Te_3, and Sb_2Se_3. The results show that the Dirac-cone-type dispersion is formed at the Γ point in the local density of states (LDOS) exist for Sb_2Se_3[41] associating with spin-orbit coupling.

・J. A. Sobota *et al*. observed the occupied and unoccupied electric structure of *n*- and *p*-type Bi_2Se_3 by one-photon photoemission (1PPE) and two-photon photoemission (2PPE) angle-resolved spectroscopy[47]. They theoretically and experimentally show that the presence of 1st surface state (SS) and 2nd SS exist only in the presence of spin-orbit coupling.

・Angle-resolved photoemission spectroscopy (ARPES) is the most useful tool to directly investigate a topological surface state. This method has been used to identify surface state of *p*-type Bi_2Se_3[48] and Bi_2Te_3[49,50].

・Y. –Y. Li *et al*. investigate the thickness limit of the single-Dirac cone surface state with ARPES and first-principle calculations[51]. The thickness dependence were measured by using Bi_2Te_3 thin films grown by molecular beam epitaxy technique on Si(111). They found that the thickness limit of the single-Dirac cone surface state is 2 quintuple layers (2QLs). In addition, the topological surface state is also visualized as energy and spatial structure of Landau levels using scanning tunneling microscopy (STM)[52-54].

(ii) Surface carrier scattering dynamics

Time- and angle-resolved photoemission spectroscopy (Tr-ARPES) is used for real-time visulalization of the transient carrier population[55]. A. Creoaldi *et al*. report that the time-dependent electronic thermal distribution after optical excitation in Bi_2Se_3[56-59]. They analyzed the distribution by using an effective Fermi-Dirac function whose temperature (T) and chemical potential (μ) relax with the relaxation time of $\tau_T \sim 2.5$ ps and $\tau_\mu \sim 2.7$ ps, respectively. The relaxation time (τ_T) is compatible with a mechanism of energy relaxation to the lattice mediated by the electron-phonon interaction, and τ_μ is related to the relaxation of the excess change in the conduction band via diffusion. J. A. Sobota *et al*. investigated the dynamics of optically excited electrons (1.5 eV) in *p*-type Bi_2Se_3 by using Tr-ARPES, they concluded the non-equilibrium population of surface state persisting for >10 ps[60]. In addition, different scattering channels of surface and bulk electrons in Bi_2Se_3 are shown by Y. H. Wang *et al*. with using Tr-ARPES[61]. Very recently, the spin and electric dynamics in Bi_2Se_3 is unveiled with using a spin-, time-, and angle- resolved photoemission

spectroscopy by C. Cacho *et al*[62]. Their results show that the surface and bulk states behave as independent electric populations after optical excitation, which is to say the photoexcited electrons relax back to equilibrium with different τ ($\tau_{TS} = 3.5$ ps, $\tau_{TB} = 6.0$ ps). Similarly, the relaxation time is obviously different between the surface and bulk states in Bi_2Te_3[63,64], and Sb_2Te_3[65]. S. Zhu *et al*. have studied the dynamics of excited electrons of Sb_2Te_3[66]. They report that the excited electrons in the upper Dirac cone stay longer than those below the Dirac point.

(iii) Spin current

The current of topological insulators in equilibrium is typically dominated by non-spin-polarized carriers of the bulk conduction band (BCB) rather than the spin-polarized carriers of the surface state[67,68]. The helical spin of the metallic surface state can be selectively excited by circular polarized laser pulses[69,70].

1.5 Objective and outline of this study

Topological insulators are a new quantum phase of matter having a Dirac-cone-type dispersion. The gapless surface states have confirmed by using ARPES, STM and STS. However there is little known about the dynamics of photoexcited electrons and phonons. Investigating these dynamics in topological insulators would be closely related with intrinsic features for electronic applications. The objective of my research is to elucidate the dynamics of photoexcited electrons and coherent phonons in the topological insulators having the tetradymite structure (Bi_2Te_3, Sb_2Te_3 and Bi_2Se_3) using femtosecond time-resolved reflectivity measurements. The near-IR transient reflectivity shows modulation due to all of the Raman-active coherent optical phonons (E_g^1, E_g^2, A_{1g}^1, and A_{1g}^2). Meanwhile, the mid-IR transient reflectivity shows the electron dynamics via both the electronic bulk and surface states. The relaxation process of the photoexcited carriers in topological insulator is also examined.

In chapter 1, I give an overview of time-domain spectroscopy, target materials and the objective of this dissertation. In chapter 2, I explain the sample characterization (sample morphology, optical properties, lattice vibrational modes) and experimental apparatus. Chapter 3 shows the dynamics of optical coherent phonons, which are investigated by transient reflectivity of the near-infrared (IR) pulse using the pump-probe technique. I obtained frequencies and decay times of all the Raman active optical phonons. Chapter 4 shows the dynamics of photo-excited carriers in Sb_2Te_3 investigated by the transient reflectivity in a mid-IR region. The lifetime of the photo-excited carriers is obtained and its relaxation dynamics is discussed. Finally, I summarized the results and show the general conclusion in chapter 5.

References

1. G. J. Snyder, and E. S. Toberer, "Complex thermoelectric materials", *Nat. Mater.*, **7**, 105 (2008).
2. R. Venkatasubramanian, E. Siivola, T. Colpitts, and B. O'Quinn, "Thin-film thermoelectric devices with high room-temperature figures of merit", *Nature*, **413**, 597 (2001).
3. M. Wuttig, and N. Yamada, "Phase-change materials for rewriteable data storage", *Nat. Mater.*, **6**, 824 (2007).
4. F. Xiao, C. Hangarter, B. Yoo, Y. Rheem, K. –H. Lee, and N. V. Myung, "Recent progress in electrodeposition of thermoelectric thin films and nanostructure", *Electrochim. Acta*, **53**, 8103 (2008).
5. T. M. Tritt, "Holey and unholy semiconductors", *Science*, **283**, 804 (1999).
6. C. B. Saiterthwaite, and R. W. Ure Jr., "Electrical and thermal properties of Bi_2Te_3", *Phys. Rev.*, **108**, 1164 (1957).
7. P. Janicek, C. Drasar, L. Benes, and P. Lost'ak, "Thermoelectric properties of TI-doped Bi2Se3 single crystals", *Cryst. Res. Technol.*, **44**, 505 (2009).
8. L. –L. Wang, and D. D. Johnson, "Ternary Tetradymite compounds as topological insulators", *Phys. Rev. B*, **83**, 241309 (2011).
9. P. Janicek, C. Drasar, L. Benes, and P. Lost'ak, "Thermoelectric properties of TI-doped Bi_2Se_3 single crystals", *Cryst. Res. Technol.*, **44**, 505 (2009).
10. Norman F. Ramsey, The Novel Prize in Physics 1989.
11. G. Hooft, and S. Vandoren, "Time in powers of ten, Natural phenomena and their timescales", World Scientific.
12. N. F. Scherer, J.L. Knee, D. D. Smith, and A. H. Zewail, "Femtosecond photofragment spectroscopy: The reaction ICN→CN+I", *J. Phys. Chem.*, **89**, 5141 (1985).
13. V. Engel, H. Metiu, R. Almeida, R. A. Marcus, and A. H. Zewail, "Molecular state evolution after excitation with an ultra-short laser pulse: a quantum analysis of NaI and NaBr dissociation", *Chem. Phys. Lett.*, **152**, 1 (1988).
14. R. M. Bowman, M. Dantus, and A. H. Zewail, "Femtochemistry of the reaction:

IHgI*→[IHg…I]*→HgI+I", *Chem. Phys. Lett.*, **156**, 131 (1989).

15. A. Zewail, The Novel Prize in Chemistry 1999.
16. S. De Silvestri, J. G. Fujimoto, E. P. Ippen, E. B. Gamble Jr., L. R. Williams, and K. A. Nelson, "Femtosecond time-resolved measurements of optic phonon dephasing by impulsive stimulated Raman scattering in α-Perylene crystal from 20 to 300K", *Chem. Phys. Lett.*, **116**, 146 (1985).
17. T. K. Cheng, S. D. Brorson, and A. S. Kazeroonian, *Appl. Phys. Lett.*, **57**, 1004 (1990).
18. H. Katsuki, J. C. Delagnes, K. Hosaka, K. Ishioka, H. Chiba, E. S. Zijlstra, M. E. Garcia, H. Takahashi, K. Watanabe, M. Kitajima, Y. Matsumoto, K. G. Nakamura, and K. Ohmori, "All-optical control and visualization of ultrafast two-dimensional atomic motions in a single crystal of bismuth", *Nat. Commun.*, **4**, 2801 (2013).
19. G. C. Cho, W. Kütt, and H. Kurz, "Subpicosecond time-resolved coherent-phonon oscillation in GaAs", *Phys. Rev. Lett.*, **65**, 764 (1990).
20. W. Albrecht, Th. Kruse, and H. Kurz, "Time-resolved observation of coherent phonons in superconducting $YBa_2Cu_3O_{7-}\delta$ thin films", *Phys. Rev. Lett.*, **69**, 1451 (1992).
21. H. Takahashi, K. Kato, H. Nakano, M. Kitajima, K. Ohmori, and K. G. Nakamura, "Optical control and mode selective excitation of coherent phonons in $YBa_2Cu_3O_{7-}\delta$", *Solid State Commun.*, **149**, 1955 (2009).
22. H. J. Zeiger, J. Vidal, T. K. Cheng, E. P. Ippen, G. Dresselhaus, and M. S. Dresselhaus, "Theory for displacive excitation of coherent phonons", *Phys. Rev. B*, **45**, 768 (1992).
23. A. V. Kuznetsov, and C. J. Stanton, "Theory of coherent phonon oscillations in semiconductors", *Phys. Rev. Lett.*, **73** (1994) 3243.
24. R. Marlin, "Generating coherent THz phonons with light pulses", *Solid State Commun.*, **102** (1997) 207.
25. K. G. Nakamura, Y. Shikano, and Y. Kayanuma, "Influence of pulse width and detuning on coherent phonon generation", *Phys. Rev. B*, **92** (2015) 144304.
26. G. L. Eesley, "Observation of nonequillibrium electron heating in copper", *Phys. Rev. Lett.*, **51**, 2140 (1983).
27. R. W. Schoenlein, W. Z. Lin, and J. G. Fujimoto, "Femtosecond studies of nonequillibrium electronic processes in metals", *Phys. Rev. Lett.*, **58**, 1680 (1987).
28. S. D. Brorson, A. Kazeroonian, J. S. Moodera, D. W. Face, T. K. Cheng, E. P. Ippen, M. S.

Dresselhaus, and G. Dresselhaus, "Femtosecond room-temperature measurement of the electron-phonon coupling constant λ in metallic superconductors", *Phys. Rev. Lett.*, **64**, 2172 (1990).

29. K. S. Novoselov, A. K. Geim, S. V. Morozov, D. Jiang, Y. Zhang, S. V. Dubonos, I. V. Grigorieva, and A. A. Firsov, "Electric field effect in atomically thin carbon films", *Science*, **306**, 666 (2004).
30. A. K. Geim and K. S. Novoselov, "The rise of graphene", *Nature Mater*., **6**, 183 (2007).
31. A. Geim and K. Novoselov, The Novel Prize in Physics 2010.
32. M. Z. Hasan, and C. L. Kane, "Colloquium: Topological insulators", *Rev. Mod. Phys.*, **82**, 3045, (2010).
33. A. Kitaev, and J. Preskill, "Topological entanglement entropy", *Phys. Rev. Lett.*, **96**, 110404 (2006).
34. C. L. Kane and E. J. Mele, "Quantum spin hall effect in graphene", *Phys. Rev. Lett.*, **95**, 226801 (2005).
35. L. Fu and C. L. Kane, "Topological insulators with inversion symmetry", *Phys. Rev. B*, **76**, 045302 (2007).
36. S. Murakami, "Phase transition between the quantum spin Hall and insulator phases in 3D: emergence of a topological gapless phase", *New J. Phys*., **9**, 356 (2007).
37. M. König, S. Wiedmann, C. Brünr, A. Roth, H. Buhmann, L. W. Molenkamp. X. –L. Qi, and S. –C. Zhang, "Quantum spin hall insulator state in HgTe quantum wells", *Science*, **318**, 766 (2007).
38. I. Knez, R. –R. Du, and G. Sullivan, "Evidence for helical edge modes in inverted InAs/GaSb quantum wells", *Phys. Rev. Lett*., **107**, 136603 (2011).
39. D. Hsieh, D. Qian, L. Wray, Y. Xia, Y. S. Hor, R. J. Cava, and M. Z. Hasan, "A topological Dirac insulator in a quantum spin hall phase", *Nature*, **452**, 970 (2008).
40. M. König, H. Buhmann, L. W. Molenkamp, and Taylor Hughes, "The quantum spin hall effect: Theory and experiment", *J. Phys. Soc. Jpn*., **77** (2008) 031007.
41. H. Zhang, C. –X. Liu, X. –L. Qi, X. Dai, Z. Fang, and S. –C. Zhang, "Topological insulators in Bi_2Se_3, Bi_2Te_3 and Sb_2Te_3 with a single Dirac cone on the surface", *Nat. Phys*., **5** ,438 (2009).
42. J. Zhang, C. –Z. Chang, Z. Zhang, J. Wen, X. Feng, K. Li, M. Liu, K. He, L. Wang, X.

Chen, Q. –K, Xue, X. Ma, and Y. Wang, "Band structure engineering in $(Bi_{1-x}Sb_x)_2Te_3$ ternary topological insulators", *Nature Commun.*, **2**, 574 (2011).

43. Z. Ren, A. A. Taskin ,S. Sasaki, K. Segawa, and Y. Ando, "Optimizing $Bi_{2-x}Sb_xTe_{3-y}Se_y$ solid solutions to approach the intrinsic topological insulator regime", *Phys. Rev. B*, **84**, 165311 (2011).
44. S. -Y. Xu, C. Liu, N. Alidoust, M. Neupane, D. Qian, I. Belopolski, J. D. Denlinger, Y. J. Wang, H. Lin, L. A. Wray, G. Landolt, B. Slomski, J. H. Dil, A. Marcinkova, E. Morosan, Q. Gibson, R. Sankar, F. C. Chou, R. J. Cava, A. Bansil, and M. Z. Hasan, "Observation of a topological crystalline insulator phase and topological phase transition in $Pb_{1-x}Sn_xTe$", *Nature Commun.*, **3**, 1192 (2012).
45. H. Lin, T. Das, L. A. Wray, S. –Y. Xu, M. Z. Hasan, and A. Bansil, "An isolated Dirac cone on the surface of ternary tetradymite-like topological insulators", *New J. Phys.*, **13**, 095005 (2011).
46. G. Wang, and T. Cagin, "Electric structure of the thermoelectric materials $Bi_2Te_3$and Sb_2Te_3 from first-principles calculations", *Phys. Rev. B*, **76**, 075201 (2007).
47. J. A. Sobota, S. –L. Yang, A. F. Kemper, J. J. Lee, F. T. Schmitt, W. Li, R. G. Moore, J. G. Analytis, I. R. Fisher, P. S. Kirchmann, T. P. Devereaux, and Z. –X. Shen, "Direct optical coupling to an unoccupied Dirac state in the topological insulator Bi_2Se_3", *Phys. Rev. Lett.*, **111**, 136802 (2013).
48. Y. Xia, D. Qian, D. Hsigh, L. Wray, A. Pal, H. Lin, A. Bansil, D. Grauer, Y. S. Hor, R. J. Cava, and M. Z. Hasan, "Observation of a large-gap topological-insulator class with a single Dirac cone on the surface", *Nat. Phys.*, **5**, 398 (2010).
49. Y. L. Chen, J. G. Analytis, J. –H. Chu, Z. K. Liu, S. –K. Mo, X. L. Qi, H. J. Zhang, D. H. Lu, X. Dai, Z. Fang, S. C. Zhang, I. R. Fisher, Z. Jussain, Z. –X. Shen, "Experimental realization of a three-dimensional topological insulator Bi_2Te_3", *Science*, **325**, 178 (2009).
50. D. Hsieh, Y. Xia, D. Qian, L. Wray, J. H. Dil, F. Meier, J. Osterwalder, L. Patthey, J. G. Checkelsky, N. P. Ong, A. V. Fedorov, H. Lin, A. Bansil, D. Grauer, Y. S. Hor, R. J. Cava, and M. Z. Hasan, "A tunable topological insulator in the spin helical Dirac transport regime", *Nature*, **460**, 1101 (2009).
51. Y. –Y. Li, G. Wang, X. –G. Zhu, M. –H. Liu, C. Ye, X. Chen, Y. –Y. Wang, K. He, L. –L. Wang, X. –C. Ma, H. –J. Zhang, X. Dai, Z. Fang, X. –C. Xie, Y. Liu, X. –L. Qi, J. –F. Jia, S.

–C. Zhang, and Q. –K. Xue, “Intrinsic topological insulator Bi2Te3 thin films on Si and thickness limit”, *Adv. Mater*., **22**, 4002 (2010).

52. P. Roushan, J. Seo, C. V. Parker, Y. S. Hor, D. Hsieh, D. Qian, A. Richardella, M. Z. Hasan, R. J. Cava, and Ali Yazdani, “Topological surface states protected from backscattering by chiral spin texture”, *Nature*, **460**, 1106 (2009).
53. Z. Alpichshev, J. G. Analytis, J. –H. Chu, I. R. Fisher, Y. L. Chen, Z. X. Shen, A. Fang, and A. Kapitulnik, “STM imaging of electric waves on the surface of Bi_2Te_3: Topologically protected surface states and hexagonal warping effects”, *Phys. Rev. Lett.*, **104**, 016401 (2010).
54. Y. –S. Fu, M. Kawamura, K. Igarashi, H. Takagi, T. Hanaguri, and T. Sasagawa, “Imaging the two-component nature of Dirac-Landau levels in the topological surface state of Bi_2Se_3”, *Nat. Phys*., **10**, 815 (2014).
55. D. Niesner, S. Otto, V. Hermann, Th. Fauster, T. V. Menshchikova, S. V. Eremeev, Z. S. Aliev, I. R. Amiraslanov, M. B. Babanly, P. M. Echenique, and E. V. Chylkov, “Bulk and surface electron dynamics in a *p*-type topological insulator $SnSb_2Te_4$”, *Phys. Rev. B*, **89**, 081404(R) (2014).
56. A. Creoaldi, B. F. Cilento, M. Zacchigna, C. Grazioli, H. Berger, Ph. Bugnon, K. Kern, M. Grioni, and F. Parmigiani, “Ultrafast photodoping and effective Fermi-Dirac particles in Bi_2Se_3”, *Phys. Rev. B*, **86**, 205133 (2012).
57. A. Crepaldi, B. Ressel, F. Cilento, M. Zacchigna, C. Grazioli, H. Berger, Ph. Bugnon, K. Kern, M. Grioni, and F. Parmigiani, “Ultrafast photodoping and effective Fermi-Dirac distribution of the Dirac particles in Bi_2Se_3”, *Phys. Rev. B*, **86**, 205133 (2012).
58. A. Crepaldi, F. Cilento, B. Ressel, C. Cacho, J. C. Johannsen, M. Zacchigna, H. Berger, Ph. Bugnon, C. Grazioli, I. C. E. Turcu, E. Springate, K. Kern, M. Grioni, and F. Parmigiani, “Evidence of reduced surface electron-phonon scattering in the conduction band of Bi_2Se_3 by nonequilibrium ARPES”, *Phys. Rev. B*, **88**, 121404 (2013).
59. J. A. Sobota, S. Yang, J. G. Analytis, Y. L. Chen, I. R. Fisher, P. S. Kirchmann, and Z. –X. Shen, “Ultrafast optical excitation of a persistent surface-state population in the topological insulator Bi_2Se_3”, *Phys. Rev. Lett.*, **108**, 117403 (2012).
60. Y. H. Wang, D. Hsieh, E. J. Sie, H. Steinberg, D. R. Gardner, Y. S. Lee, P. Jarillo-Herrero, and N. Gedik, “Measurement of intrinsic Dirac Fermion cooling on the surface of the

topological insulator Bi_2Se_3 using time-resolved and angle-resolved photoemission spectroscopy", *Phys. Rev. Lett.*, **109**, 127401 (2012).

61. C. Cacho, A. Crepaldi, M. Battiato, J. Braun, F. Cilento, M. Zacchigna, M. C. Richter, O. Heckmann, E. Springate, Y. Liu, S. S. Dhesi, H. Berger, Ph. Bugnon, K. Held, M. Grioni, H. Ebert, K. Hricovini, J. Minar, and F. Parmigiani, "Momentum-resolved spin dynamics of bulk and surface excited states in the topological insulator Bi_2Se_3", *Phys. Rev. Lett.*, **114**, 097401 (2015).
62. M. Hajlaoui, E. Papalazarou, J. Mauchain, G. Lantz, N. Moisan, D. Boschetto, Z. Jiang, I. Miotkowski, Y. P. Chen, A. Taleb-Ibrahimi, L. Perfetti, and M. Marsi, "Ultrafast surface carrier dynamics in the topological insulator Bi_2Te_3", *Nano Lett*., **12**, 3532 (2012).
63. M. Hajlaoui, E. Papalazarou, J. Mauchain, L. Perfetti, A. Taleb-Ibrahimi, F. Navarin, M. Monteverde, P. Auban-Senzier, C. R. Pasquier, N. Moisan, D. Boschetto, M. Neupane, M. Z. Hasan, T. Durakiewicz, Z. Jiang, Y. Xu, I. Miotkowski, Y. P. Chen, S. Jia, H. W. Ji, R. J. Cava, and M. Marsi, "Tuning a Schottky barrier in a photoexcited topological insulator with transient Dirac cone electron-hole asymmetry", *Nat. Commun*., **5**, 3003 (2014).
64. J. Reimann, J. Güdde, K. Kuroda, E. V. Chulkov, and U. Höfer, "Spectroscopy and dynamics of unoccupied electric states of the topological insulators Sb_2Te_3 and Sb_2Te_2S", *Phys. Rev. B*, **90**, 081106(R) (2014).
65. S. Zhu, Y. Ishida, K. Kuroda, K. Sumida, M. Ye, J. Wang, H. Pan, M. Taniguchi, S. Qiao, S. Shin, and A. Kimura, "Ultrafast electron dynamics at the Dirac node of the topological insulator Sb_2Te_3", *Sci. Rep*., **5**, 13213 (2015).
66. J. G. Analytis, R. D. McDonald, S. C. Riggs, J. –H. Chu, G. S. Boebinger, and I. R. Fisher, "Two-dimensional surface state in the quantum limit of a topological insulator", *Nat. Phys*., **6**, 960 (2010).
67. N. P. Butch, K. Kirshenbaum, P. Syers, A. B. Sushkov, G. S. Jenkins, H. D. Drew, and J. Paglione, "Strong surface scattering in ultrahigh-mobility Bi2Se3 topological insulator crystals", *Phys. Rev. B*, **81**, 241301 (2010).
68. D. Hsieh, F. Mahmood, J. W. McIver, D. R. Gardner, Y. S. Lee, and N. Gedik, "Selective probing of photoinduced charge and spin dynamics in the bulk and surface of a topological insulator", *Phys. Rev. Lett.*, **107**, 077401 (2011).
69. J. W. McIver, D. Hsieh, H. Steinberg, P. Jarillo-Herrero, and N. Gedik, "Control over

topological insulator photocurrents with light polarization", *Nat Nanotech.*, **7**, 96 (2012).

70. Y. Li, V. A. Stoica, L. Endicott, G. Wang, C. Uher, and R. Clarke, "Coherent optial phonon spectroscopy studies of femtosecond-laser modified Sb_2Te_3 films", *Appl. Phys. Lett.*, **97**, 171908 (2010).

Chapter 2.
Sample characterization and experimental detail

In this chapter, some characterizations of sample materials (Bi_2Se_3, Bi_2Te_3, and Sb_2Te_3 single crystals) are presented. The following section consists of three parts: (1) crystal structure observed with X-ray diffraction and sample preparation in various types of thickness, (2) basic optical properties such as band gap, reflectance, penetration depth, and (3) lattice vibrational modes. In addition, the experimental apparatus are described.

2.1 Sample preparation and characterization

2.1.1 Crystal structure

Chalcogenide compounds (Sb_2Te_3, Bi_2Se_3 and Bi_2Se_3) have a rhombohedral structure in space group of D_{3d}^5 ($R\bar{3}m$)[1]. As shown in Fig. 2-1, the atomic arrangement along the *c*-axis has repeating units with five-atomic –Te(1)–Sb–Te(2)–Sb–Te(1)– layers called quintuple layers[2].

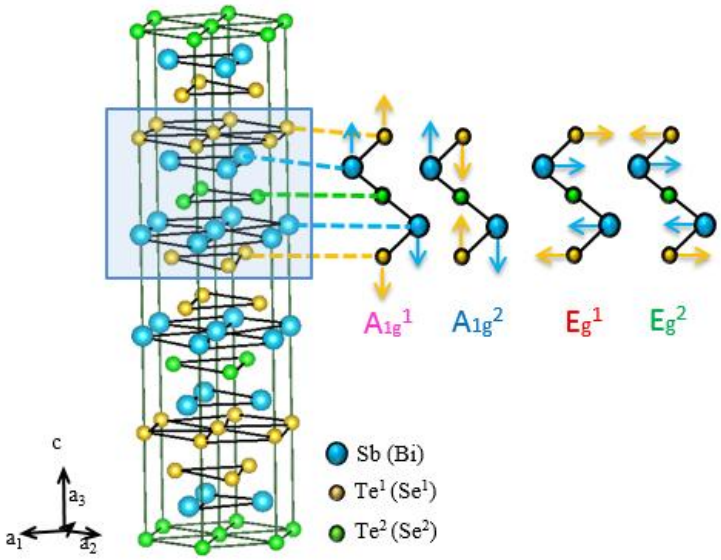

Fig. 2-1 Crystal structure of topological insulator (Sb_2Te_3, Bi_2Te_3 and Bi_2Se_3) and the four Raman-active optical phonon mode in quintuple layer: images of the out-of-plane $A_{1g}^{\ 1}$ and $A_{1g}^{\ 2}$ modes and in-plane $E_g^{\ 1}$ and $E_g^{\ 2}$ modes.

Figure 2-2 shows a typical example of the single crystal X-ray diffraction pattern of Sb_2Te_3 measured with a conversional X-ray diffractometer (D8 Discover BRUKER). The sheet-like-shaped crystal has a (0001) orientation of the plane normal to the surface (Fig. 2-2(a)) and an in-plane trigonal structure (Fig. 2-2(b)). The unit cell parameters of Sb_2Te_3 were 0.426 and 3.046 nm for *a* and *c* axes, respectively[3]. The bonds between quintuple layers are connected by a very weak van der Waals force; therefore, it can be easily cleaved at the Te(1)–Te(1) interface.

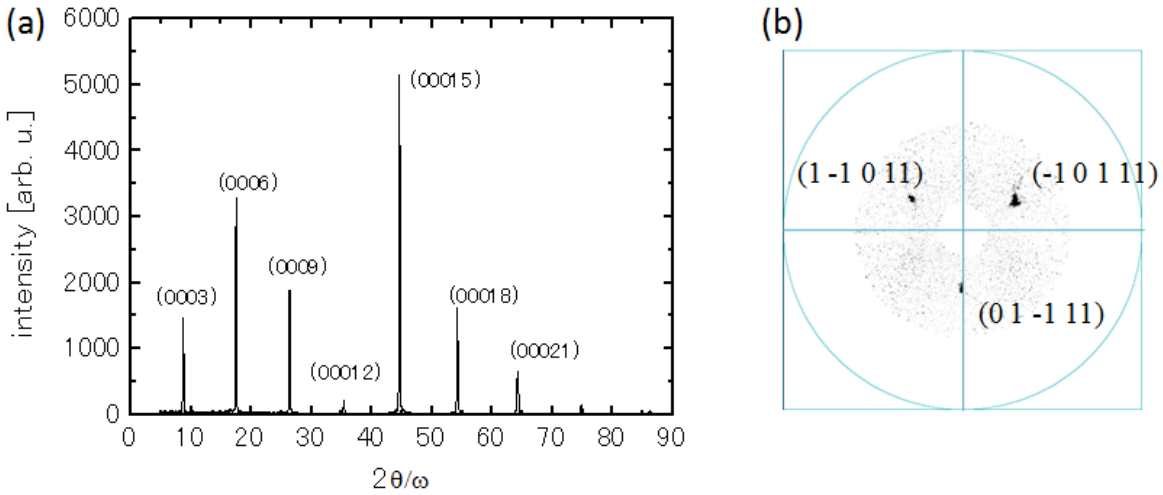

Fig. 2-2 X-ray diffraction pattern of Sb_2Te_3 along the (0001) orientation of (a) the plane normal to the surface and (b) the in-plane trigonal structure.

2.1.2 Sample preparation

Single crystals of Bi_2Se_3, Bi_2Te_3, and Sb_2Te_3 were grown by a modified Bridgman technique at Sasagawa Laboratory in Materials and Structure Laboratory of Tokyo Institute of Technology. The Bridgman technique is a popular method for producing large single crystal to grow semiconductor crystals with using temperature gradient[4]. The mixture of Bismuth, Selenium, Tellurium or Antimony were raised to melt and slowly cooling in a crucible.

2.1.3 Sample morphology

(i) Bulk sample

Figure 2-3 shows the surface images of the Bi_2Se_3 single crystal obtained by a laser microscope (KEYENCE VK-8550). For all of the experiments, I prepared a fresh surface by cleaving the sample with an adhesive tape. As shown in Fig. 2-3(a) and (b), the sample has a flat and metallic-color surface. The thickness of this bulk sample measured to be approximately 46 μm (Fig. 2-3(c)). Similarly, the thicknesses of bulk samples in Bi_2Te_3 and Sb_2Te_3 are obtained approximately 31 μm and 29 μm, respectively.

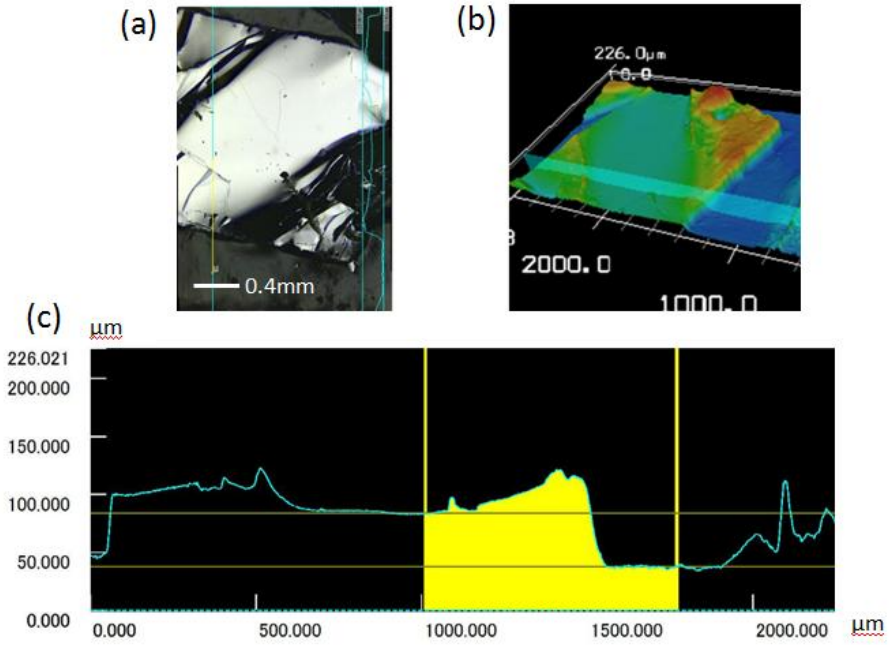

Fig. 2-3 The laser microscope images of Bi_2Se_3 single crystal, (a) metal-like and (b) flat surface, and (c) the bulk sample thickness of 46 μm.

(ii) Thin-film (<100 nm)

Topological insulators have a layered structure, thus these crystals were easily cleaved perpendicular to the *c*-axis. The thin-film sample was prepared with a Microtome on copper-mesh substrate to be used for time-resolved electron diffraction experiment[5]. I could slice only the Bi_2Te_3 single crystal with the thickness of 30 nm because of the hardness of the samples.

(iii) Ultra thin-film (<10 nm)

One of the main topics of this study is to investigate the surface and bulk of the topological insulators from the viewpoint of the electronic and phononic dynamics. Hence, I tried three kinds of method to prepare the ultrathin-topological insulators and measure the photo-excited coherent phonon modes on these ultrathin films. The surface of topological insulators Figure 2-4(a) displays the thin-film prepared by exfoliation. The bulk samples are exfoliated at least 10 times by an adhesive tape[6]. The thickness of the ultra thin-film is estimated from the laser fluencies as shown in Fig. 2-4(b). Using the reported refractive index (5.7-3.3*i*)[7], the sample thickness is determined to be 3 nm.

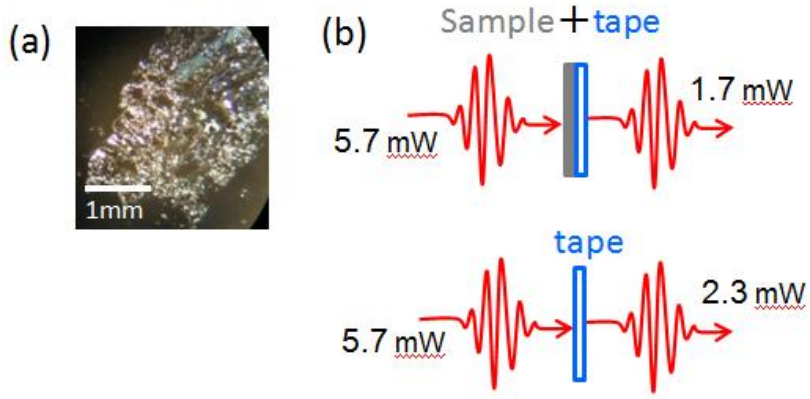

Fig. 2-4 (a) Optical microscope image of exfoliated sample (Sb_2Te_3). (b) Method of estimated the thickness of ultra thin-film.

Figure 2-5 shows a SEM image of the gold nano particles evapolated surface of Bi_2Se_3. Gold nano-particles will enhance the surface electric field[8], which will provide the properties of surface of topological insulators. The final idea is to make a-few-layered flakes with sonication in the organic solvents (N-methyl-2-pyrrolidone, NMP)[9].

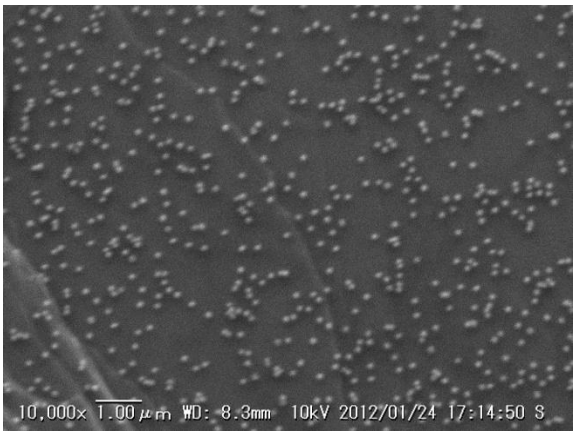

Fig. 2-5 SEM image of Bi_2Se_3 to evaporate gold nano-particles on the sample surface.

2.1.4 Carrier concentration

The intrinsic carrier density of the prepared samples is obtained from the Hall coefficient[10]. Figure 2-6 shows a typical result of the Hall measurement of Sb_2Te_3 at

room temperature (Quantum Design PPMS). The hall resistance (ρ_{xy}) linearly increases along the applied magnetic field up to 5 T.

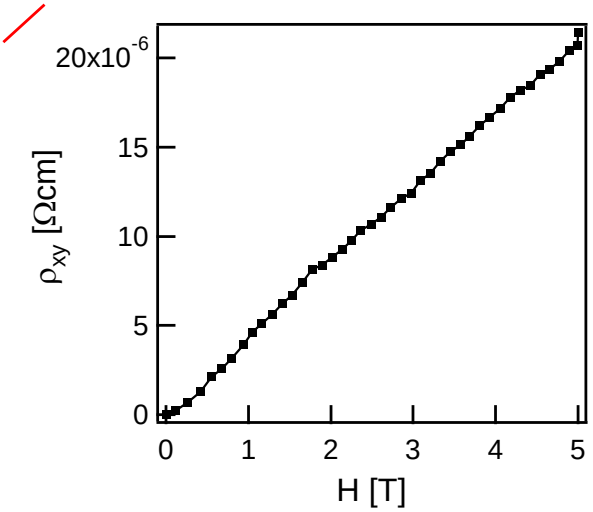

Fig. 2-6 Hall resistance measurement of Sb_2Te_3 in the magnetic field of 0 to 5 T at room temperature.

The Hall coefficient (R_H) is obtained$R_H = 8.18 \times 10^{-16}$ Ωcm/T. The Hall carrier concentration can be calculated as

$$n = {}^{1}/_{R_H e} \ . \tag{2.1}$$

Thus, the Hall carrier concentration is$n = 7.63 \times 10^{19}$ cm^{-3}. This result indicates that the carrier is hole (the sample is a *p*-type semiconductor). In addition, the carrier concentration of surface state can be estimated from ARPES by following equation [11]

$$n_{surface} = {K_F}^2/_{4\pi} \ , \tag{2.2}$$

where K_F is the Fermi wave number. The carrier concentration of surface state is $n = 0.50 \times 10^{13} cm^{-2}$, which refer to the ARPES spectrum of Sb_2Te_3 ($K_F = 0.08$ Å^{-1}). The carrier concentration is the same order of magnitude as previous report of *n*-type Bi_2Se_3[10]. The carrier densities of the other samples (*n*-type Bi_2Se_3 and *n*-type Bi_2Te_3) are $n = 1 \times 10^{18}$ cm^{-3} and $n = 3 \times 10^{18}$ cm^{-3}, respectively[12].

2.1.5 Energy band gap and optical properties

Optical properties of samples are obtained from optical transmission and

reflection spectra. Figure 2-7 shows a typical example of the transmission spectrum of Sb_2Te_3 single crystal (thickness of the order of few μm)[13]. The transmission spectrum was measured between 0.22 and 0.60 eV. The transmittance decreases rapidly at the photon energy of 0.33 eV as the photon energy increases, thus the band gap is determined to be 0.33 eV. The transmission spectrum of Bi_2Te_3 is also shown in Fig. 2-8 and the band gap is determined to be 0.13 eV[14]. As shown in Fig. 2-9, the band bap is not related with the sample temperature [14].

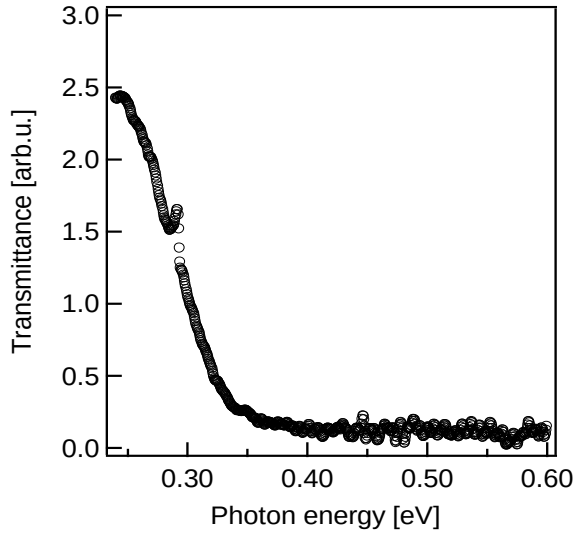

Fig. 2-7 Infrared transmission spectrum of Sb_2Te_3 single crystal.

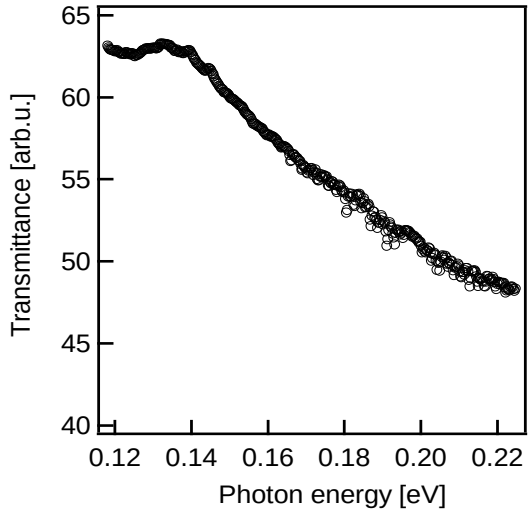

Fig. 2-8 Infrared transmission spectrum of Bi_2Te_3 single crystal.

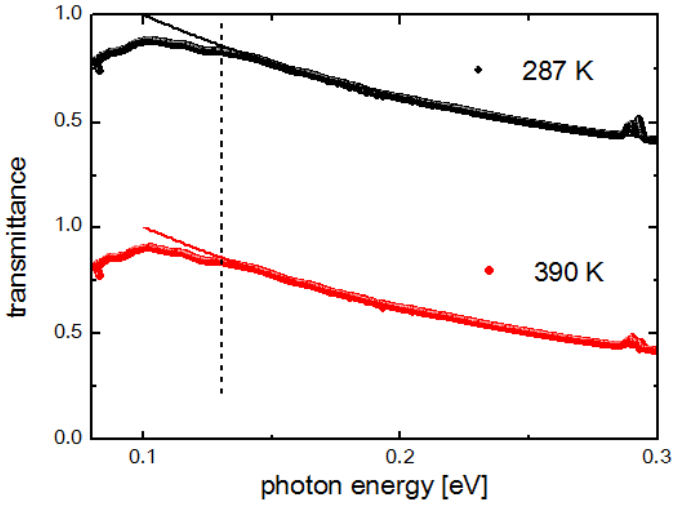

Fig. 2-9 Infrared transmission spectra of Bi_2Te_3 at the temperature of 287 K and 390 K.

One of the most popular methods to find optical parameters is the measurement of specular reflectance. As shown in Fig. 2-10, the static reflectivity spectrum of Sb_2Te_3 was measured in the photon energy range between 0.1 and 0.8 eV[14] (Thermo Scientific, Nicolet 6700). It is found that the plasma frequency of Sb_2Te_3 is $\omega_p = 1.08\,\text{eV}$ with analyzing Drude-Lorentz model[15], the detail will be described later (chapter 4).

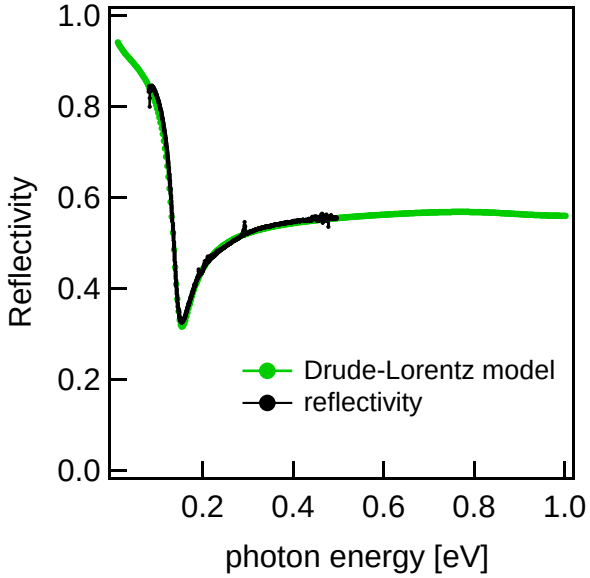

Fig. 2-10 Infrared reflectivity spectrum of Sb_2Te_3; experimental data (black dot) and fitting curve with Drude-Lorentz modes (green line).

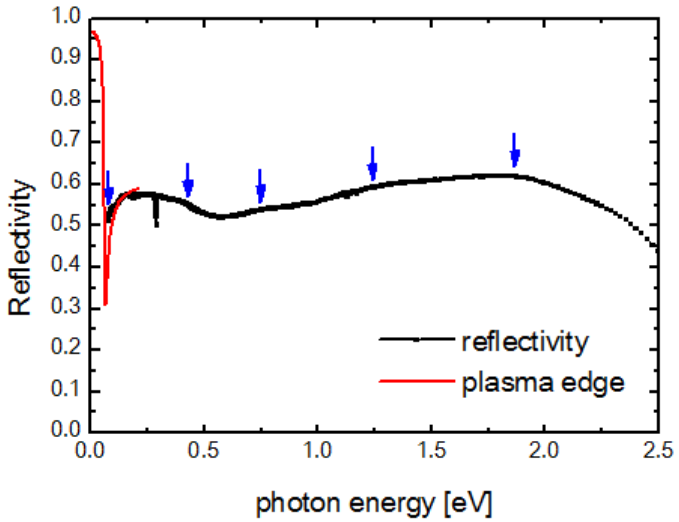

Fig. 2-11 Infrared reflectivity spectrum of Bi_2Te_3; experimental data (black dot) and plasma edge calculated using the Kramers-Kronig transformation of the reflectivity spectrum (red line).

Figure 2-11 shows a reflectivity spectrum from Bi_2Te_3 measured in the energy range from 0.08 to 2.5 eV at room temperature. Blue markers (arrows) indicate the kink positions corresponding to the allowed electron transitions from the valence band. We calculated optical conductivity using the Kramers-Kronig (KK) transformation of the reflectivity spectrum assuming the extrapolation of plasma edge structure due to the response of the free carrier in the surface state for the low energy region as shown by the red line (below 0.08 eV). The indirect bandgap of the Bi_2Te_3 is determined to be 0.13 eV.

The penetration depth of the pump pulse is described as

$$\alpha = \frac{4\pi k}{\lambda} \tag{2.3}$$

where α is absorption coefficient, k is extinction coefficient, and λ is wavelength. In the wavelength of 800 nm, the extinction coefficient of Bi_2Te_3 and Sb_2Te_3 are $k = 5.5$ and $k = 3.3$, respectively[7,16]. Therefore, the penetration depth of pump pulse in Bi_2Te_3 and Sb_2Te_3 are 12 nm and 19 nm, respectively.

2.1.6 Lattice vibrational modes

Raman spectroscopy is a popular method to observe vibrational modes in

molecules and crystals. Optical phonons of the prepared samples (Sb_2Te_3, Bi_2Te_3 and Bi_2Se_3) were examined via Raman scattering at thermal equilibrium conditions. The Raman spectroscopy was performed with a micro-Raman spectrometer (Horiba-JY T64000) in backscattering configuration with 514.5 nm laser light[17]. The optical phonon modes of topological insulators at the Γ point consist of $2(A_{1g}+E_g) + 3(E_u+A_{2u})$, where the A_{1g} and E_g phonons are Raman active while the E_u and A_{2u} phonons are infrared active. The Raman-active A_{1g} modes ($A_{1g}^1$and A_{1g}^2) are out-of-plane vibrational mode, in contract the E_g modes (E_g^1 and E_g^2) are in-plane vibrational modes, as shown in Fig. 2-1.

Figures 2-12 – 2-14 present the Raman spectra of Sb_2Te_3, Bi_2Se_3 and Bi_2Te_3, respectively. The Raman spectrum of Sb_2Te_3 (Fig. 2-13) shows four peaks at 1.2 THz (41 cm^{-1}), 2.0 THz (68 cm^{-1}), 3.4 THz (114 cm^{-1}), and 5.0 THz (166 cm^{-1}), which are assigned to the Raman-active E_g^1, A_{1g}^1, E_g^2, and A_{1g}^2 phonons of bulk Sb_2Te_3, respectively[18-20].

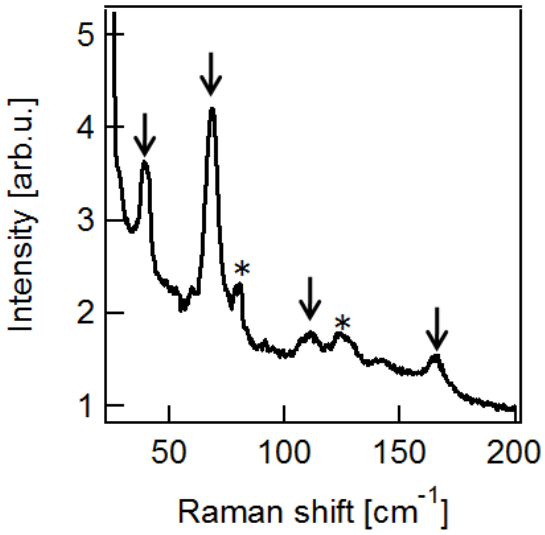

Fig. 2-12 Raman spectrum of Sb_2Te_3 showing four peaks at 41 cm^{-1} (1.2 THz), 68 cm^{-1} (2.0 THz), 114 cm^{-1} (3.4 THz), and 166 cm^{-1} (5.0 THz), which are assigned to E_g^1, A_{1g}^1, E_g^2, and A_{1g}^2 modes, respectively. The small peaks marked with asterisks (*) may be because of the E_u^1 and E_u^2 modes.

The Raman spectrum of Bi_2Te_3 (Fig. 2-13) shows also four peaks at 1.2 THz (40 cm^{-1}), 1.8 THz (61 cm^{-1}), 3.0 THz (101 cm^{-1}) and 4.0 THz (132 cm^{-1}), which are identified as E_g^1, A_{1g}^1, E_g^2, and A_{1g}^2 modes, respectively[19,20].

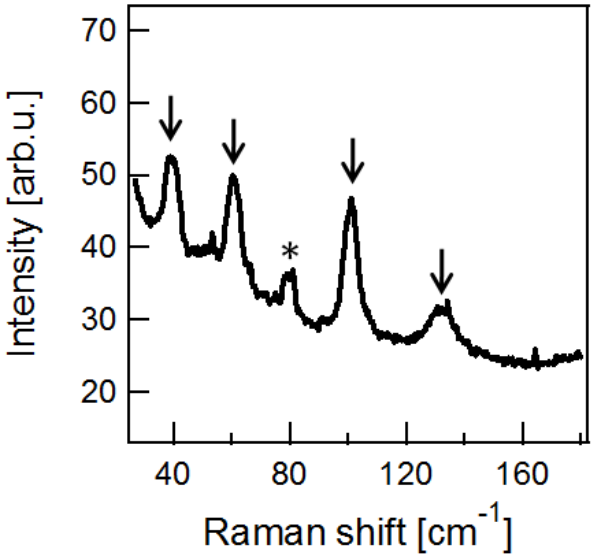

Fig. 2-13 Raman spectrum of Bi_2Te_3 showing four peaks at 40 cm^{-1} (1.2 THz), 61 cm^{-1} (1.8 THz), 101 cm^{-1} (3.0 THz), and 132 cm^{-1} (4.0 THz), which are assigned to E_g^1, A_{1g}^1, E_g^2, and A_{1g}^2 modes, respectively. The small peak marked with asterisks (*) may be because of the E_u^1 modes.

The Raman spectrum of Bi_2Se_3 as shown in Fig. 2-14 shows also four Raman active modes, 1.2 THz (40 cm^{-1}: E_g^1), 2.1 THz (71 cm^{-1}: A_{1g}^1), 3.9 THz (130 cm^{-1}: E_g^2) and 5.2 THz (173 cm^{-1}: A_{1g}^2). These results agree well with the previous reports[19,20].

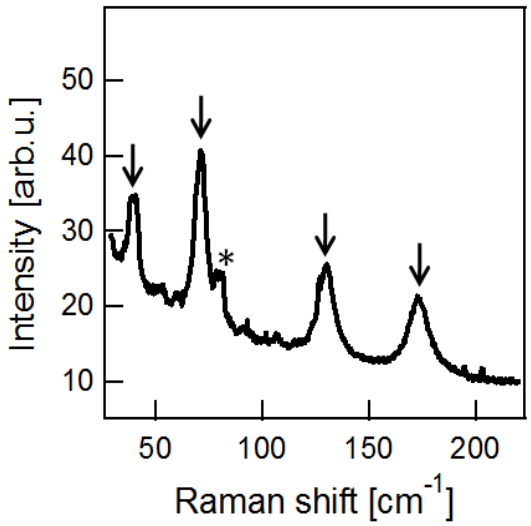

Fig. 2-14 Raman spectrum of Bi_2Se_3 showing four peaks at 40 cm^{-1} (1.2 THz), 71 cm^{-1} (2.1 THz), 130 cm^{-1} (3.9 THz), and 173 cm^{-1} (5.2 THz). The small peak marked with asterisks may be because of the E_{1u} modes.

Table 2-1 Ramans active optical phonon modes

mode	E_g^1		A_{1g}^1		E_g^2		A_{1g}^2	
	[cm^{-1}]	[THz]	[cm^{-1}]	[THz]	[cm^{-1}]	[THz]	[cm^{-1}]	[THz]
Sb_2Te_3	41	1.2	68	2.0	114	3.4	166	5.0
Bi_2Te_3	40	1.2	61	1.8	101	3.0	132	4.0
Bi_2Se_3	40	1.2	71	2.1	130	3.9	173	5.2

2.2 Ultrashort laser pulses

In ultrafast spectroscopy, it is necessary to precisely determine a pulse duration, which affects temporal resolution. There are several ways to evaluate the pulse duration, for example, interferometric autocorrelation, fringe-resolved autocorrelation (FRAC), frequency-resolved optical gating (FROG) and spectral phase interferometry for direct electric-field reconstruction (SPIDER). Here, I introduce the interferometric autocorrelation and FRAC systems used in my experiments.

2.2.1 Autocorrelation

The simplest and a widely used technique for evaluating the femtosecond laser-pulse width is a second harmonic generation (SHG) intensity autocorrelation (Fig. 2-15). An optical pulse derived from a femtosecond laser system is divided into two replica pulses with separation time τ. These two replica pulses have to make spatially overlapped in a nonlinear optical crystal such as BBO (β–BaB_2O_4) crystal. The oscillating electric field of a laser pulse is

$$E(t) = E_0(t)exp\left[-i\left(\omega_0 t - \phi(\omega)\right)\right] \quad (2.4)$$

where $E_0(t)$ is a pulse envelope function, $\phi(\omega)$ is the spectral phase. The pulse intensity can be written as

$$I(t) = E(t)E(t) = E_0(t)E_0^*(t) \quad (2.5).$$

The Intensity autocorrelation as a function of time-delay (τ) is expressed as following:

$$E_{SH} = \int_{-\infty}^{\infty} I(t)I(t-\tau)dt\ . \quad (2.6)$$

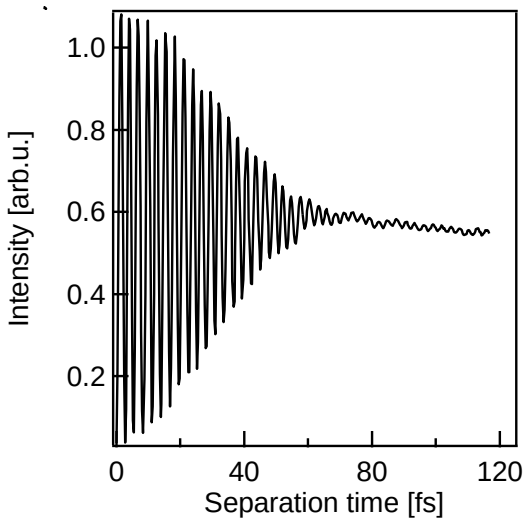

Fig. 2-15 Intensity of optical interferometric between double pump pulses as a function of separation time.

2.2.2 Fringe-resolved autocorrelation (FRAC)

A fringe-resolved autocorrelation (FRAC) is a popular method to measure an ultrashort optical pulse duration [21,22]. The FRAC signal involves in the second harmonic signal as a function of delay time between autocorrelation pulses at the output of a Michelson interferometer as shown in Fig. 2-16. The two phase-locked pulses induced by a Michelson-type interferometer have optically difference path length. The expression for FRAC trace for a given delay is

$$I_{\mathrm{FAC}}(\tau) = \int_{-\infty}^{\infty} ||E(t) + E(t-\tau)|^2|^2 \; dt$$

$$= \int_{-\infty}^{\infty} |E(t)^2 + 2E(t)E(t-\tau) + E(t-\tau)^2|^2 \; dt \; . \qquad (2.7)$$

The integrals of $E(t)^2$ and $E(t-\tau)^2$ are SHG of each individual pulses. The term of $E(t)E(t-\tau)$ is the second harmonic interferogram of these two pulses.

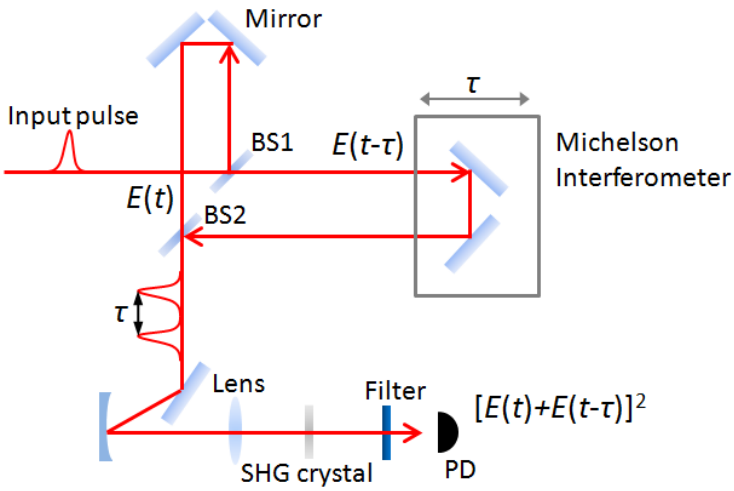

Fig. 2-16 Schematic of the fringe-resolved autocorrelation (FRAC). BS, beam splitters; PD, photodetector.

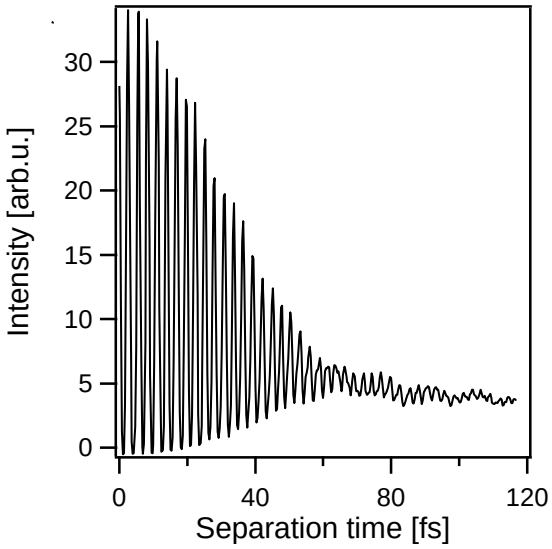

Fig. 2-17 fringe-resolved autocorrelation (FRAC) trace in this measurements.

2.3 Pump-probe spectroscopy

Optical pump-probe spectroscopy is the popular method in femtosecond time-resolved spectroscopy. General description of this method is following; an output pulses derived from Ti:Sapphire laser system is divided into two pulses, one is used to excite the materials (pump pulse), and the other pulse (probe pulse) is used to detect the

modulations induced by pump pulse. Figure 2-18 shows the laser spectrum of a mode-locked Ti:sapphire laser (KM-Lab, MTS-a) at a center wavelength of 800-820 nm with a pulse duration of 40 fs and a repetition rate of 86 MHz.

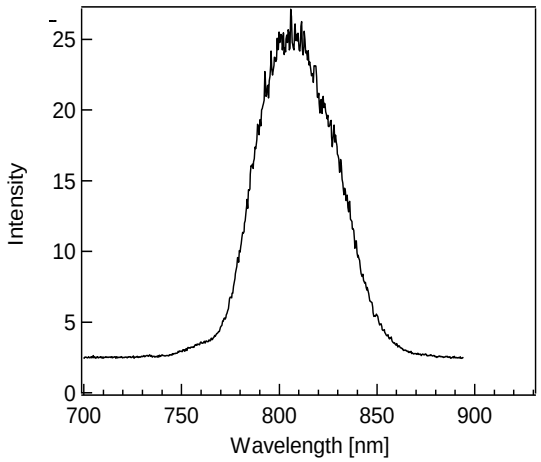

Fig. 2-18 Ti:sapphire laser spectrum at a center wavelength of 810 nm with a pulse duration of 40 fs.

2.3.1 Isotropic configuration

Figure 2-19 shows the schematic of the experimental setup. The optical pulses were split with a partial beam splitter into pump and probe pulses with 9:1 ratio, and their fluencies of 16.0 μJ/cm^2 and < 0.08 μJ/cm^2, respectively[23-25]. The power of probe pulse is much smaller than that of pump pulse not to induce any modulation on the sample. The linearly polarized pump and probe pulses were focused with a single convex lends to be overlapped on the sample at a diameter of approximately 40 μm.

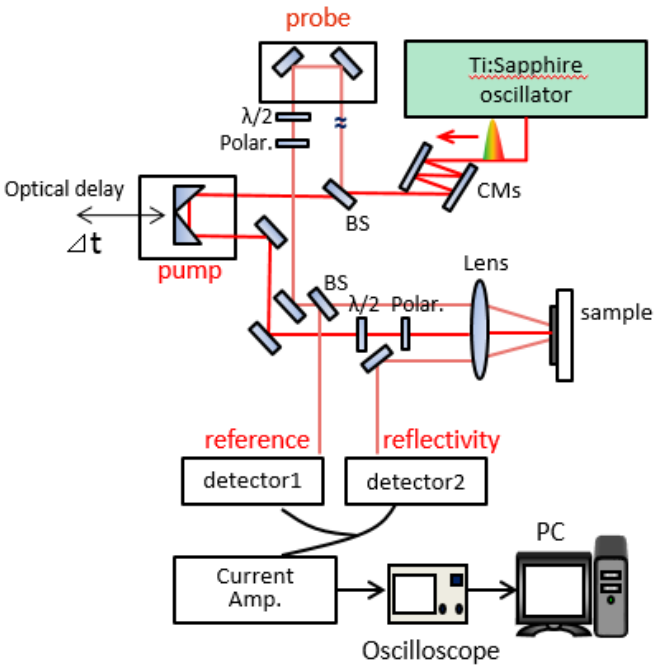

Fig. 2-19 Setup for pump-probe spectroscopy (Isotropic configuration). CMs, chirped mirrors; BS, beam splitter; Polar., polarizer; Amp., current preamplifier.

The transient reflectivity change of the probe pulse was monitored with a pair of balanced PIN photodiodes (Hamamatsu Photonics, S5973-01). The differential signal from the photodiodes was amplified with a current preamplifier (SRS, SR570) and obtained by accumulating 4000 scans of the digital oscilloscope (Iwatsu DS-4354 M). A delay between the pump and probe pulses is controlled by changing the optical path lengths. The time-zero was arranged with using a cross correlation between pump and probe pulses. The 300 μm difference between the pump and probe pulse lengths corresponds to 1-ps time delay. The time-resolution in pump-probe spectroscopy is dependent on the pulse width, and the time step is determined by the mechanical pitch of optical delay stage. Temporal evolution of the reflectivity was measured by scanning the delay between the pump and probe pulses repetitively at 20 Hz with a fast-scan mechanical stage (APE GmbH ScanDelay). The oscillation components are observed by removing the non-oscillatory components using a band-pass filter of the current amplifier in the range from 1 to 300 kHz. The oscillation by coherent phonons is amplified due to reduce contribution from the slow decay component of the strong

electronic response. The data were averaged from 500 scans. All of the measurements were conducted at room temperature in the air.

2.3.2 EO-sampling configuration

Figure 2-20 shows another technique, called EO-sampling, in which the reflected pulse from the sample was separated into p- and s-polarized components and detected with balanced photodiodes to remove the isotropic components of the reflectivity change.

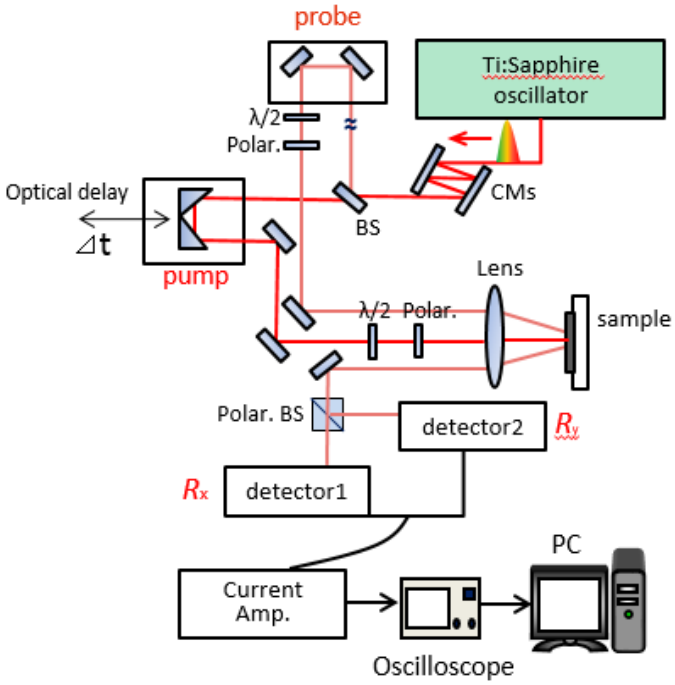

Fig. 2-20 Schematic of EO sampling configuration in a pump-probe spectroscopy.

Figure 2-21 shows a typical transient reflectivity signal of *n*-type GaAs in our study[26]. This result shows mode beating consist of two modes at the frequencies of 8.7 THz and 7.7 THz. These oscillations are identified the longitudinal optical (LO) phonons and the LO phonon-plasmon coupling (LOPC) oscillations[27].

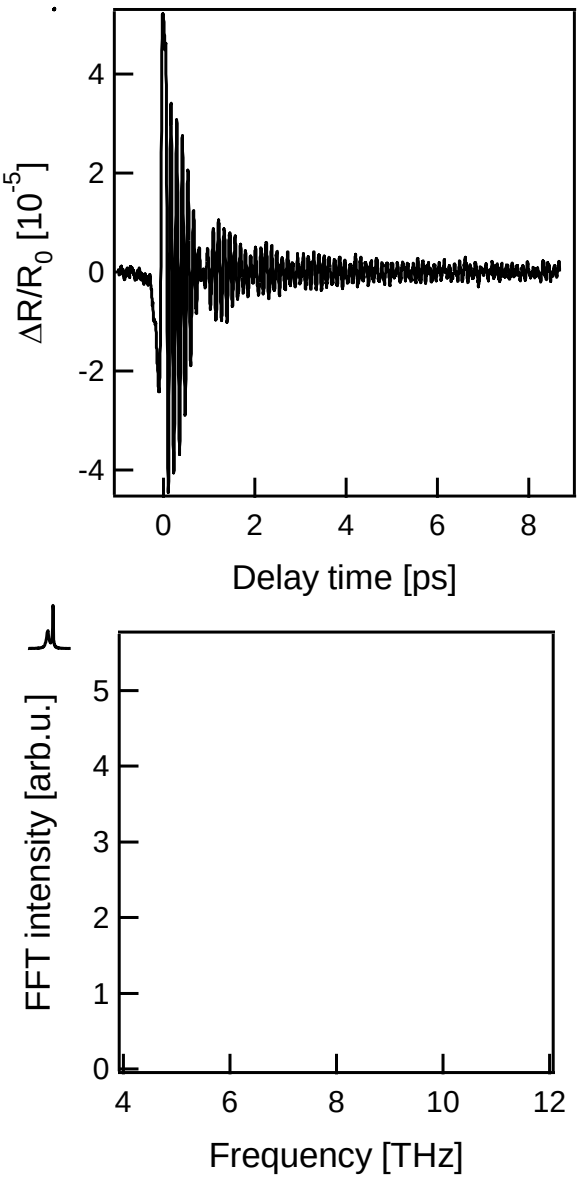

Fig. 2-21 Transient reflectivity change and FFT intensity of *n*-type GaAs.

2.3.3 Optical pump mid-IR probe spectroscopy

The used femtosecond laser system consists of Ti:sapphire oscillator and regenerative amplifier and its operated with a repetition rate of 1 kHz. The output pulse from the regenerative amplifier was divided into two pulses (pump and probe pulses) by the beam splitter. The pump pulse was chopped by using the optical chopper operating at 500 Hz. The probe pulse was converted to mid IR pulse by using the optical

parametric amplification (OPA) and differential frequency generation (DFG). The pulse width of the mid-IR probe pulse was 120 fs. The reflected light from the sample was detected using a spectrometer and a photoconductive detector. The time-resolved mid-IR reflectivity measurements were performed at Onda laboratory of Tokyo Institute of Technology.

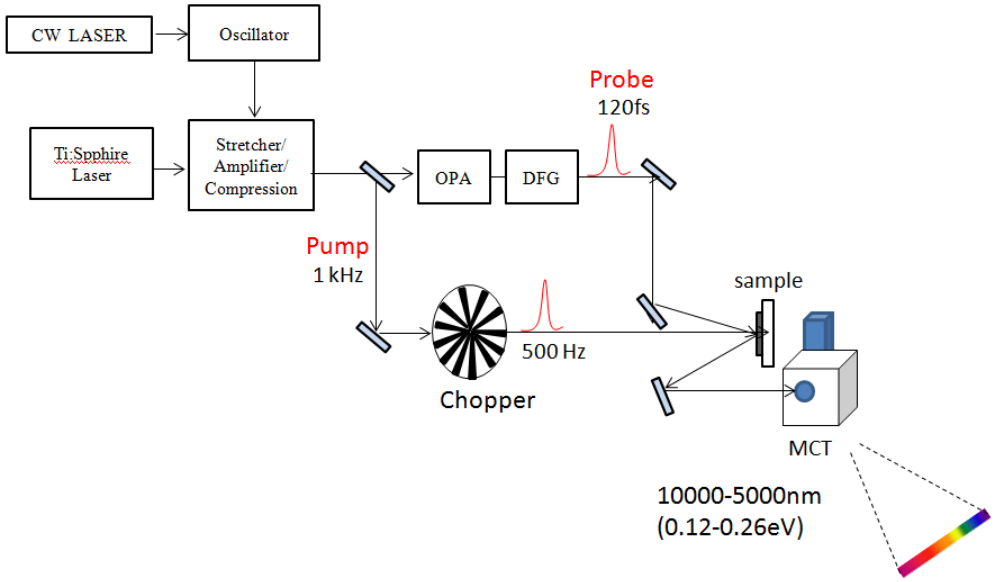

Fig. 2-22 Setup for optical pump and mid-IR probe spectroscopy. (MCT photoconductive detector)

References

1. W. Richter, A. Krost, U. Nowak, and E. Anastassakis, "Anisotropy and dispersion of coupled Plasmon-LO-phonon modes in Sb_2Te_3", *Z. Phys. B – Condensed Matter*, **49**, 191 (1982).
2. L. –L. Wang, and D. D. Johnson, "Ternary Tetradymite compounds as topological insulators", *Phys. Rev. B*, **83**, 241309 (2011).
3. W. Zhang, R. Yu, H. –J. Zhang, Z. Dai, and Z. Fang, "First-principle studies of the three-dimensional strong topological insulators Bi_2Te_3, Bi_2Se_3, and Sb_2Te_3", *New J. Phys.*, **12**, 065013 (2010).
4. Y. L. Chen, J. –H. Chu, J. G. Analytis, Z. K. Liu, K. Igarashi, H. –H. Kuo, X. L. Qi, S. K. Mo, R. G. Moore, D. H. Lu, M. Hashimoto, T. Sasagawa, S. C. Zhang, I. R. Fisher, Z. Hussain, and Z. X. Shen, "Massive Dirac Fermion on the surface of a magnetically doped topological insulator", *Science*, **329**, 659 (2010).
5. M. Hada, K. Norimatsu, S. Tanaka, S. Keskin, T. Tsuruta, K. Igarashi, T. Ishikawa, Y. Kayanuma, R. J. Dwayne Miller, K. Onda, T. Sasagawa, S. Koshihara, and K. G. Nakamura, "Preferential atomic motions in a photoexcited topological insulator Bi_2Te_3", *Phys. Rev. B*, submitted.
6. K. S. Novoselov and A. H. Castro Neto, "Two-dimensional crystals-based heterostructures: materials with tailored properties", *Phys. Scr.*, **T146**, 014006 (2012).
7. M. Kuwahara, R. Endo, K. Tsutsumi, F. Morikasa, T. Tsuruoka, T. Fukaya, M. Suzuki, M. Susa, T. Endo, and T. Tadokoro, "Approach for measuring complex refractive index of molten Sb_2Te_3 by spectroscopic ellipsometry", *Appl. Phys. Lett.*, **100**, 101910 (2012).
8. I. Katayama, S. Koga, K. Shudo, J. Takeda, T. Shimada, A. Kubo, S. Hishita, D. Fujita, and M. Kitajima, "Ultrafast dynamics of surface-enhanced Raman scattering due to Au nanostructures", *Nano Lett.*, **11**, 2648 (2011).

9. L. Sun, Z. Lin, J. Peng, J. Weng, Y. Huang, and Z. Luo, “Preparation of few-layer bismuth selenide by liquid-phase-exfoliation and its optical absorption properties”, *Sci. Rep*., **4**, 4794 (2014).
10. Hall resistivity measurement was performed with help of M. Namiki of Sasagawa group of Tokyo Tech.
11. C. W. Luo, H. J. Wang, S. A. Ku, H. –J. Chen, T. T. Yeh, J. –Y. Lin, K. H. Wu, J. Y. Juang, B. L. Young, T. Kobayashi, C. –M. Cheng, C. –H. Chen, K. –D. Tsuei, R. Sankar, F. C. Chou, K. A. Kokh, O. E. Tereshchenko, E. V. Chulkov, Yu. M. Andreev, and G. D. Gu, “Snapshots of Dirac Fermions near the Dirac point in topological insualtors”, *Nano Lett*., **13**, 5797 (2013).
12. S. Yamamoto, Mater thesis of Sasagawa group of Tokyo Tech.,(2013).
13. Transmission spectrum measurement of Sb_2Te_3 was performed with help of R. Yano of Sasagawa group of Tokyo Tech.
14. Transmission spectrum measurement of Bi_2Te_3 was performed with help of Prof. T. Ishikawa of Department of Chemistry and Materials Science of Tokyo Tech.
15. P. Di. Pietro, F. M. Vitucci, D. Nicoletti, L. Baldassarre, P. Calvani, R. Cava, Y. S. Hor, U. Schade, and S. Lupi, “Optical conductivity of bismuth-based topological insulators”, *Phys. Rev. B*, **86**, 045439 (2012).
16. H. Cui, I. B. Bhat, and R. Venkatasubramanian, “Optical constants of Bi2Te3 and SB2Te3 measured using spectroscopic ellipsometry”, *J. Electr. Mater.*, **28**, 111 (1999).
17. Raman spectroscopy was performed with help of H. Taniguchi of Nagoya University.
18. G. C. Sosso, S. Caravati, and M. Bernasconi, “Vibrational properties of crystalline Sb_2Te_3 from first principles”, *J. Phys.: Condens. Matter*, **21**, 095410 (2009).
19. W. Richter, H. Köhler, and C. R. Becker, “A Raman and far-infrared investigation of phonons in the rhombohedral V_2-VI_3 compounds”, *Phys. Stat. Sol. (b)*, **84**, 619 (1977).
20. V. Chis, I. Yu. Sklyadneva, K. A. Kokh, E. V. Chulkov, “Vibrations in binary and ternary topological insulators: First-pronciples calculations and Raman spectroscopy measurements”, *Phys. Rev. B*, **86**, 174304 (2012).
21. T. Mindl, P. Hefferle, S. Schneider, and F. Dörr, “Characterization of a train of subpicosecond laser pulses by Fringe Resolved Autocorrelation Measurements”, *Appl. Phys. B*, **31**, 201 (1983).

22. Swamp Optics, LLC. HP, http://www.swampoptics.com
23. K. G. Nakamura, J. Hu, K. Norimatsu, A. Goto, K. Igarashi, and T. Sasagawa, "Observation of coherent higher frequency A_{1g}^2 phonon in Bi_2Se_3 using femtosecond time-resolved reflection measurement", *Solid State Commun.*, **152** (2012) 902.
24. K. Norimatsu, J. Hu, A. Goto, K. Igarashi, T. Sasagawa, and K. G. Nakamura, "Coherent optical phonons in a Bi_2Se_3 single crystal measured via transient anisotropic reflectivity", *Solid State Commun.*, **157** (2013) 58.
25. K. Norimatsu, M. Hada, S. Yamamoto, T. Sasagawa, M. Kitajima, Y. Kayanuma, and K. G. Nakamura, "Dynamics of all the Raman-active coherent phonons in Sb_2Te_3 revealed via transient reflectivity", *J. Appl. Phys.*, **117** (2015) 143102.
26. S. Hayashi, K. Kato, K. Norimatsu, M. Hada, Y. Kayanuma, and K. G. Nakamura, "Measuring quantum coherence in bulk solids using dual phase-locked optical pulses", *Scientific reports*, **4** (2014) 4456.
27. J. Hu, O. V. Misochko, A. Goto, and K. G. Nakamura, "Delayed formation of coherent LO phonon-plasmon coupled modes in n- and p-type GaAs measured using a femtosecond coherent control technique", *Phys. Rev. B*, **86**, 235145 (2012).

Chapter 3.
Phonon dynamics

3.1 Introduction

Photo-excited dynamics of topological insulators have been studied by using ARPES, STM and STS. However, there is little known about their phonon vibration dynamics. Investigating these dynamics in topological insulators would be closely related with intrinsic features for electronic applications through a perspective of electron-phonon interaction. The optical phonon modes of topological insulators at the Γ point consist of $2(A_{1g}+E_g) + 3(E_u+A_{2u})$, where A_{1g} and E_g modes are Raman active modes. The incoherent phonon properties of bismuth and antimony compounds (Bi_2Te_3, Bi_2Se_3 and Sb_2Te_3) have been extensively investigated with Raman scattering and first principle calculations[1-6]. Recently, coherent optical phonons have been measured in Bi_2Te_3, Bi_2Se_3 and Sb_2Te_3[7-11].The A_{1g}^1 mode in Bi_2Te_3 has been observed at the frequencies of 1.8 THz using a 100 fs pulse laser[7]. Y. Wang *et al*. reported two coherent phonon modes (A_{1g}^1 and A_{1g}^2) in Bi_2Te_3 and Sb_2Te_3 crystals by using 50 fs pulse laser[8]. The frequency of A_{1g}^2 mode in Bi_2Te_3 is 4.0 THz. In the Sb_2Te_3 crystal, the A_{1g}^1 and A_{1g}^2 modes have been reported 2.1 THz and 5.0 THz. Only the A_{1g}^1 mode in Bi_2Se_3 have been observed at around 2.1 THz by using 150 fs or 200 fs pulse laser[10,11]. However, the decaytime of three modes (E_g^1, E_g^2 and A_{1g}^2) have not yet been reported in time-domain-spectroscopy, and to the best of our knowledge, the anisotropic modes (E_g^1 and E_g^2) have not been observed. In this chapter, I studied ultrafast dynamics of coherent phonons in the topological insulators (Sb_2Te_3, Bi_2Te_3, and Bi_2Se_3) by using femtosecond time-resolved near-infrared (IR) reflectivity measurements.

3.2 Bismuth Selenide (Bi_2Se_3)

3.2.1 Coherent *A*-symmetric optical phonons

The coherent *A*-symmetry optical phonons (A_{1g}^1, A_{1g}^2 modes) are usually obtained with isotropic configuration. Figure 3-1 shows the temporal evolution of the transient reflectivity change. The delay zero (Δt_1=0) was determined by measuring cross correlation with second-harmonic generation, as previously indicated (as previously mentioned in chapter 2). The obtained reflectivity change consists of two components: one is an oscillatory part caused by the coherent phonons, and the other is a non-oscillatory background component arising from electrons photo-excited to higher energy bands, carrier recombination, lattice heating, etc. Therefore, to remove the non-oscillatory background modulation, I use a band-pass filter to clearly observe the oscillatory part derived from coherent phonons in this experiment. The successive beat signals derive from the motion of coherent phonons. The fast-Fourier transformed (FFT) spectrum of the transient reflectivity in the range of 0.15–7.0 ps shows two distinct peaks at frequencies of 2.1 and 5.1 THz. In comparison with Raman spectroscopy, they are assigned to the out-of-plane A_{1g}^1 and A_{1g}^2 optical phonons, respectively[1,5]. The oscillation components induced by coherent phonons can be expressed as a sum of damped oscillations:

$$\Delta R(t)/R_0 = A_0 + \sum_{i=1}^{N} A_i \exp(-t/\Gamma_i)\sin(2\pi T_i t + \delta_i) \quad (3.1)$$

where A_i, Γ_i, T_i, and δ_i are the amplitude, decaytime, frequency, and initial phase of *i*th-vibration modes, respectively. A_0 is the baseline and N is a number of phonon modes.

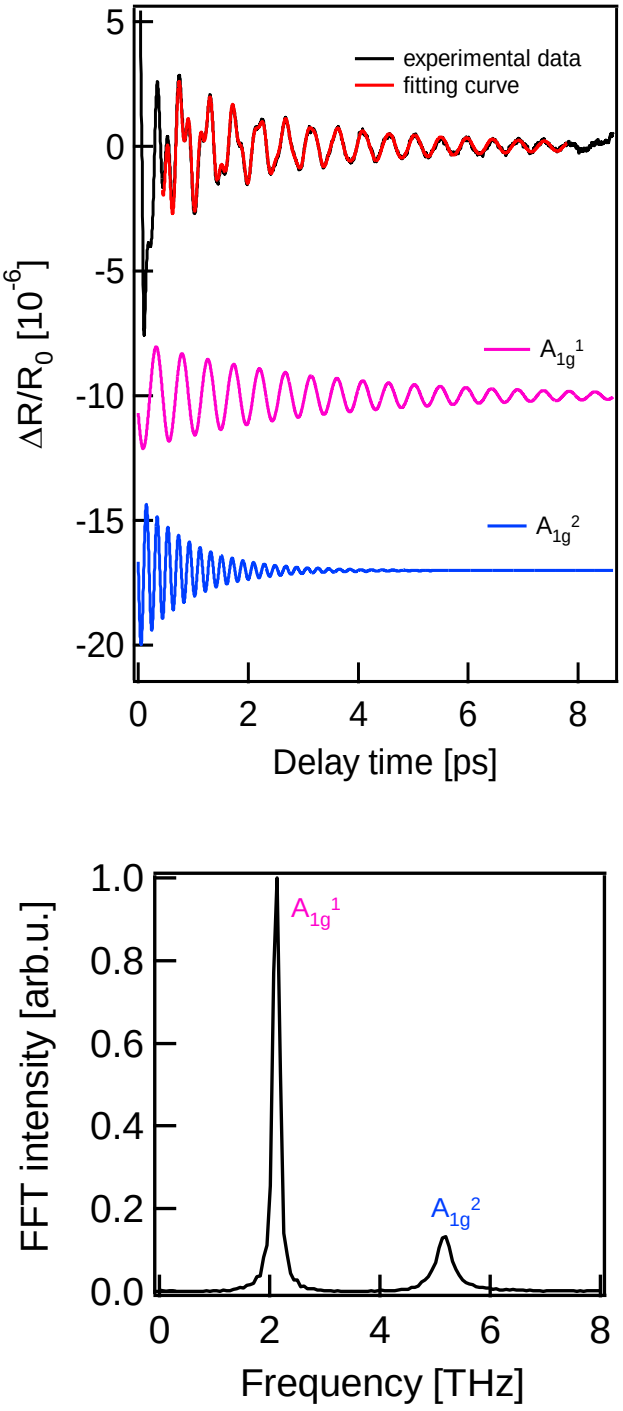

Fig. 3-1 Transient reflectivity change ($\Delta R/R_0$) and FFT spectrum in Bi_2Se_3: the experimental data (black line) and the result of fitting with two damped oscillations (red line) expressed by Eq. (3.1). Oscillations of A_{1g}^1 and A_{1g}^2 phonon modes with using fitting parameters are also shown by pink and blue curves, respectively.

By fitting the transient reflectivity with Eq. (3.1), the decaytimes of A_{1g}^{1} and A_{1g}^{2} coherent phonons were obtained as 3.2 ps and 0.9 ps, respectively. The decaytime of the A_{1g}^{1} mode agrees with the value reported in a previous study[11]. N. Kumar *et al.* have been observed the A_{1g}^{1} mode in Bi_2Se_3 by using 250 fs pulse laser, they reported the frequency of the A_{1g}^{1} mode is 2.167 THz with the decaytime of 3.2 ± 0.1 ps. The coherent A_{1g}^{2} phonons decayed faster than the A_{1g}^{1} phonons. In case of Bi_2Se_3, the signal of coherent phonons has disappeared when increasing the laser fluence or the irradiation time, thus this material is not appropriate for long time experiment.

3.2.2 Coherent anisotropic optical phonons

The anisotropic *E*-symmetry coherent phonons are usually obtained with EO-sampling (as previously mentioned in chapter 2). Figure 3-2 shows the transient reflectivity change of Bi_2Se_3 by using EO-sampling. Fine tuning of the pump pulse polarization enables the observation of E_g^{1} and E_g^{2} modes. The oscillations at frequencies of 1.3 THz, 2.1 THz, 3.8 THz, and 5.3 THz were assigned to the E_g^{1}, A_{1g}^{1}, E_g^{2}, and A_{1g}^{2} modes respectively [1,4,5]. By fitting the transient reflectivity using Eq. (3.1), the decaytimes of the E_g^{1} and E_g^{2} phonons were obtained as $\ll 1$ ps and 1.0 ps, respectively.

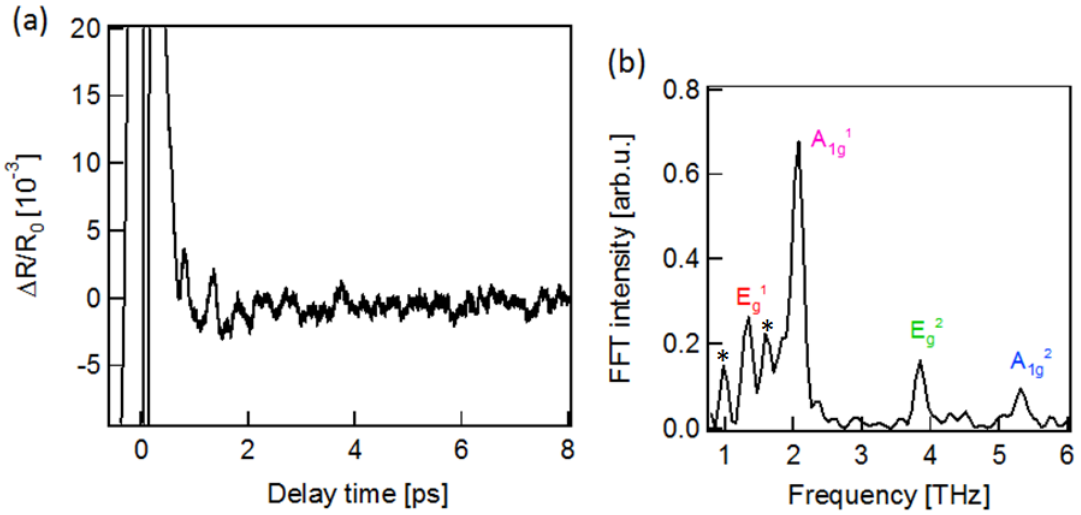

Fig. 3-2 (a) Coherent phonon detection of Bi_2Se_3 by using the EO-sampling. (b) The FFT spectrum of the anisotropic reflectivity change. The peak at the frequency of 1.3 THz, 2.1 THz, 3.8 THz, and 5.3 THz were assigned to the E_g^{1}, A_{1g}^{1}, E_g^{2}, and A_{1g}^{2}, respectively. The peaks marked with asterisks (*) may be because of artificial peak.

3.3 Bismuth telluride (Bi_2Te_3)

3.3.1 Coherent *A*-symmetric optical phonons

The oscillatory behaviors of the transient reflectivity as a function of the time delay between the pump and probe pulses in Bi_2Te_3 shown in Fig. 3-3. The FFT intensity of this oscillation component shows two peaks at 1.8 THz and 4.0 THz, which were assigned A_{1g}^1 and A_{1g}^2 modes, respectively[1,3,5,6]. The oscillatory part of the transient reflectivity change was analyzed with two damped oscillations using by Eq. (3.1). The decaytimes of A_{1g}^1 and A_{1g}^2 modes were obtained as 4.1 ps and 1.1 ps, respectively. The decaytime of the A_{1g}^1 mode agrees with the value reported in a previous study[7]. A. Q. Wu *et al.* have been observed the A_{1g}^1 mode in Bi_2Te_3 by using 100 fs pulse laser, they reported the frequency of the A_{1g}^1 mode is 1.84 THz with the decaytime of 5.0 ps.

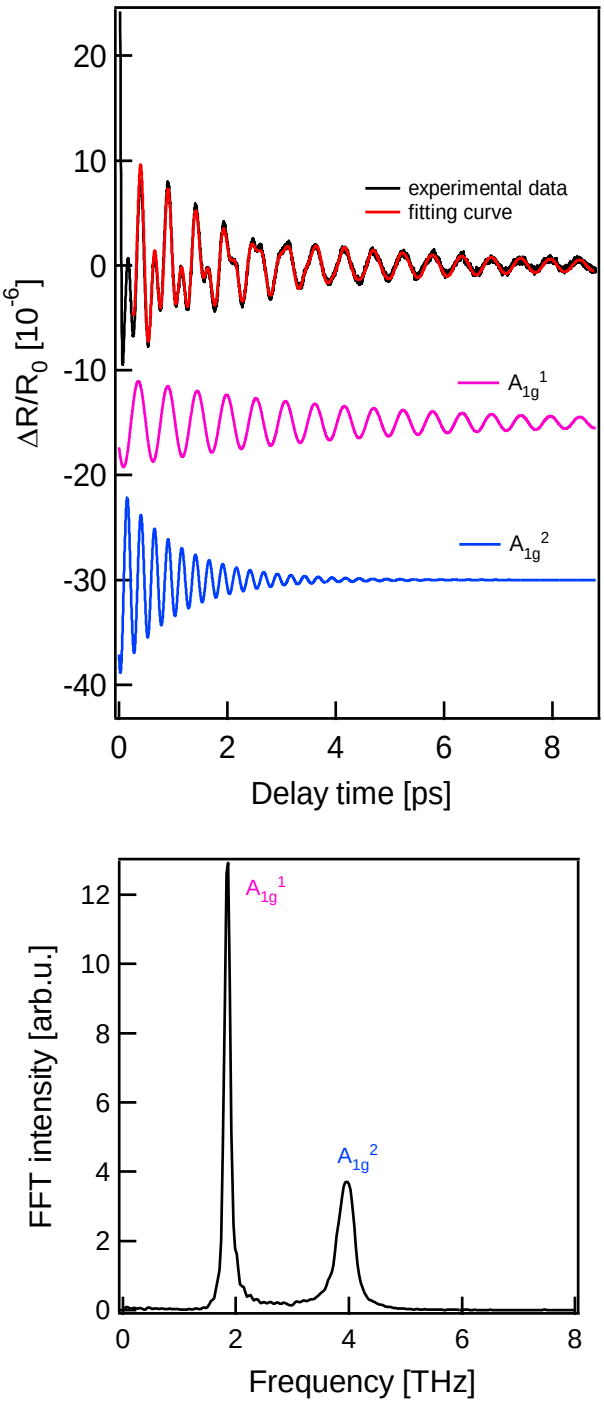

Fig. 3-3 Transient reflectivity change ($\Delta R/R_0$) and FFT spectrum in Bi_2Te_3: the experimental data (black line) and fitting curve (red line) with two damped oscillations (red line) expressed by Eq. (3.1). Oscillations of $A_{1g}{}^1$ and $A_{1g}{}^2$ phonon modes with using fitting parameters are also shown by pink and blue curves, respectively.

3.3.2 Coherent anisotropic optical phonons

Figure 3-4 shows the transient reflectivity change of Bi_2Te_3 by using EO-sampling. These oscillations at frequencies of 1.3 THz, 2.1 THz, 3.3 THz, and 5.0 THz were assigned to the E_g^1, A_{1g}^1, E_g^2, and A_{1g}^2 modes, respectively[1,3,5,6]. The obtained decaytimes of the E_g^1 and E_g^2 phonons are ≪1 ps and 2.9 ps, respectively. The decaytime of E_g^2 mode is three times longer than that of Bi_2Se_3.

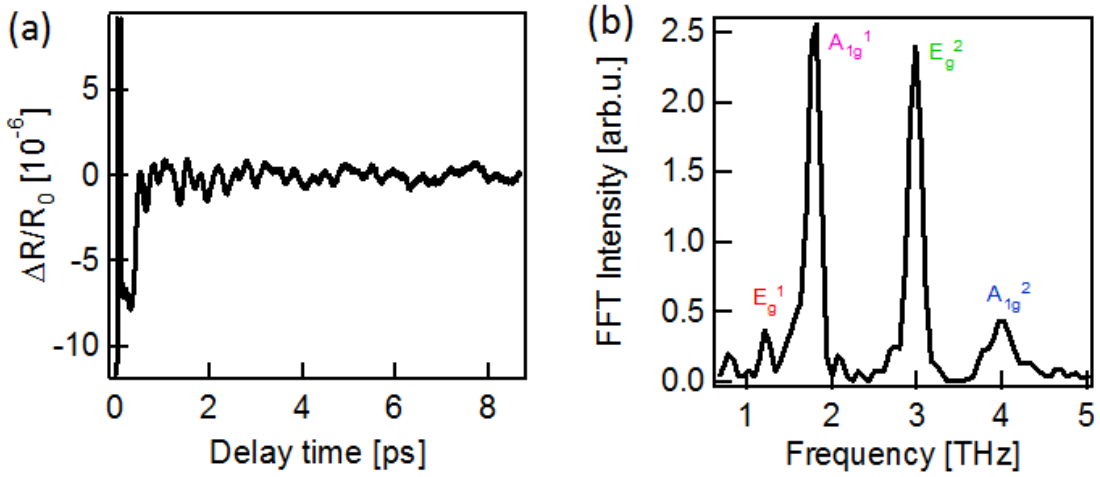

Fig. 3-4 (a) Coherent phonon detection of Bi_2Te_3 by using the EO-sampling. (b) The FFT spectrum of the anisotropic reflectivity change. The peak at the frequency of 1.2 THz, 1.8 THz, 3.0 THz, and 4.0 THz were assigned to the E_g^1, A_{1g}^1, E_g^2, and A_{1g}^2, respectively.

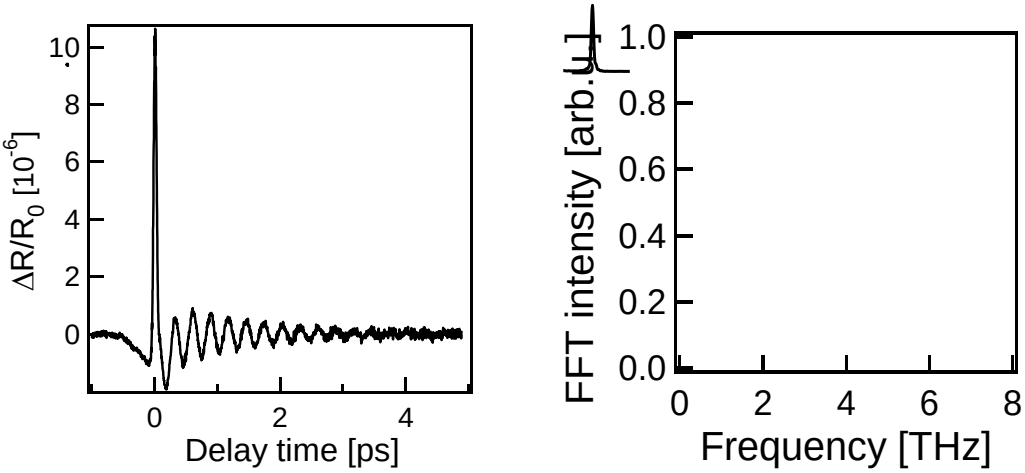

Fig. 3-5 Transient reflectivity obtained by using the EO-sampling with long-time laser irradiation. The oscillation at the frequency of 3.5 THz is the A_{1g} phonons of tellurium due to the tellurium segregation.

Here, it is worth noting that tellurium segregation is induced by accumulative heat when increasing the laser fluency or the irradiation time. Figure 3-5 shows the transient reflectivity changes when I irradiate the laser pulse (>30 min) and 30 μJ/cm^2. The oscillation at the frequency of 3.5 THz have been observed, and which agrees with the A_{1g} phonons of tellurium[12] as a result of laser-induced decomposition of the Bi_2Te_3. Similar thermal segregation of tellurium has been reported for other tellurium compounds such as CdTe[13] and $Ge_2Sb_2Te_5$[14]. To avoid such heating effects, the set pump-pulse intensity is 16.0 μJ/cm^2, repetition rate of 86 MHz, and a data-accumulation time of 400 s that was less than the lower limit of thermal tellurium segregation.

3.4 Antimony telluride (Sb_2Te_3)

3.4.1 Coherent *A*-symmetric optical phonons

The transient reflectivity changes as a function of the time delays between the pump and probe pulses in Sb_2Te_3 shown in Fig. 3-6. The FFT intensity of this oscillation component shows two peaks at 2.0THz and 5.0 THz, which were assigned $A_{1g}{}^1$ and $A_{1g}{}^2$ modes[1,2,5]. The oscillatory part of the transient reflectivity change was analyzed with two damped oscillations using by Eq. (3.1), the decaytimes of $A_{1g}{}^1$ and $A_{1g}{}^2$ coherent phonons were obtained as 2.4 ps and 1.3 ps, respectively.

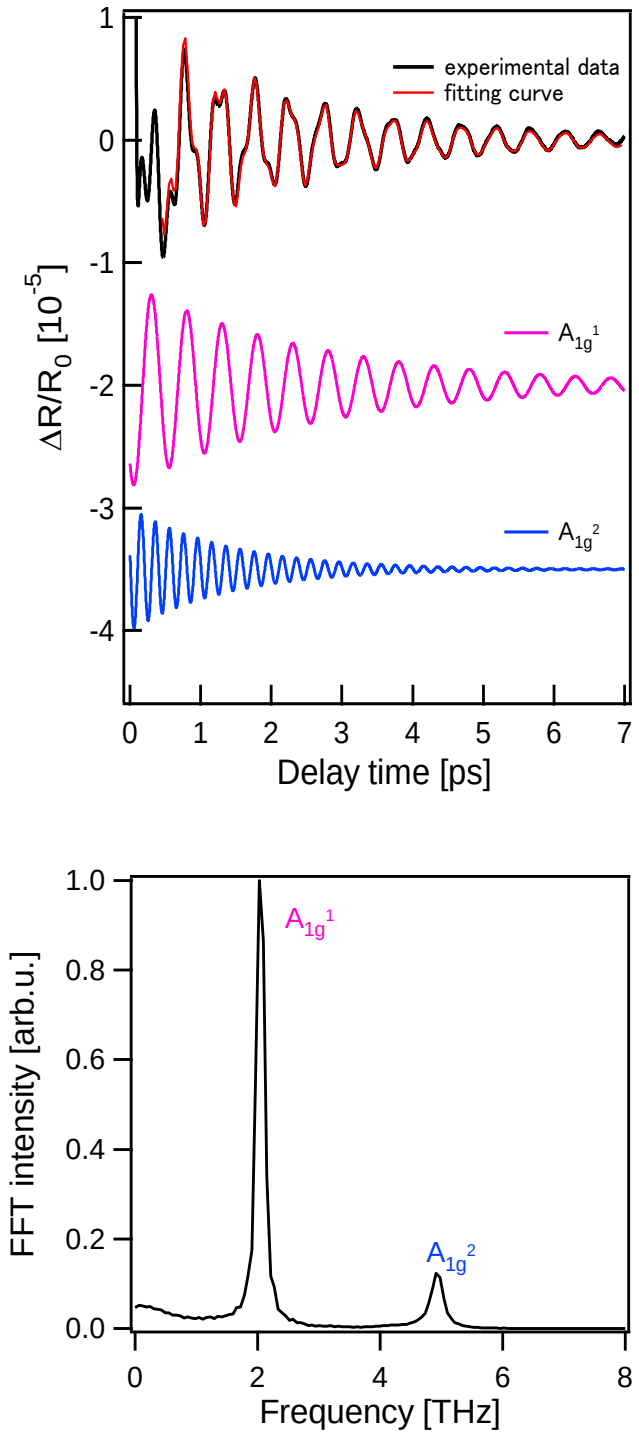

Fig. 3-6 Transient reflectivity change ($\Delta R/R_0$) in Sb_2Te_3 and FFT spectrum: the experimental data (black line) and fitting curve (red line) with two damped oscillations expressed by Eq. (3.1). Oscillations of A_{1g}^1 and A_{1g}^2 phonon modes with using fitting parameters are also shown by pink and blue curves, respectively.

3.4.2 Coherent anisotropic optical phonons

Antimony telluride (Sb_2Te_3) is the most suitable sample among these three chalcogenide compounds (Bi_2Te_3, Bi_2Se_3 and Sb_2Te_3) for investigating more detailed dynamics of coherent phonons, because of laser heating properties. Figure 3-7 shows a schematic view of the polarization angles of the pump and probe pulses over the sample orientation. The pump and probe pulses were directed to the sample nearly perpendicular to the sample (0001) plane. The polarization angle of the probe pulse was fixed to $\pi/4$ from $\vartheta=0$ angle while that of the pump pulse set to $\vartheta=0$ (clockwise direction). This angle is parallel to the $<01\bar{1}0>$ axis of the sample.

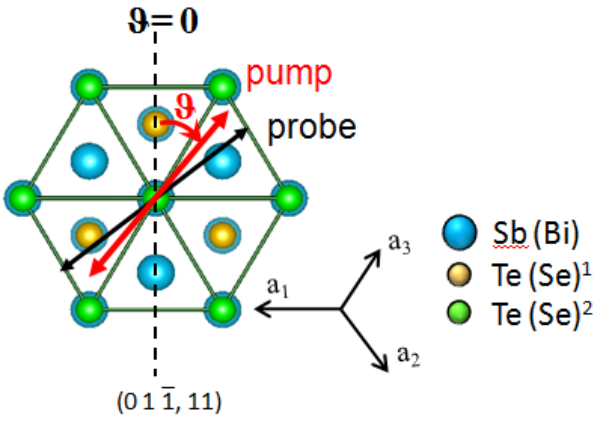

Fig. 3-7 Schematic view of the polarized pump and probe pulses over the crystal orientation.

The reflectivity changes ($\Delta R/R_0$) are dependent on the sample orientation with respect to the polarization angles of the pump pulse. Figures 5(a)–(c) show the transient reflectivity at the pump pulse polarization angles of $\vartheta=\pi/6$, $\pi/3$, and $8\pi/9$, and each FFT spectra are shown in Fig. 3-8(e)–(g). The results show that all of the Raman-active phonons including the E_g^1 phonons have been observed. The frequencies of the in-plane E_g^1 and E_g^2 phonons were 1.2 and 3.3 THz, respectively[1,2,5]. Especially, the E_g^1 phonons at the frequency of 1.2 THz have never by other group.

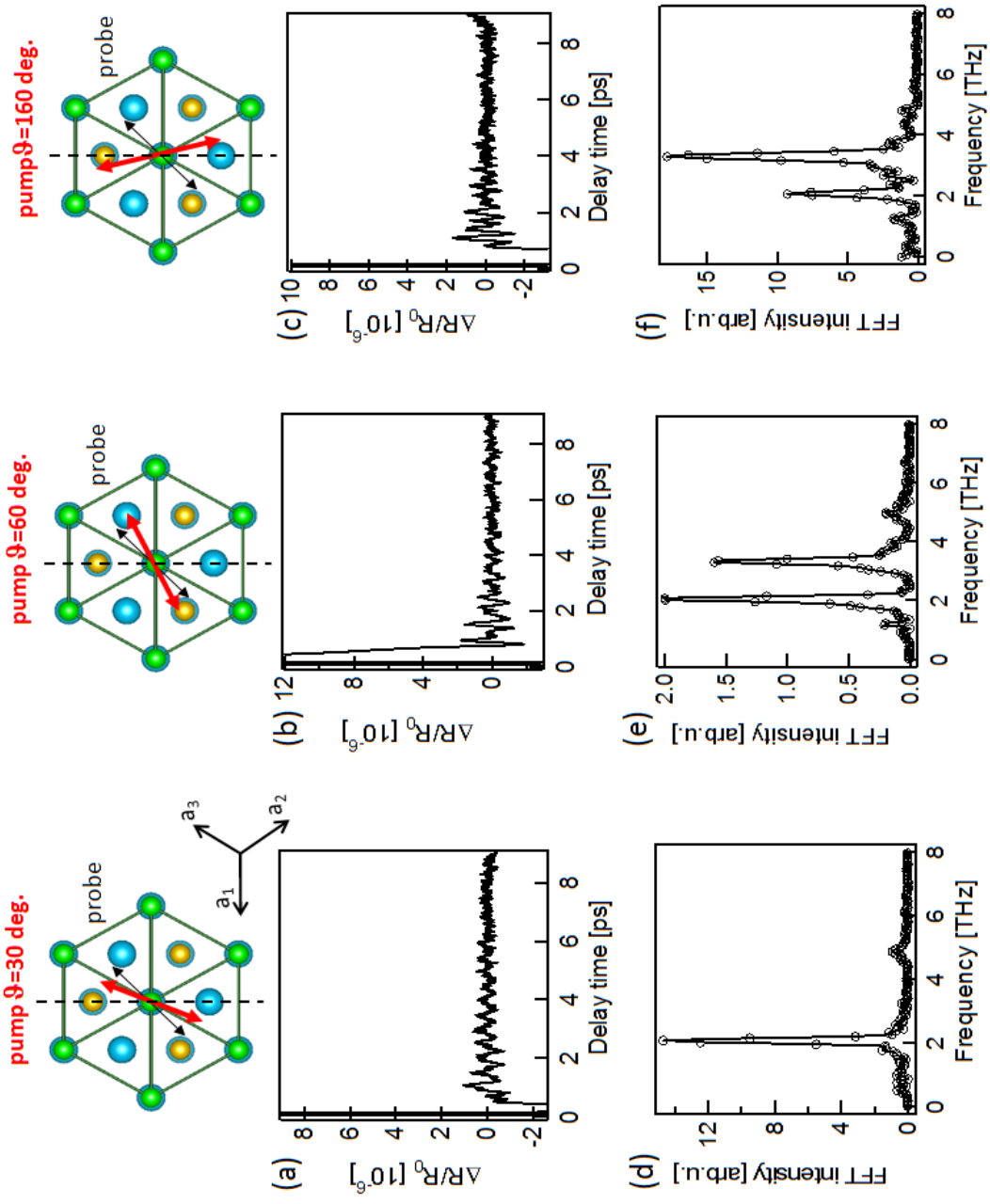

Fig. 3-8 Transient reflectivity changes ($\Delta R/R_0$) in Sb_2Te_3 obtained using EO-sampling. The top of them are the schematic view of the polarization angles of the pump and probe pulses. The spectra of $\Delta R/R_0$ in the pump pulse polarization angle of (a) ϑ=30 deg. (π/6), (b) ϑ=60 deg. (π/3) and (c) ϑ=160 deg. (8π/9), and the FFT spectra of their oscillatory components shown in (d), (e), and (f), respectively.

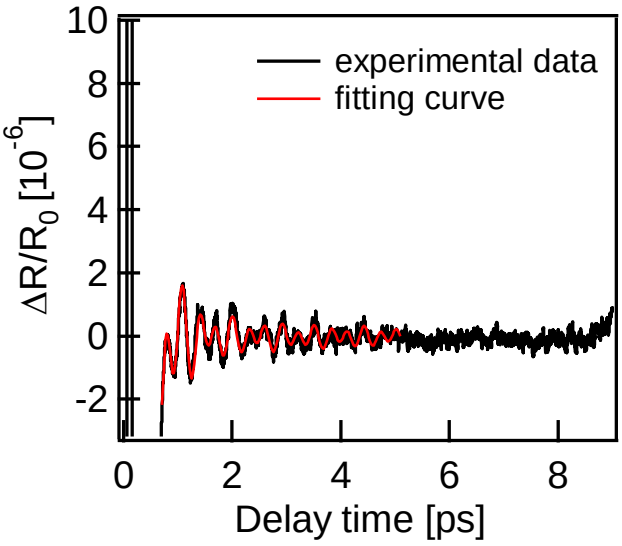

Fig. 3-9 Transient reflectivity change in Sb_2Te_3 with the pump pulse polarization angle of ϑ=160 deg (8π/9). The red line is fitted to the experimental data with using three damped oscillations (E_g^1, A_{1g}^1 and E_g^2).

By fitting the reflectivity signal of ϑ=160 deg (8π/9), the decaytimes of the E_g^1 and E_g^2 phonons are obtained as $\ll$1 ps and 1.4 ps, respectively (Fig. 3-9). The polarization dependence of the phonon amplitude (Fig. 3-10, 3-11) indicates that the A_{1g} and E_g phonons have different polarization dependence. The in-plane E_g^1 and E_g^2 phonons have rotational symmetries through π/2. In contrast, the out-of-plane A_{1g}^1 and A_{1g}^2 phonons have rotational symmetries through π. The out-of-plane A_{1g} phonons are generally not detected with EO-sampling because of their isotropic vibrational properties($\Delta R = R_x - R_y = 0 : R_x = R_y$). However, they are clearly present in Fig.3-11, because of the slightly oblique incident angle of the pump pulse, which will be described in detail later.

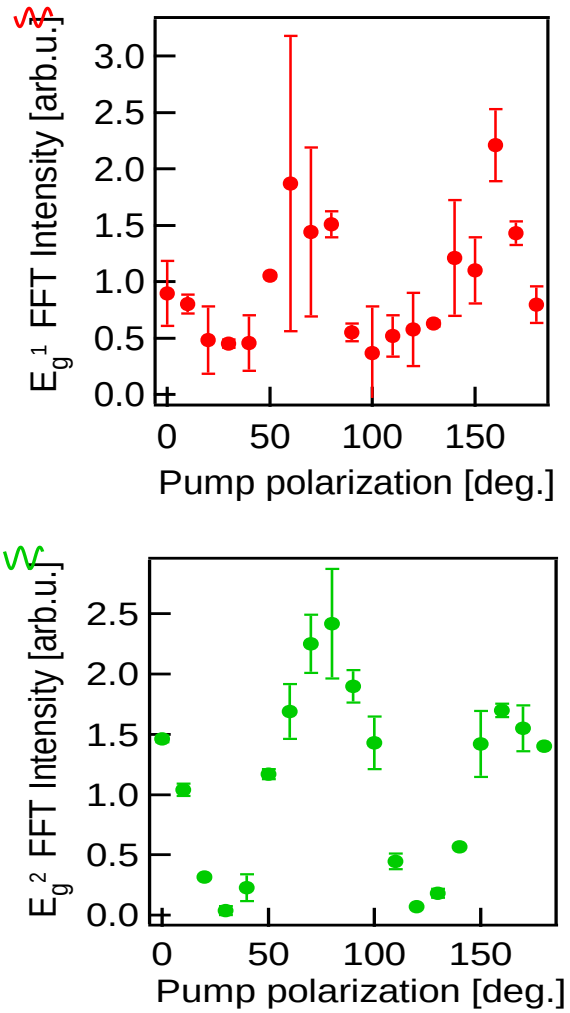

Fig. 3-10 Polarization dependences of the FFT intensity of the E_g^1 and E_g^2 phonons. The solid lines are the fitting curve with Eq. (3.4) and (3.12).

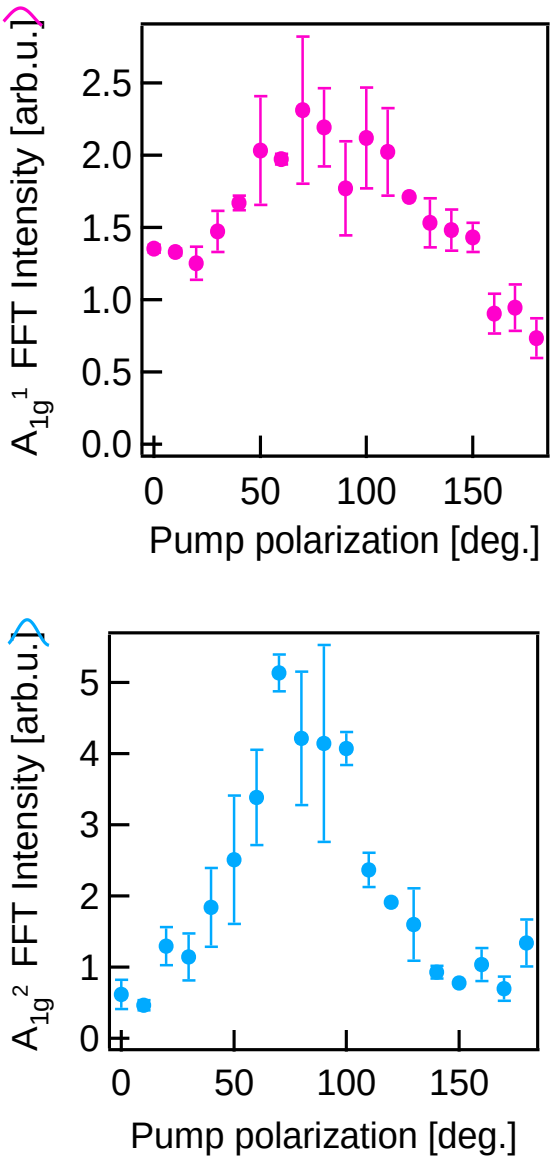

Fig. 3-11 Polarization dependences of the FFT intensity of the A_{1g}^{1} and A_{1g}^{2} phonons. The solid lines are the fitting curve with Eq. (3.4) and (3.12).

3.4.3 Discussion of pump-pulse polarization dependence

The amplitudes of these coherent phonons strongly depend on the pump-pulse polarization. Then, I discuss these results based on the Raman tensor, which represent the interaction between the incident optical electric fields and the polarization of the materials due to lattice deformation and phonon modes. It has the same symmetry as the electron-phonon coupling tensor. The pump pulse induces the coherent phonons and makes the polarization into the materials. Subsequently the probe pulse detects the induced phonons via a change in polarization of the materials. The total process can be separated into two processes: generation and detection. The Raman tensors of rhombohedral structure[15] are expressed as

$$A_{1g} = \begin{pmatrix} a & 0 & 0 \\ 0 & a & 0 \\ 0 & 0 & b \end{pmatrix}$$

$$E_g = \begin{pmatrix} 0 & -c & -d \\ -c & 0 & 0 \\ -d & 0 & b \end{pmatrix} \quad \text{or} \quad \begin{pmatrix} c & 0 & 0 \\ 0 & -c & d \\ 0 & d & 0 \end{pmatrix} \tag{3.2}$$

The intensity of the induced polarization (I) can be described with the Raman tensor ($\hat{\alpha}$) and the incident and outgoing electrical field ($\boldsymbol{e}_{\text{in}}$ and $\boldsymbol{e}_{\text{out}}$) as

$$I = |\boldsymbol{e}_{\text{in}}(\hat{\alpha})\boldsymbol{e}_{\text{out}}|^2 \ . \tag{3.3}$$

The amplitude of the phonons is proportional to the induced polarization in the medium. Thus, the FFT intensity of the E_g phonons (I_{Eg}) is derived from eq. (3-3) as

$$I_{E_g} \propto \left| (\cos\vartheta \quad \sin\vartheta \quad 0)(\hat{\alpha}) \begin{pmatrix} \cos\vartheta \\ \sin\vartheta \\ 0 \end{pmatrix} \right|^2$$

$$= |c(\cos^2\vartheta - \sin^2\vartheta)|^2 = c^2\cos^2(2\vartheta). \tag{3.4}$$

Here, I set $\boldsymbol{e}_{\text{in}} = \boldsymbol{e}_{\text{out}}$ because the present process is the impulsive stimulated process during a single pulse. The polarization of the excitation light component and the Raman light are same. The polarization dependence in E_g-phonon generation is given by $\cos^2(2\vartheta)$. In the detection process, the difference between the *x*- and *y*-components of the reflected pulse due to the induced phonons was observed. The polarization angle of the probe pulse was fixed to $\pi/4$, and the difference of reflection was calculated to be constant as follows:

$$\Delta R = \left(R_{\mathrm{x}} - R_{\mathrm{y}}\right) \tag{3.5}$$

$$R_{\mathrm{x}} = (\cos 45° \quad 0 \quad 0)\begin{pmatrix} c & 0 & 0 \\ 0 & -c & d \\ 0 & d & 0 \end{pmatrix}\begin{pmatrix} \cos 45° \\ 0 \\ 0 \end{pmatrix}$$

$$= \left(\frac{1}{\sqrt{2}} \quad 0 \quad 0\right)\begin{pmatrix} c & 0 & 0 \\ 0 & -c & d \\ 0 & d & 0 \end{pmatrix}\begin{pmatrix} \frac{1}{\sqrt{2}} \\ 0 \\ 0 \end{pmatrix} = \frac{\mathrm{c}}{\sqrt{2}} \tag{3.6}$$

$$R_{\mathrm{y}} = (0 \quad \sin 45° \quad 0)\begin{pmatrix} c & 0 & 0 \\ 0 & -c & d \\ 0 & d & 0 \end{pmatrix}\begin{pmatrix} 0 \\ \sin 45° \\ 0 \end{pmatrix}$$

$$= \left(0 \quad \frac{1}{\sqrt{2}} \quad 0\right)\begin{pmatrix} c & 0 & 0 \\ 0 & -c & d \\ 0 & d & 0 \end{pmatrix}\begin{pmatrix} 0 \\ \frac{1}{\sqrt{2}} \\ 0 \end{pmatrix} = -\frac{\mathrm{c}}{\sqrt{2}} \tag{3.7}$$

$$\Delta R = \left|R_{\mathrm{x}} - R_{\mathrm{y}}\right|^2 = 2\mathrm{c}^2. \tag{3.8}$$

Thus, the difference of the reflection (ΔR) modulated by the pump pulse is proportional to $\cos^2(2\vartheta)$ and the transient reflectivity of the $E_{\mathrm{g}}{}^1$ and $E_{\mathrm{g}}{}^2$ phonons shows rotational symmetry through $\pi/2$, as shown in Fig. 3-10. The observed polarization dependence of the E_{g} phonons and its analysis with the Raman tensor are consistent with a previous report on the polarization dependence of the amplitude of the E_{g} phonons of bismuth crystal, which has the same Raman tensors[16]. Similar to the E_{g} phonons, the FFT intensity of the $A_{1\mathrm{g}}$ phonons ($I_{\mathrm{A_{1g}}}$) is derived from Eq. (3-3) as

$$I_{\mathrm{A_{1g}}} = \left|(\cos\vartheta \quad \sin\vartheta \quad 0)(\hat{\alpha})\begin{pmatrix} \cos\vartheta \\ \sin\vartheta \\ 0 \end{pmatrix}\right|^2$$

$$= (a\cos^2\vartheta + a\sin^2\vartheta)^2 = a^2, \tag{3.9}$$

and the difference of the reflection are

$$R_{\mathrm{x}} = (\cos 45° \quad 0 \quad 0)(\hat{\alpha})\begin{pmatrix} \cos 45° \\ 0 \\ 0 \end{pmatrix} = \frac{a}{2}$$

$$R_{\mathrm{y}} = (0 \quad \sin 45° \quad 0)(\hat{\alpha})\begin{pmatrix} 0 \\ \sin 45° \\ 0 \end{pmatrix} = \frac{a}{2}$$

$$\Delta R = \left|R_{\mathrm{x}} - R_{\mathrm{y}}\right|^2 = 0. \tag{3.10}$$

Despite the isotropic vibrational properties ($R_{\mathrm{x}} = R_{\mathrm{y}}$) because of the incident angle of the probe pulse, the $A_{1\mathrm{g}}$ phonons can be observed with the EO-sampling. According to the

calculated of the FFT intensity (Eq. (3.9)), the polarization angle dependence of the A_{1g} phonons is constant. However, it has rotational symmetry through π as shown in Fig. 3-11. This result may be explained by the slightly oblique incident angle of the pump pulse. Here, I assumed this slightly oblique incident angle to be φ ($\ll 1$) and the incident pump electric field to be

$$\boldsymbol{e}_{\text{in}} = \begin{pmatrix} \cos\vartheta \\ \sin\vartheta \\ \varphi\sin\vartheta \end{pmatrix} \tag{3.11}$$

where I set $\cos\varphi = 1$ and $\sin\varphi = \varphi$. Equation (3-3) leads to the following expression:

$$I'_{A_{1g}} \propto \left| (\cos\vartheta \quad \sin\vartheta \quad \varphi\sin\vartheta)(\hat{\alpha}) \begin{pmatrix} \cos\vartheta \\ \sin\vartheta \\ \varphi\sin\vartheta \end{pmatrix} \right|^2$$
$$= |a + \varphi^2 b\sin^2\vartheta|^2 \approx a^2 + 2\varphi^2 ab\sin^2\vartheta. \tag{3.12}$$

where I'_{A1g} is the intensity of the A_{1g} phonons using the oblique incident pump pulse. Thus, the FFT intensity of the A_{1g} phonons shows polarization dependence of $\varphi^2 ab\sin^2\vartheta$ and a constant offset (a^2). The experimental polarization dependence of the A_{1g} phonons (Fig. 3-11) is well-reproduced.

3.4.4 Coherent control of optical phonons

The coherent *A*-symmetric phonon modes ($A_{1g}{}^1$ and $A_{1g}{}^2$) have been observed with using isotropic configuration as mentioned in 3.3.1, however, the $A_{1g}{}^2$ mode has smaller amplitude and shorter decaytime. I report on the precisely investigation the dynamics of $A_{1g}{}^2$ mode by controlling the amplitude of coherent phonon. Controlling amplitude is performed by double-pulse excitation[17,18]. The pump pulse is lead into a Michelson interferometer to produce double pulses with separation time (Δt'). The separation time (Δt') was varied by moving a mechanical stage in the Michelson interferometer. In the double-pulse experiment, the first pump pulse generates coherent phonons subsequently the second pulse makes the specific phonon mode enhanced or suppressed. By tuning separation time in concord with the period of the vibration

($T_{A_{1g}^1}$ =500 fs and $T_{A_{1g}^2}$ =200 fs), the phonon mode was selectively controlled as shown in Fig. 3-12.

The coherent $A_{1g}{}^2$ phonons decayed faster than the $A_{1g}{}^1$ phonons approximately 2–4 times, which can be said that in common with all compounds. It might be explained that a collision probability of $A_{1g}{}^2$ mode is higher than that of $A_{1g}{}^1$ mode due to high frequency.

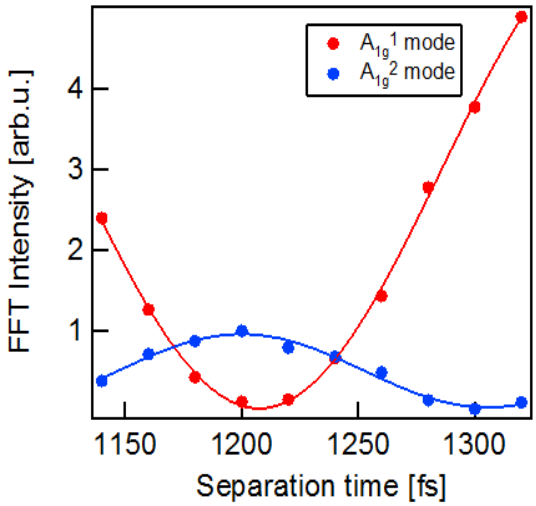

Fig. 3-12 The FFT intensity of the $A_{1g}{}^1$ and $A_{1g}{}^2$ modes by changing the separation time of double-pulses.

Figure 3-13(a) and (b) shows the double pulse reflectivity changes at Δt'=1320 fs and Δt'=1200 fs. As shown in Fig. 3-13(c), it is precisely observed the $A_{1g}{}^2$ phonons at the separation time of 1200 fs. The accurate decay time of the $A_{1g}{}^2$ mode is 1.4 ps analyzed with Eq. (3.1).

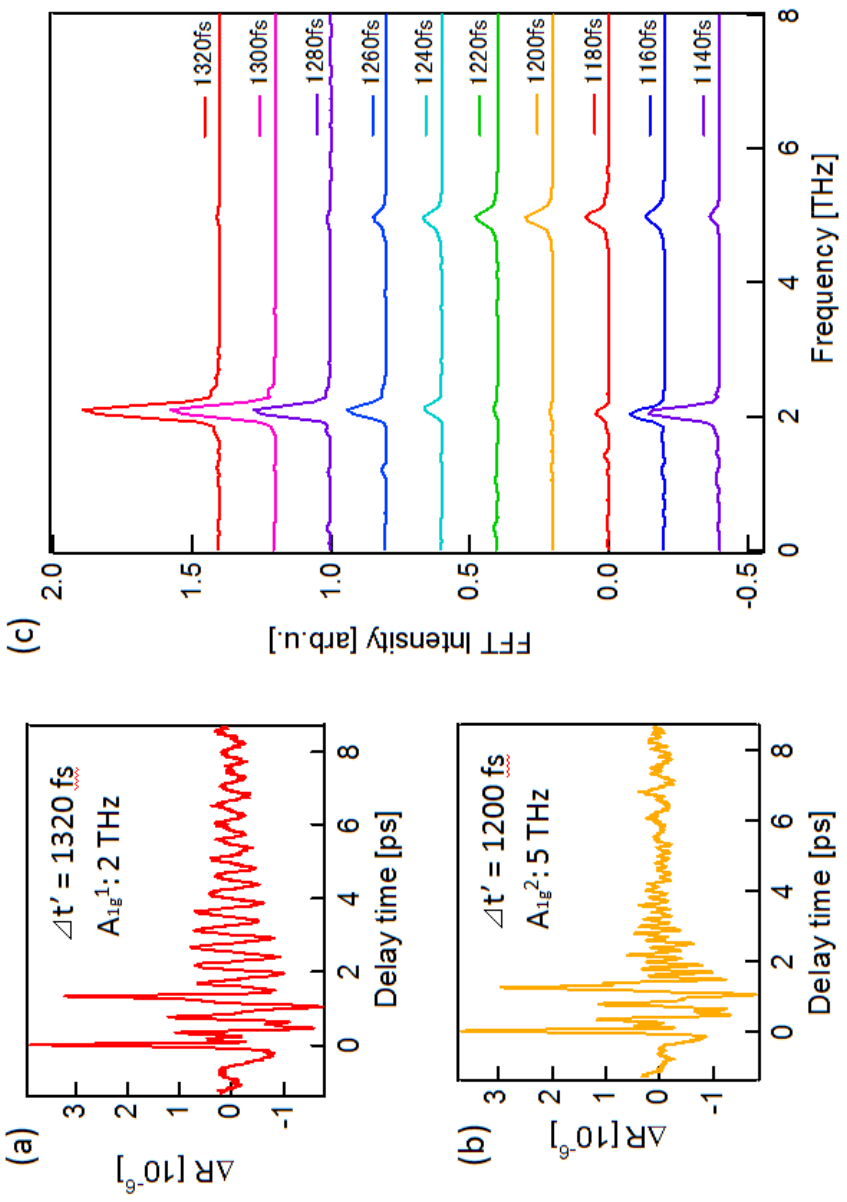

Fig. 3-13 The reflectivity change of Sb_2Te_3 induced by the double pulse excitation: (a) separation time (Δt'=1320 fs) shows only the $A_{1g}{}^1$ mode at the frequency of 2.0 THz, (b) Δt'=1200 fs appears only the $A_{1g}{}^2$ mode at the frequency of 5.0 THz. (c) The FFT intensity with respect to the double pulse separation time from 1140 fs to 1320 fs.

3.5 Thickness dependence

The intrinsic metal-like surface state of topological insulators is expected to be applied in various technical branches. The Raman active optical phonons are often correlated directly to physical properties including electron-phonon coupling. In general, Raman shifts are dependent on size of solids due to variety of physical factor; phonon quantum confinement, surface stress, surface disorder. For example, the red-shift of optical phonons with reducing the solid size in graphite is suggested to be due to the effect of quantum confinement. Besides, the appearance of the D mode arouse from the surface disorder[19]. In transition metal chalcogenide, these shifts are attributed to the variation in the dielectric screening environment for Coulomb interaction as thickness changes[20]. Similarly, investigating between the differences of bulk and surface optical phonons would be important for revealing the properties of the topological insulators. In this experiment, the transient transmission measurements were carried out with using an ultra thin-film. The ultra thin-film is prepared to exfoliate the single crystal sample with an adhesive tape, and the thickness was estimated to be less than 3 nm, which corresponds to < 3 quintuple layers (QLs).

Figure 3-14 shows the temporal evolution of the transient transmission spectrum of Sb_2Te_3 thin-film. This signal is obtained by accumulating 4000 scans and average of 10 times. The FFT spectrum of the transient transmission spectrum in the range of 0.4–4.4 ps is shown in Fig. 3-15. The sharp peak at frequency of 5.2 THz corresponds to the out-of-plane $A_{1g}{}^2$ mode. It is clearly found that the frequency of $A_{1g}{}^2$ mode shifts higher than that of bulk and the $A_{1g}{}^1$ mode disappeared. This trend is also reported by other groups as shown in Table 3-1[5,21-23].

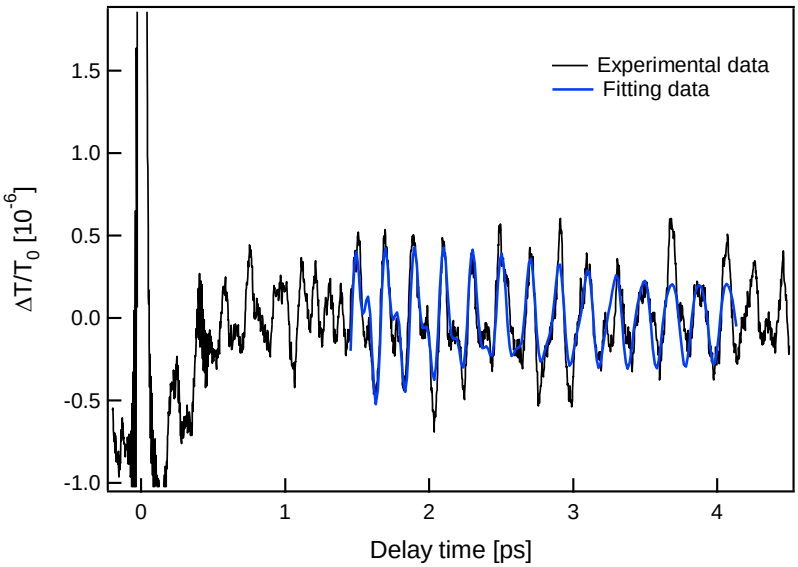

Fig. 3-14 Transient transmission of Sb_2Te_3 ultra thin-film.

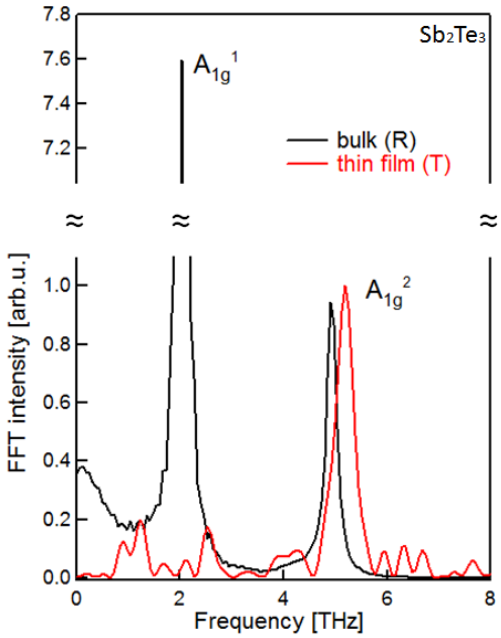

Fig. 3-15 FFT spectrum of the transient transmission signal (red line) and that of bulk.

Table 3-1 Frequency of A_{1g}^2 mode comparison with bulk and thin-film.

Sample	Bulk	Thin-film	Difference	Reference
Sb_2Te_3	5.00	5.20	+0.20	This work
Sb_2Te_3	5.14	5.30	+0.16	Ref.5 (Theory)
Bi_2Te_3	4.02	4.22	+0.20	Ref.21 (Exp.)
Bi_2Se_3	5.22	5.32	+0.10	Ref.22 (Exp.)
Bi_2Te_3	4.05	4.23	+0.18	Ref.23 (Exp.)

The oscillatory part of the transient transmission change was analyzed with two damped oscillations with the vibrational frequencies of 5.2 THz and 10.0 THz (SHG) using by Eq. (3.1). It is difficult to analyze around 0–1.5 ps because of a background non-oscillation component. However, it can be seen from Fig. 3-14 that the oscillation component has continued to 4.5 ps, which is longer than that of bulk ($\tau_{bulk} = 1.4$ ps).

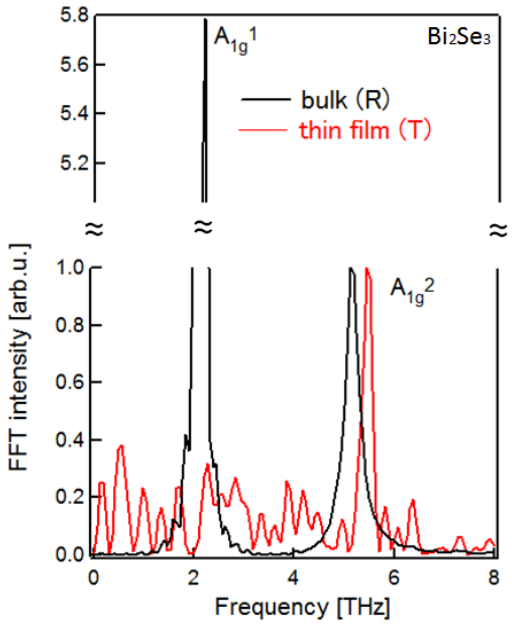

Fig.3-16 Difference between bulk and ultra thin-film of FFT intensity spectra in Bi_2Se_3.

As shown in Fig. 3-16, a similarly result is also obtained in the Bi_2Se_3 thin-film. These obviously blue-shifts of A_{1g}^2 mode are also measured by Raman spectroscopy of the topological insulator Bi_2Se_3 films with varying thickness[22]. The intensity of Raman spectra depends on the number of layers. According to this report, the Raman intensity is the most enhancement as the thickness of 3 QLs (3 nm). It might not be the reason for

the effect of quantum confinement considering the phonon dispersion curve[5]. Therefore, it also might lead to the relative vibration mode directions the blue-shift of the A_{1g}^2 mode, or the effect of topological surface, and require further study.

3.6 Summary

In summary, all of the Raman-active optical phonons (A_{1g}^1, A_{1g}^2, E_g^1, and E_g^2) in topological insulators (Sb_2Te_3, Bi_2Te_3 and Bi_2Se_3) were clearly observed with femtosecond time-resolved reflectivity measurements. Table 3-2 summarizes the obtained frequencies and decaytimes of Raman-active optical phonons. The following are summarizing remarks of this chapter.

Table 3-2 Parameters of coherent phonons in Sb_2Te_3, Bi_2Te_3, and Bi_2Se_3

mode	E_g^1		A_{1g}^1		E_g^2		A_{1g}^2	
	[THz]	[ps]	[THz]	[ps]	[THz]	[ps]	[THz]	[ps]
Sb_2Te_3	1.2	<< 1	2.0	2.6	3.3	1.4	5.0	1.4
Bi_2Te_3	1.2	<< 1	1.8	4.1	3.0	2.9	4.0	1.1
Bi_2Se_3	1.2	<< 1	2.1	3.2	3.9	1.0	5.1	0.9

The frequencies of Bi_2Te_3 are smaller than the other samples. These results indicate that heavier atomic nucleus such as bismuth (Table 3-3(a)) has low frequencies. This implies that the interaction potential is almost same for these three samples since the phonon frequency is proportional to the square root of the force constant over the reduced mass. In fact, the bond strengths are almost same because there is little difference in the lattice parameters of these compounds[24].

The common characteristics of all compounds are (1) the A_{1g}^1 modes have relatively longer decaytimes, (2) the E_g^1 modes are overdamped motion.

(1) The decaytimes are concerned in a collision probability of A_{1g}^2 mode, therefore the higher frequency mode of A_{1g}^2 decay faster.

(2) The reason for the very shorter decaytime of the E_g^1 mode could not be clear. It might be concerned in the direction of atomic motion after the photoexcitation in long time scale (100 ps-order). This fact is a far more complicated problem and needs further study.

I figure out that the amplitude of the in-plane E_g phonons strongly depends on the polarization angle of the pump pulse. The FFT intensity of the E_g phonons and A_{1g} phonons show rotational symmetry through $\pi/2$ and π with a large offset constant, respectively. The polarization dependence of the coherent phonons is based on the Raman tensors. Hence, careful investigation of the appropriate polarization angle of the pump pulse makes it possible to observe even E_g^1 phonons with a very small amplitude ($\Delta R/R_0 \approx 10^{-7}$) and short decay time ($\ll$1 ps).

In addition, I demonstrate the controlling of the specified phonon mode by using double-pulse excitation. It found that fine tuning of the separation time between first pump pulse and second pump pulse enable us to selectively observe the coherent phonon modes, and the accuracy decaytime of A_{1g}^2 mode was observed.

It is also found that the frequency of A_{1g}^2 mode was blue-shifted from bulk to ultra thin-film (3 nm). It might be considered the effect of surface phonon mode not the effect of quantum confinement.

References

1. W. Richter, H. Köhler, and C. R. Becker, "A Raman and far-infrared investigation of phonons in the rhombohedral V_2-VI_3 compounds", *Phys. Stat. Sol. (b)*, **84**, 619 (1977).
2. G. C. Sosso, S. Caravati, and M. Bernasconi, "Vibrational properties of crystalline Sb_2Te_3 from first principles", *J. Phys.: Condens. Matter*, **21**, 095410 (2009).
3. K. M. F. Shahil, M. Z. Hossain, D. Teweldebrhan, and A. A. Balandin, "Crystal symmetry breaking in few-quintuple Bi2Te3 films: Applications in nanometrology of topological insulators", *Appl. Phys. Lett.*, **96**, 153103 (2010).
4. V. Gnezdilov, Y. G. Pashkevich, H. Berger, E. Pomjakushina, K. Conder, and P. Lemmens, "Helical fluctuations in the Raman response of the topological insulator Bi_2Se_3", *Phys. Rev. B*, **84**, 195118 (2011).
5. V. Chis, I. Yu. Sklyadneva, K. A. Kokh, E. V. Chulkov, "Vibrations in binary and ternary topological insulators: First-pronciples calculations and Raman spectroscopy measurements", *Phys. Rev. B*, **86**, 174304 (2012).
6. V. V. Atuchin, T. A. Gavrilova, K. A. Kokh, N. V. Kuratieva, N. V. Pervukhina, and N. V. Surovtsev, "Structural and vibrational properties of PVT grown Bi_2Te_3 microcrystals", *Solid State Commun.*, **152**, 1119 (2012).
7. A. Q. Wu, X. Xu, and R. Venkatasubramanian, "Ultrafast dynamics of photoexcited coherent phonon in Bi_2Te_3 thin films", *Appl. Phys. Lett.*, **92**, 011108 (2008).
8. Y. Wang, X. Xu, and R. Venkatasubramanian, "Reduction in coherent phonon lifetime in Bi_2Te_3/Sb_2Te superlattices", *Appl. Phys. Lett.*, **93**, 113114 (2008).
9. Y. Li, V. A. Stoica, L. Endicott, G. Wang, C. Uher, and R. Clarke, "Coherent optial phonon spectroscopy studies of femtosecond-laser modified Sb_2Te_3 films", *Appl. Phys. Lett.*, **97**, 171908 (2010).
10. J. Qi, X. Chen, W. Yu, P. Cadden-Zimansky, D. Smimov, N. H. Tolk, I. Miotkowski, H. Cao, Y. P. Chen, Y. Wu, S. Qiao, and Z. Jiang, "Ultrafast carrier and phonon dynamics in Bi_2Se_3 crystals", *Appl. Phys. Lett.*, **97**, 182102 (2010).
11. N. Kumar, B. A. Ruzicka, N. P. Butch, P. Syers, K. Kirshenbaum, J. Paglione, and H. Zhao,

"Spatially resolved femtosecond pump-probe study of topological insulator Bi_2Se_3", *Phys. Rev. B*, **83**, 235306 (2011).

12. A. S. Pine and G. Dresselhaus, "Raman spectra and lattice dynamics of tellurium", *Phys. Rev. B*, **4**, 356 (1971).
13. K. Ishioka, M. Kitajima, J. Irisawa, Y. Hironaka, K. Ushida, and K. G. Nakamura, "Amplitude saturation of coherent phonon excited by field screening in CdTe", *Jpn. J. Appl. Phys.*, **45**, 9111(2006).
14. L. Krusin-Elbaum, C. Cabral Jr., K. N. Chen, M. Copel, D. W. Abraham, K. B. Reuter, S. M. Rossnagel, J. Bruley, and V. R. Deline, "Evidence for segregation of Te in $Ge_2Sb_2Te_5$ films: Effect on the "phase-change" stress", *Appl. Phys. Lett.*, **90**, 141902 (2007).
15. R. Loudon, "The Raman effect in crystals", *Adv. Phys*., **50**, 813 (2001).
16. K. Ishioka, M. Kitajima, and O. V. Misochko, "Temperature dependence of coherent A_{1g} and E_g phonons of bismuth", *J. Appl. Phys.*, **100**, 093501(2006).
17. H. Takahashi, K. Kato, H. Nakano, M. Kitajima, K. Ohmori, and K. G. Nakamura, "Optical control and mode selective excitation of coherent phonons in $YBa_2Cu_3O_{7-}\delta$", *Solid State Commun.*, **149**, 1955 (2009).
18. S. Hayashi, K. Kato, K. Norimatsu, M. Hada, Y. Kayanuma, and K. G. Nakamura, "Measuring quantum coherence in bulk solids using dual phase-locked optical pulses", *Scientific reports*, **4** (2014) 4456.
19. I. Katayama, S. Koga, K. Shudo, J. Takeda, T. Shimada, A. Kubo, S. Hishita, D. Fujita, and M. Kitajima, "Ultrafast dynamics of surface-enhanced Raman scattering due to Au nanostructures", *Nano Lett.*, **11**, 2648 (2011).
20. S. –L. Li, H. Miyazaki, H. Song, H. Kuramochi, S. Nakaharai, and K. Tsukagashi, "Quantitative Raman spectrum and reliable thickness identification for atomic layers on insulating substarates", *ACS Nano*, **6**, 7381 (2012).
21. R. He, Z. Wang, R. L. J. Qiu, C. Delaney, B. Beck, T. E. Kidd, C. C. Chancey, and X. P. A. Gao, "Observation of infrared-active modes in Raman scattering from topological insulator nanoplates", *Nano Tech*., **23**, 455703 (2012).
22. W. Dang, H. Peng, H. Li, P. Wang, and Z. Liu, "Epitaxial heterostructures of ultrathin topological insulator nanoplate and graphene", *Nano Lett*., **10**, 2870 (2010).
23. C. Wang, X. Zhu, L. Nilsson, J. Wen, G. Wang, X. Shan, Q. Zhang, S. Zhang, J. Jia, and Q.

Xue, "*In situ* Raman spectroscopy of topological insulator Bi_2Te_3 films with varying thickness", *Nano Res.* **6**, 688 (2013).

24. W. Zhang, R. Yu, H. –J. Zhang, Z. Dai, and Z. Fang, "First-principle studies of the three-dimensional strong topological insulators Bi_2Te_3, Bi_2Se_3, and Sb_2Te_3", *New J. Phys.*, **12**, 065013 (2010).

Chapter 4.
Carrier dynamics

4.1 Introduction

A non-trivial feature of the topological insulator is the Dirac-cone-type dispersion, which is formed at the gapless surface states. The Dirac Fermions are known as massless electrons existing in the Dirac cone and have high electric mobility. Thus, they are expected to be used as high-efficiency, low-power electronic devices and spintronic devices. The electric-population dynamics of photoexcited topological insulators were directly demonstrated by using Tr-ARPES[1-9]. Optically excited carriers in a Bi_2Se_3 by interband photoexcitation (1.5 eV) are immediately scattered into the bulk conduction band (BCB) and surface state, and wholly relax in the timescale of ~10 ps[2]. The electrons in BCB nearby the Dirac cone invariably relax though the surface conductive channel. Very recently, the dynamics of photoexcited electrons at the Dirac cone are also observed in *p*-type Sb_2Te_3[5]. Figure 4-1 shows the result of Tr-ARPES by S. Zhu *et al*[9], they conclude that the relaxation of photoexcited surface carriers in the timescale of ~3 ps. However, the underlying surface state properties as well as mechanism of the specific gapless surface state have not been particularly and quantitatively clarified, yet. I will discuss briefly the relaxation processes of surface electrons by comparing the present results with time- and angle-resolved photoemission spectroscopy (Tr-ARPES).

Relaxation processes of excited carrier have also been investigated by using the optical pump and mid–near IR probe reflective spectroscopy. The dynamics of photoexcited electrons in *n*-type Bi_2Se_3 was reported using the time-resolved reflectivity measurement with near-IR (1.5 eV) pump and IR probe with the photon energy range

from 0.09 to 0.15 eV by C. W. Luo *et al*[10]. This probe photon energy of mid-IR was much smaller than the band gap (~0.3 eV) and the plasma frequency (~0.68 eV)[11]. In the report, they indicate that the reflectivity depends on the doping levels of *n*-type Bi_2Se_3 single crystals. For the case of lower carrier density ($n = 0.25 \times 10^{18} cm^{-3}$), the reflectivity was dominated by the free carrier absorption in the BCB and Dirac cone. The relaxation process of excited carriers were revealed to pass the intervalley scattering from the Γ to L valley.

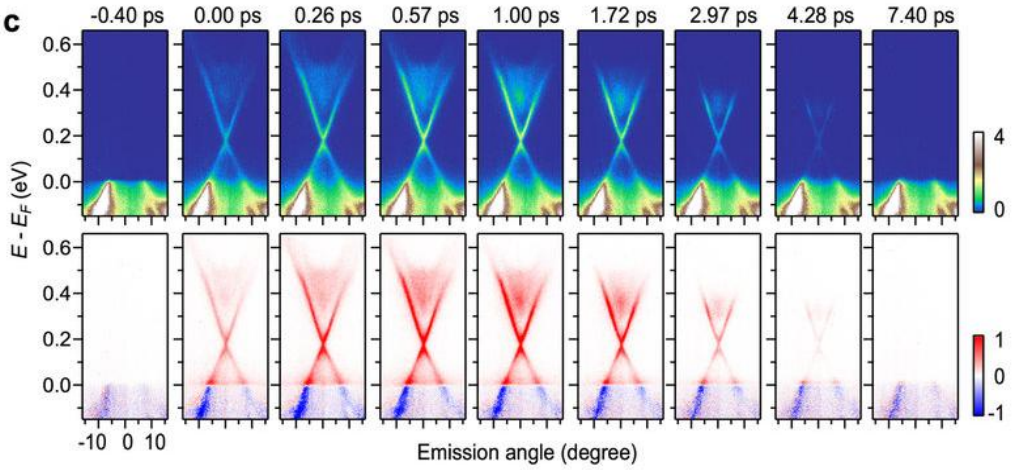

Fig. 4-1 Tr-ARPES images of reference[9] in Fig. 2(c) Tr-ARPES images. Upper and lower panels show Tr-ARPES and difference to that recorded before pump.

In the present experiment, I carried out the time-resolved reflectivity measurement on *p*-type Sb_2Te_3 using mid-IR probe light based on the results of previous research, which might be avoid the free carrier absorption of BCB and the interband transition. The probe photon energy is much smaller than the band gap of ~0.33 eV as illustrated in Fig. 4-2. The optical pump pulses (800 nm, 1.5 eV) operated at a repetition rate of 500 Hz and laser fluence of ~1.5 mW. The mid-IR probe pulse (4800–10000 nm, 0.12–0.26 eV) was derived with pulse duration of 120 fs at a repetition rate of 1 kHz. The incident pump and probe pulses are parallel to the sample along the *c* axis, and focused on a diameter of 240 μm. The laser penetration depth of the pump light (1.5 eV) was estimated to be about 19 nm[12]. The carrier of this sample is estimated to be 7.63×10^{19} cm^{-3} at room temperature. Figure 4-3 shows the experimental conditions in comparison with previous research[10].

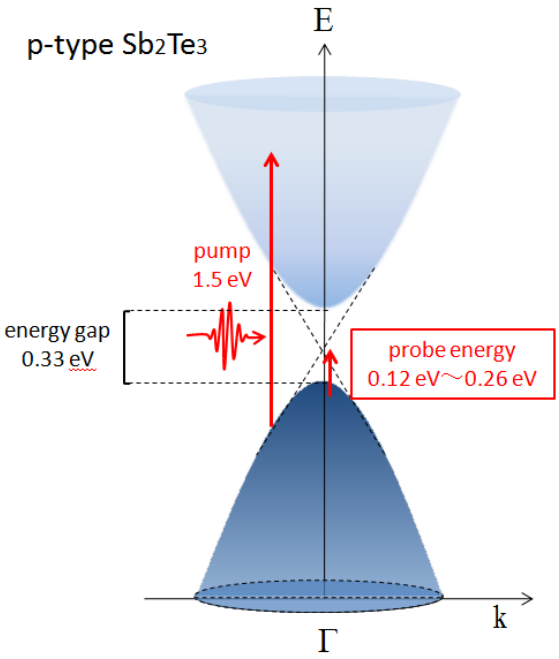

Fig. 4-2 Image of optical pump (1.5 eV) and mid-IR probe (0.12–0.26 eV) experiments in *p*-type Sb_2Te_3.

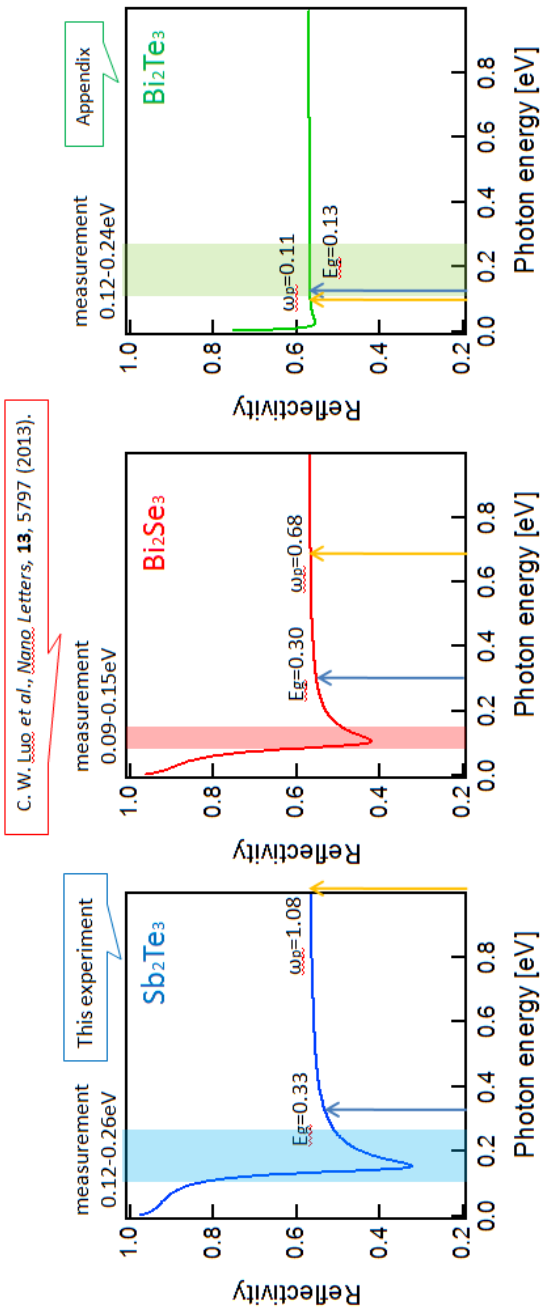

Fig. 4-3 Comparing with the experimental condition between the previou s researches and this work; Sb_2Te_3 (this work), Bi_2Se_3[10], and Bi_2Te_3 (Appendix).

4.2 Plasma frequency

Conducting materials like gold, silver and copper have higher reflectivity in the far-infrared due to collective motion of free carriers: plasma oscillation. The plasma oscillation plays the important role on cancellation of the charge of electric field (so-called plasma frequency), so that the incident electromagnetic wave below the plasma frequency cannot penetrate into the bulk, and that is mostly reflected near the surface. Here, first of all, I measured a static reflectivity in order to decide the plasma frequency of the prepared Sb_2Te_3 single crystal. As mentioned earlier chapter (Fig. 2-10), the minimum of reflectivity at photon energy of ~0.15 eV is so-called the plasma edge. Usually, the reflectivity spectrum of topological insulator is analyzed in the context of a conventional Drude-Lorentz model[11,13]. A Drude part represents the electrical conduction in the metallic surface state and a Lorentz part represents absorption in the bulk state. The Drude-Lorentz model is expressed as

$$\varepsilon_1 = \left(\varepsilon_\infty - \frac{{\omega_p}^2\omega^2}{\omega^4 + \gamma^2\omega^2}\right) + \left(1 + \frac{{\omega_p}^2({\omega_0}^2 - \omega^2)}{({\omega_0}^2 - \omega^2)^2 + \Gamma^2\omega^2}\right), \tag{4.1}$$

$$\varepsilon_2 = -\frac{\gamma{\omega_p}^2\omega}{\omega^4 + \gamma^2\omega^2} + \frac{{\omega_p}^2\Gamma\omega}{({\omega_0}^2 - \omega^2)^2 + \Gamma^2\omega^2}, \tag{4.2}$$

$$n^2 = \frac{\varepsilon_1 + \sqrt{{\varepsilon_1}^2 + {\varepsilon_2}^2}}{2}, \tag{4.3}$$

$$k^2 = \frac{-\varepsilon_1 + \sqrt{{\varepsilon_1}^2 + {\varepsilon_2}^2}}{2}, \tag{4.4}$$

$$R = \frac{(n-1)^2 + k^2}{(n+1)^2 + k^2}, \tag{4.5}$$

where ε_1 and ε_2 are respective real part and imaginary part of material permittivity, ε_∞ is the high frequency permittivity, ω is the angular frequency, ω_p is the plasma frequency, ω_0 is the absorption energy, γ and Γ are the relaxation frequency of Drude and Lorentz part, respectively. By fitting the reflectivity spectrum (Fig. 2-10) with Eq. (5.5), the parameters were obtained as follows: $\varepsilon_\infty = 50$, $\omega_p = 1.08$, $\gamma = 0.045$, $\omega_0 = 0.33$ and $\Gamma = 1$. The direct band gap for Sb_2Te_3 is experimented ~0.33 eV at room temperature as shown in chapter 2, Fig. 2-7. Here, the plasma frequency (ω_p) can be written as

$$\omega_p^2 = \frac{Nq^2}{m^*\varepsilon_0}, \tag{4.6}$$

where m^* is the effective mass, N is the carrier density, q is the electronic charge, and ε_0 is the vacuum permittivity. That is the carrier effective mass is expressed as

$$m^* = \frac{Nq^2}{\omega_p^2\varepsilon_0}. \tag{4.7}$$

The effective mass is obtained to $m^* = 27 \times 10^{-31}$ kg, which is three times as heavy as the free electron rest mass ($m_0 = 9.10938 \times 10^{-31}$ kg) due to the fact that the heavy hole carriers.

4.3 Results and Discussion

Figure 4-4 shows typical examples of reflectivity change as a function of time delay measured with probe photon energy range at (a) 0.12, (b) 0.13, (c) 0.15, (d) 0.16, (e) 0.20, and (f) 0.26 eV. For the case of low photon energy (0.12 eV), the signal definitely presents a negative peak as shown in Fig. 4-4(a). However, the signal changed to a positive peak for the high photon-energy (0.26 eV) case as shown in Fig. 4-4(f). As a result, it found that the initial responses within ~1 ps vary according to the probe photon energy. In addition, the reflectivity signals included two-step of the relaxation process both fast decay ($\Delta t \sim 2$ ps) and slow decay ($\Delta t \sim 10$ ps).

Figure 4-5 showed the change rate of reflectivity (ΔR) as a function of time delay in the photon energy range from 0.12 to 0.26 eV. The positive and negative change is found for the probe photon energy at lower and higher than the plasma edge, respectively. There are some mixed signals around the plasma edge of ~0.15 eV. The reflectivity signals significantly change at ($\Delta t = 1$ ps), and recovered within 10 ps.

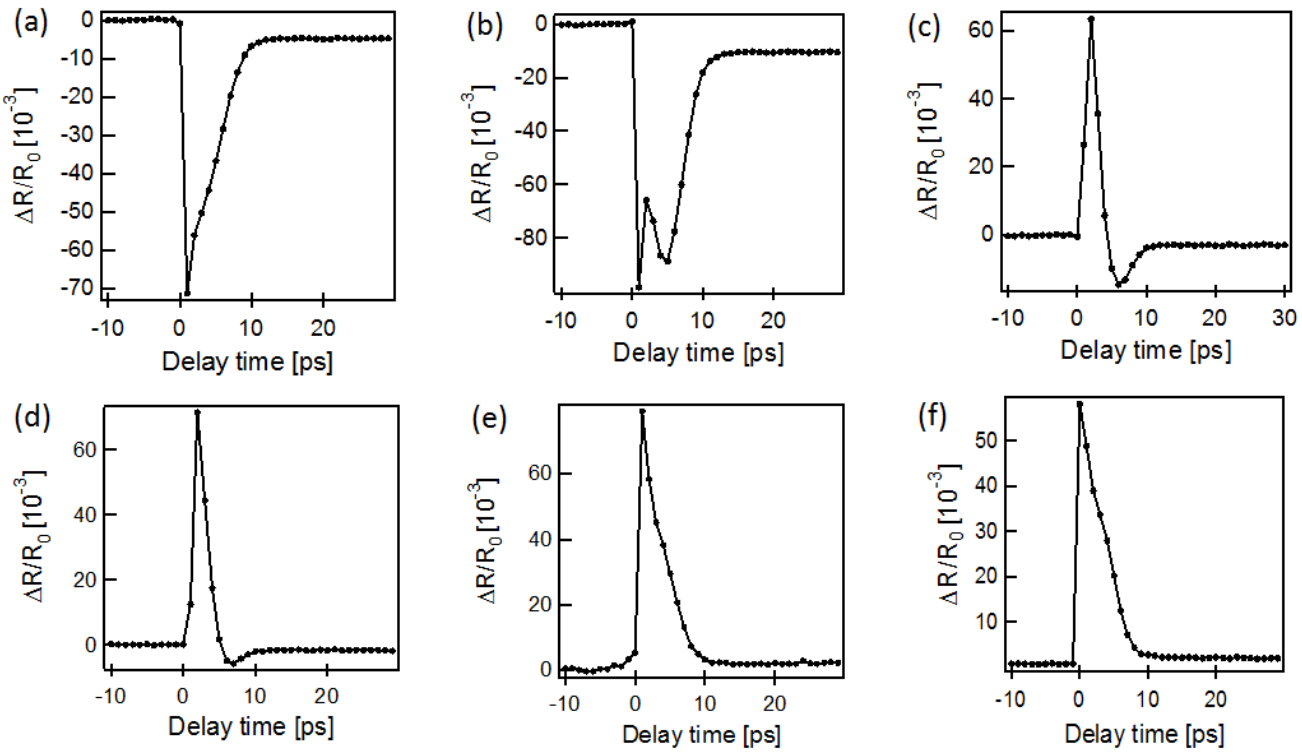

Fig. 4-4 Transient reflectivity change ($\Delta R/R_0$) at the photon energy of (a) 0.12 eV, b) 0.13 eV, (c) 0.15 eV, (d) 0.16 eV, (e) 0.20 eV, and (f) 0.26 eV.

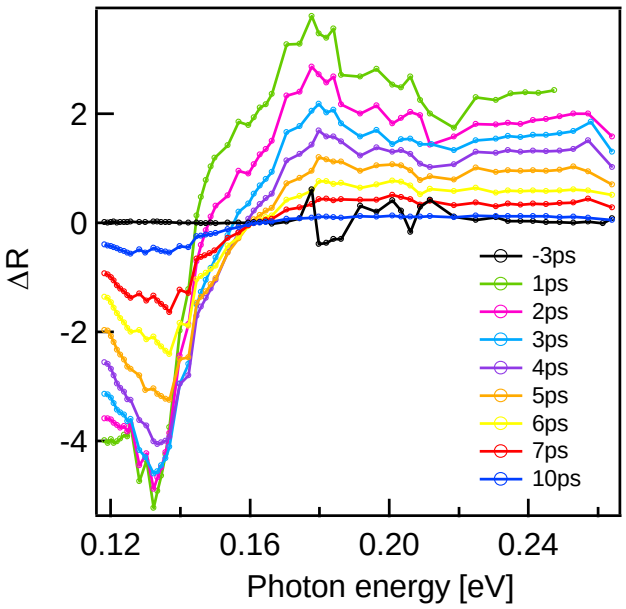

Fig. 4-5 Difference of reflectivity spectra (ΔR) of Sb_2Te_3 as a function of energy and time delay.

In general, the photoexcitation changes carrier density when the light energy is higher than the band gap. As a result, the plasma frequency changes in proportional to the carrier density (see Eq. (4.6)). I simulated the reflectivity spectra with changing the plasma frequency using a Drude-Lorentz model. The red line in Fig. 4-6 presents the reflectivity spectrum with original plasma frequency ($\omega_p = 1.08$). In the case of increasing the plasma frequency of $\omega_p + \Delta\omega = 1.08 + 0.1$ leads to the blue-shift (purple line) of the reflectivity spectrum (R), while the case of decreasing the plasma frequency of $\omega_p - \Delta\omega = 1.08 - 0.1$ leads to the red-shift (green line) of R. At higher or lower carrier density, the plasma edge shifts to the higher or lower frequency side compared to the pristine sample, respectively. The differential spectrum shows negative and positive at lower and higher frequency side from the original plasma edge, when the carrier density decreases. Theoretically calculations show that the reflectivity signals of both positive and negative associated with probing photon energy can be explained merely a plasma frequency change.

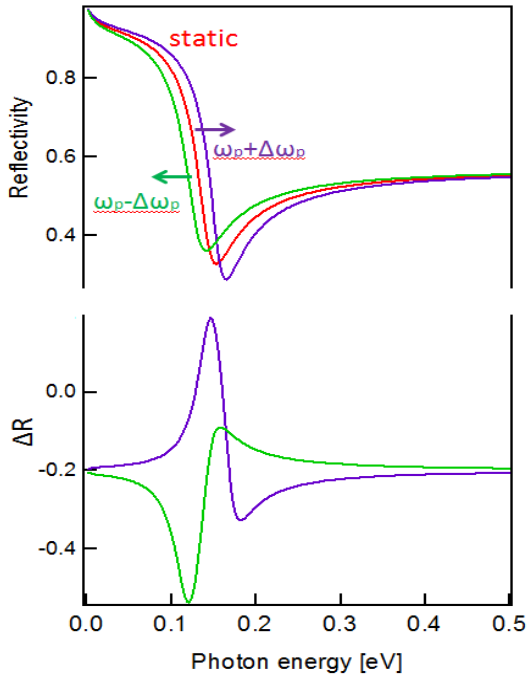

Fig. 4-6 Reflectivity spectra dependence of the plasma frequency (upper) and difference of the reflectivity (down); original plasma frequency ($\omega_p = 1.08$) (red line), increased plasma frequency ($\omega_p + \Delta\omega = 1.08 + 0.1$) (purple line), and decreased plasma frequency ($\omega_p - \Delta\omega = 1.08 - 0.1$) (green line).

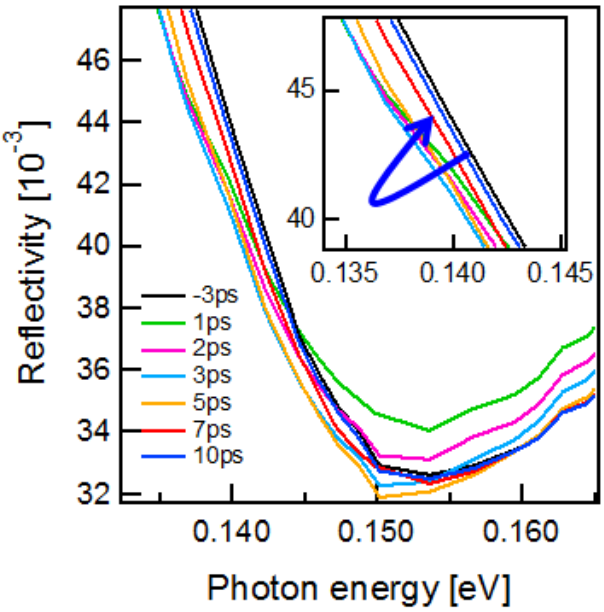

Fig. 4-7 Reflectivity spectra at a pump-probe delay times (Δt = -3–10 ps) as a function of probe photon energy.

Figure 4-7 shows reflectivity spectra at several different pump-probe delays as a function of probe photon energy. It is clearly shown that the reflectivity spectra shift toward low energy side after photoexcitation. The reflectivity spectra were dominantly determined with the carrier density due to photoexcitation, and it was predicted by all results in this mid-IR experiments that the carrier density decreasing in spite of photoexcitation (*i.e.*, plasma frequency was redshift) as mentioned above. These reflectivity spectra were analyzed with Eq.(4.1)–(4.5) operating the plasma frequency (ω_p).

Figure 4-8 shows fitting of the reflectivity spectra with Eq.(4.1)–(4.5) in the context of a Drude model. The plasma frequencies at each delay were obtained: ω_p=1.080 at -3 ps, ω_p=1.054 at 1 ps, ω_p=1.060 at 2 ps, ω_p=1.063 at 3 ps, ω_p=1.068 at 5 ps, ω_p=1.074 at 7 ps, and ω_p=1.080 at 10 ps. The plasma frequency decreased just after the pump pulse irradiation (<1 ps) and recovered within ~10 ps.

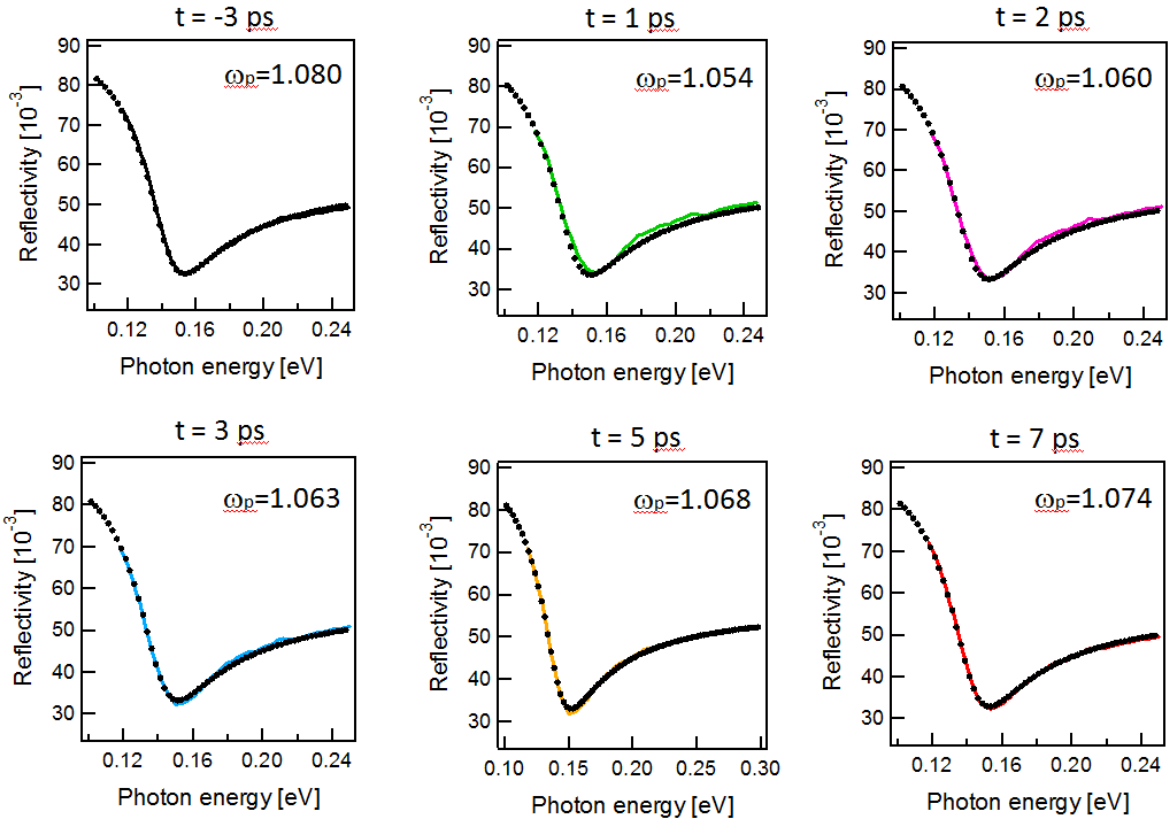

Fig. 4-8 The reflectivity spectra and fitting curves with using a conventional Drude-Lorentz model. The fitting parameter of plasma frequencies at each delay: ω_p=1.080 (Δt =-3 ps) ω_p=1.054 (Δt =1 ps), ω_p=1.060 (Δt =2 ps), ω_p=1.063 (Δt =3 ps), ω_p=1.068 (Δt =5 ps), and ω_p=1.074 (Δt =7 ps).

The previous research of *n*-type Bi_2Se_3 studied by C. W. Luo *et al.*[10], in GaAs studied by N. A. van Dantzing *et al.*[14], and in InP studied by P. N. Saeta *et al.*[15] were indicated an intervalley scattering leading to the redshift of the reflectivity. However, in the present experiment, the redshift was predicted to cause by decreasing of the plasma frequency due to the deduction of carriers. Figure 4-9 shows the plasma frequency as a

function of delay analyzed with Drude-Lorentz model (Fig. 4-8). There is a slightly difference between before and after photoexcitation around 0.025 eV. Because the plasma frequency is proportional to carrier density, it can be rewritten as the change of carrier density.

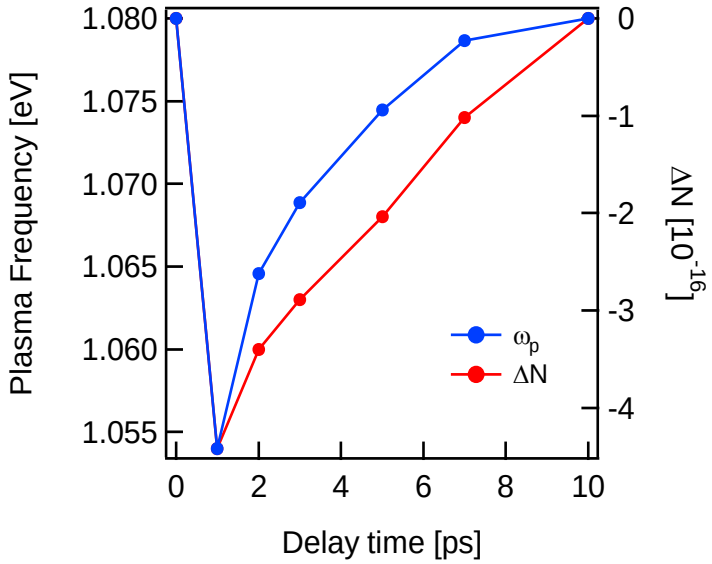

Fig. 4-9 Photoinduced plasma frequency shift and carrier density changes (ΔN) as a function of delay time analyzed with Drude-Lorentz model.

Figure 4-9 shows the carrier density change as a function of delay. It is found that the relaxation process was composed of two time constants. The first process occurs within Δt ~ 1-3 ps, followed by a slower relaxation during Δt~ 3-10 ps. The second relaxation was analyzed with a single exponential and the decay time was estimated to be $\tau = 3.3$ ps. This relaxation is faster than the common semiconductors such as GaAs ($\tau \sim 1$ ns[16]). Here, this faster decay time compares with graphene, which is also having a Dirac-cone-type dispersion, the relaxation processes of photoexcited carriers in the graphene have two distinct time scales; $\tau_1 = 70 - 120$ fs, $\tau_2 = 0.4 - 1.7$ ps[17]. Then, the decay time of topological insulator Sb_2Te_3 is about two times longer than that of graphene, but both of them are enough faster than any other materials (nothing Dirac-cone-type dispersion). Therefore, I conclude that the faster relaxation time of Sb_2Te_3 implies a characteristic of topological insulator having a Dirac cone surface state, like similarly to a graphene.

4.4 Summary

The change in reflection spectrum after the pump pulse irradiation is explained in terms of a change in carrier density in the bulk valence band (BVB). Figure 4-10 shows schematic of this process. For the pristine sample (before the pump pulse irradiation), the IR-pulse reflection is governed by scattering due to holes in the bulk state, because the pristine sample in the *p*-type Sb_2Te_3 (process A). When the pump pulse (1.5 eV) irradiates the sample, photo absorption occurs and electrons at the deep-energy level in the valence band are excited to the conduction band (process B). The generated holes interact with electrons in non-equilibrium condition just after the photoexcitation and electrons just slightly below the Fermi edge is excited above the Fermi edge. Thus the effective density of carriers near the surface, which can scatter the IR pulse, decreases. This type of electron excitation is also reported by the Tr-ARPES[9]. The decrease of the effective carrier density may correspond to decrease of the plasma frequency after the photoexcitation. The electrons in non-equilibrium state relax to below the Fermi edge within 1 ps (process C). In addition, the photoexcited electrons relax through the surface band to the BVB within 10 ps (process D). Without the surface state, the relaxation of the photoexcited electrons in the conduction of the photoexcited electrons should be very slow (in nanosecond region).

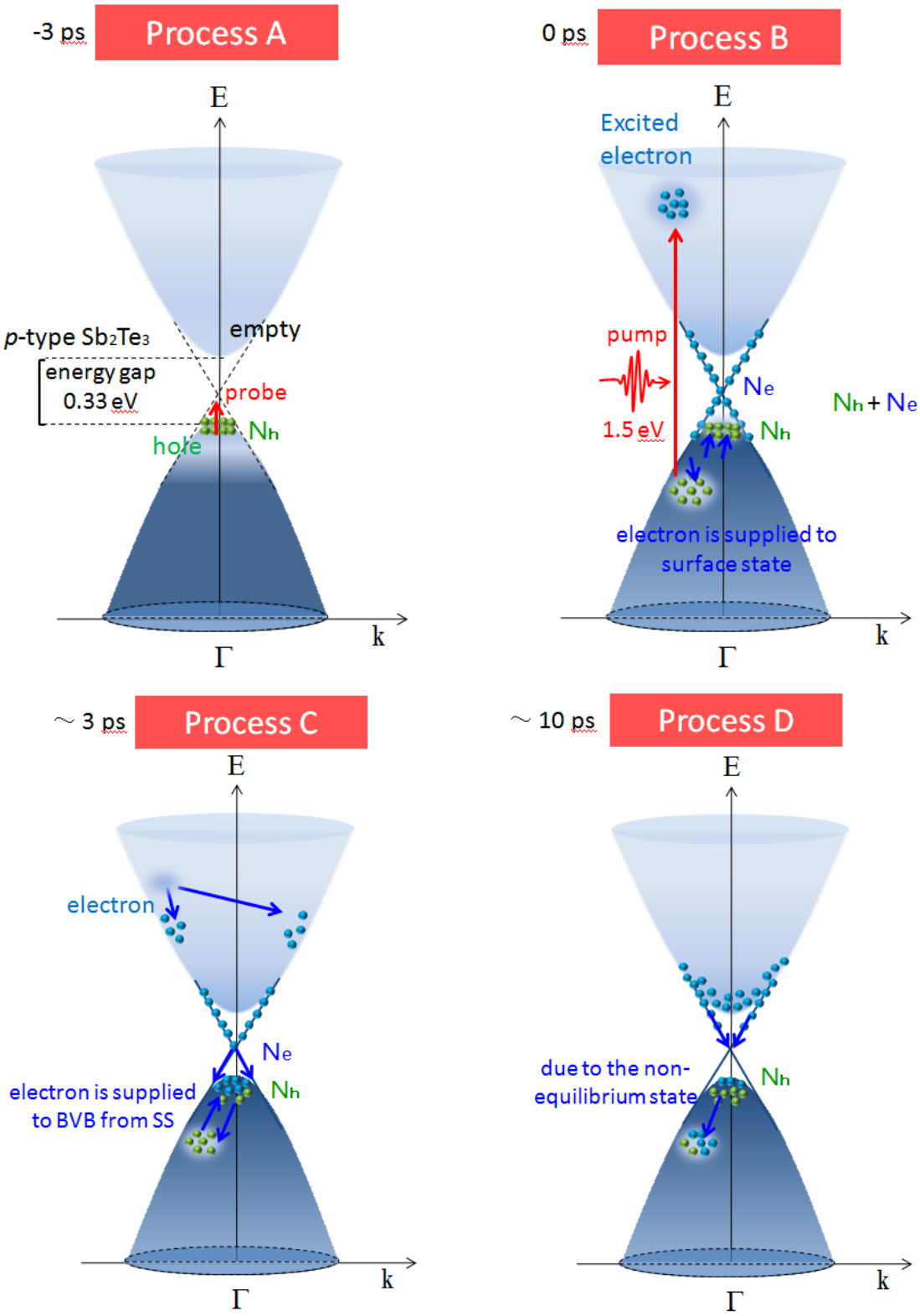

Fig. 4-10 Illustration of the photoexcited relaxation process of *p*-type Sb_2Te_3.

References

1. A. Creoaldi, B. F. Cilento, M. Zacchigna, C. Grazioli, H. Berger, Ph. Bugnon, K. Kern, M. Grioni, and F. Parmigiani, "Ultrafast photodoping and effective Fermi-Dirac particles in Bi_2Se_3", *Phys. Rev. B*, **86**, 205133 (2012).
2. J. A. Sobota, S. Yang, J. G. Analytis, Y. L. Chen, I. R. Fisher, P. S. Kirchmann, and Z. –X. Shen, "Ultrafast optical excitation of a persistent surface-state population in the topological insulator Bi_2Se_3", *Phys. Rev. Lett.*, **108**, 117403 (2012).
3. A. Crepaldi, B. Ressel, F. Cilento, M. Zacchigna, C. Grazioli, H. Berger, Ph. Bugnon, K. Kern, M. Grioni, and F. Parmigiani, "Ultrafast photodoping and effective Fermi-Dirac distribution of the Dirac particles in Bi_2Se_3", *Phys. Rev. B*, **86**, 205133 (2012).
4. M. Hajlaoui, E. Papalazarou, J. Mauchain, G. Lantz, N. Moisan, D. Boschetto, Z. Jiang, I. Miotkowski, Y. P. Chen, A. Taleb-Ibrahimi, L. Perfetti, and M. Marsi, "Ultrafast surface carrier dynamics in the topological insulator Bi_2Te_3", *Nano Lett*., **12**, 3532 (2012).
5. Y. H. Wang, D. Hsieh, E. J. Sie, H. Steinberg, D. R. Gardner, Y. S. Lee, P. Jarillo-Herrero, and N. Gedik, "Measurement of intrinsic Dirac Fermion cooling on the surface of the topological insulator Bi_2Se_3 using time-resolved and angle-resolved photoemission spectroscopy", *Phys. Rev. Lett*., **109**, 127401 (2012).
6. A. Crepaldi, F. Cilento, B. Ressel, C. Cacho, J. C. Johannsen, M. Zacchigna, H. Berger, Ph. Bugnon, C. Grazioli, I. C. E. Turcu, E. Springate, K. Kern, M. Grioni, and F. Parmigiani, "Evidence of reduced surface electron-phonon scattering in the conduction band of Bi_2Se_3 by nonequilibrium ARPES", *Phys. Rev. B*, **88**, 121404 (2013).
7. J. A. Sobota, S. –L. Yang, D. Leuenberger, A. F. Kemper, J. G. Analytis, I. R. Fisher, P. S. Kirchmann, T. P. Devereaux, and Z. –X. Shen, "Distinguishing bulk and surface electron-phonon coupling in the topological insulator Bi_2Se_3 using time-resolved photoemission spectroscopy", *Phys. Rev. Lett*., **113**, 157401 (2014).
8. J. Reimann, J. Güdde, K. Kuroda, E. V. Chulkov, and U. Höfer, "Spectroscopy and dynamics of unoccupied electric states of the topological insulators Sb_2Te_3 and Sb_2Te_2S", *Phys. Rev. B*, **90**, 081106(R) (2014).

9. S. Zhu, Y. Ishida, K. Kuroda, K. Sumida, M. Ye, J. Wang, H. Pan, M. Taniguchi, S. Qiao, S. Shin, and A. Kimura, "Ultrafast electron dynamics at the Dirac node of the topological insulator Sb_2Te_3", *Sci. Rep.*, **5**, 13213 (2015).
10. C. W. Luo, H. J. Wang, S. A. Ku, H. –J. Chen, T. T. Yeh, J. –Y. Lin, K. H. Wu, J. Y. Juang, B. L. Young, T. Kobayashi, C. –M. Cheng, C. –H. Chen, K. –D. Tsuei, R. Sankar, F. C. Chou, K. A. Kokh, O. E. Tereshchenko, E. V. Chulkov, Yu. M. Andreev, and G. D. Gu, "Snapshots of Dirac Fermions near the Dirac point in topological insualtors", *Nano Lett.*, **13**, 5797 (2013).
11. P. Di. Pietro, F. M. Vitucci, D. Nicoletti, L. Baldassarre, P. Calvani, R. Cava, Y. S. Hor, U. Schade, and S. Lupi, "Optical conductivity of bismuth-based topological insulators", *Phys. Rev. B*, **86**, 045439 (2012).
12. M. Kuwahara, R. Endo, K. Tsutsumi, F. Morikasa, T. Tsuruoka, T. Fukaya, M. Suzuki, M. Susa, T. Endo, and T. Tadokoro, "Approach for measuring complex refractive index of molten Sb_2Te_3 by spectroscopic ellipsometry", *Appl. Phys. Lett.*, **100**, 101910 (2012).
13. S. V. Dordevic, M. S. Wolf, N. Stojilovic, H. Lei, and C. Petrovic, "Signatures of charge inhomogeneities in the infrared spectra of topological insulators Bi_2Se_3, Bi_2Te_3, and Sb_2Te_3", *J. Phys.: Condens. Matter*, **25**, 075501 (2013).
14. N. A. van Dantzing, and P. C. M. Planken, "Time-resolved far-infrared reflectance of *n*-type GaAs", *Phys. Rev. B*, **59**, 1586 (1999).
15. P. N. Saeta, J. F. Federici, B. I. Greene, and D. R. Cykaar, "Intervalley scattering in GaAs and InP probed by pulsed far-infrared transmission spectroscopy", *Appl. Phys. Lett.*, **60**, 1477 (1992).
16. S. Gupta, M. Y. Frankel, J. A. Valdmanis, J. F. Whitaker, and G. A. Mourou, "Subpicosecond carrier lifetime in GaAs grown by molecular beam epitaxy at low temperatures", *Appl. Phys. Lett.*, **59**, 3276 (1991).
17. J. M. Dawlaty, S. Shivaraman, M. Chandrashekhar, F. Rana, and M. G. Spencer, "Measurement of ultrafast carrier dynamics in epitaxial graphene", *Appl. Phys. Lett.*, **92**, 042116 (2008).

Chapter 5.
General conclusion

In this dissertation, I studied ultrafast dynamics of photoexcited electrons and coherent phonons in the topological insulators (Sb_2Te_3, Bi_2Te_3, and Bi_2Se_3) by using femtosecond time-resolved near-IR and mid-IR reflectivity measurements. The dynamics of Raman active optical phonons (E_g^1, E_g^2, A_{1g}^1, and A_{1g}^2) have been investigated. Amplitude of these coherent phonons strongly depends on polarization of an excitation pulse. Fine tuning of the polarization enables the observation of even E_g^1 phonons, which have a smaller amplitude (10^{-7}) and a shorter decay time ($\ll 1$ ps). The frequencies and decaytimes of all the Raman active optical phonons are summarized in Table 5-1. These coherent phonons are generated by interaction with photoexcited electrons, thereafter decay within 4 ps.

Table 5-1 Parameters of coherent phonons in Sb_2Te_3, Bi_2Te_3, and Bi_2Se_3.

mode	E_g^1		A_{1g}^1		E_g^2		A_{1g}^2	
	[THz]	[ps]	[THz]	[ps]	[THz]	[ps]	[THz]	[ps]
Sb_2Te_3	1.2	<< 1	2.0	2.6	3.3	1.4	5.0	1.4
Bi_2Te_3	1.2	<< 1	1.8	4.1	3.0	2.9	4.0	1.1
Bi_2Se_3	1.2	<< 1	2.1	3.2	3.9	1.0	5.1	0.9

The dynamics of photoexcited topological insulators *p*-type Sb_2Te_3 has been studied by using the transient mid-IR reflectivity (0.12-0.25 eV). The time evolution of the photo-excited carrier density (hole) was determined by analyzing the transient reflection spectra by using the Drude-Lorentz model. In this experiment, the transient reflectivity changes are affected by the change of hole carrier in the bulk-valence band. Therefore what I observed in this experiment is a relaxation process through a Dirac cone surface state of photoexcited electrons.

Finally I found the photoexcited dynamics is as following: electrons excited in the bulk-conduction band relax to the band edge within 4 ps by interacting with optical phonons. The generated holes in the bulk-valence band are occupied by topological surface electrons (Dirac Fermions) via auger electron transition. Thereafter, the excited electrons go back to the bulk-valence band within 10 ps via recombination of holes with electrons relaxed through a Dirac cone surface state. The faster relaxation time ($\tau = 3.3$ ps) implies a characteristic of topological insulator having a Dirac cone surface state, like similarly to a graphene.

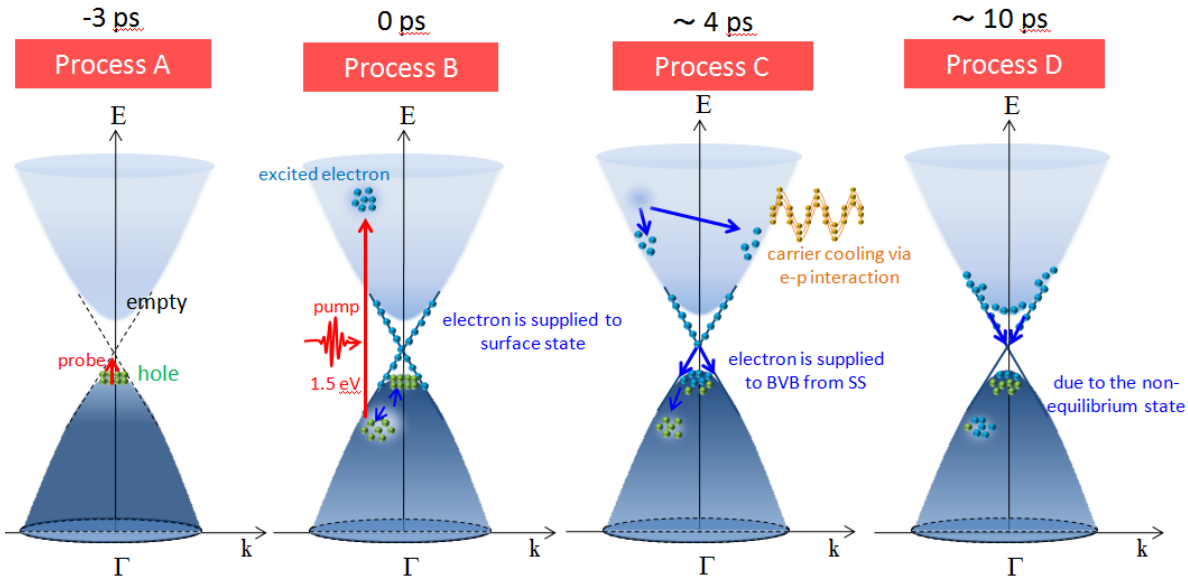

Fig. 5-1 Illustration of the photoexcited relaxation process of *p*-type Sb_2Te_3.

List of publications

Peer-reviewed articles

1. K. Norimatsu, M. Hada, S. Yamamoto, T. Sasagawa, M. Kitajima, Y. Kayanuma, and K. G. Nakamura, Dynamics of all the Raman-active coherent phonons in Sb_2Te_3 revealed via transient reflectivity, *J. Appl. Phys*., **117** (2015) 143102.
2. K. Norimatsu, J. Hu, A. Goto, K. Igarashi, T. Sasagawa, and K. G. Nakamura, Coherent optical phonons in a Bi_2Se_3 single crystal measured via transient anisotropic reflectivity, *Solid State Commun.*, **157** (2013) 58.
3. K. Norimatsu, J. Hu, A. Goto, K. Igarashi, T. Sasagawa, K. G. Nakamura, Dynamics of optical phonons in Bi_2Se_3 crystal studied using femtosecond time-resolved reflection measurement, *Proceedings of the EPJ Web of Conferences*, **41** (2013) pp.03008.
4. K. G. Nakamura, J. Hu, K. Norimatsu, A. Goto, K. Igarashi, and T. Sasagawa, Observation of coherent higher frequency A_{1g}^2 phonon in Bi_2Se_3 using femtosecond time-resolved reflection measurement, *Solid State Commun.*, **152** (2012) 902.

Other contributions

1. S. Hayashi, K. Kato, K. Norimatsu, M. Hada, Y. Kayanuma, and K. G. Nakamura, Measuring quantum coherence in bulk solids using dual phase-locked optical pulses, *Scientific reports*, **4** (2014) 4456.
2. J. Hu, K. Ichiyanagi, T. Doki, A. Goto, T. Eda, K. Norimatsu, S. Harada, D. Horiuchi, Y. Kabasawa, S. Hayashi, S. Uozumi, N. Kawai, S. Nozawa, T. Sato, S. Adachi, and K. G. Nakamura, Complex structural dynamics of bismuth under laser-driven compression, *Appl. Phys. Lett.*, **103** (2013) 161904.

Conference contributions

1. K. Norimatsu, M. Hada, S. Tanaka, K. Igarashi, T. Ishikawa, K. Onda, T. Sasagawa, and K. G. Nakamura, Ultrafast dynamics of photoexcited electrons and coherent phonons in the topological insulator, (Pacifichem 2015, Hawaii, December 2015).
2. K. Norimatsu, S. Uozumi, S. Hayashi, K. Igarashi, S. Yamamoto, T. Sasagawa, and K. G. Nakamura, Ultrafast phonon dynamics in few-quintuple layer topological insulator Sb_2Te_3, (Ultrafast Phenomena, Okinawa, June 2014).
3. K. Norimatsu, S. Uozumi, K. Igarashi, S. Yamamoto, T. Sasagawa, and K. G. Nakamura, Dynamics of coherent optical phonons in chalcogenide compounds, (CLEO/Europe:2013, Munich Germany, May 2013).
4. K. Norimatsu, J. Hu, A. Goto, K. Igarashi, T. Sasagawa, and K. G. Nakamura, Dynamics of optical phonons in a Bi_2Se_3 crystal studied using femtosecond time-resolved reflection measurement, (Ultrafast Phenomena, Switzerland, July 2012).
5. K. Norimatsu, J. Hu, A. Goto, K. Igarashi, T. Sasagawa, and K. G. Nakamura, Dynamics of coherent optical phonons in a Bi_2Se_3 crystal, (CLEO:2012, San Jose California USA, May 2012).
6. K. Norimatsu, J. Hu, K. Igarashi, T. Sasagawa, and K. G. Nakamura, Observed of coherent optical phonons modes in Bi_2Se_3 using femtosecond time-resolved reflection measurement, (STAC-6, Yokohama, June 2012).
7. K. Norimatsu, J. Hu, A. Goto, K. Igarashi, T. Sasagawa, and K. G. Nakamura, Coherent optical phonon measurements of topological insulator Bi_2Se_3, (STAR symposium, Odawara, May 2012).